AIX-MARSEILLE UNIVERSITE

ECOLE DOCTORALE 353

SCIENCES POUR L'INGENIEUR
MECANIQUE, PHYSIQUE, MICRO ET NANOELECTRONIQUE

Doctoral T H E S I S

to obtain the title of

Doctor of Science

of the Aix-Marseille Université

Speciality: MECHANICS AND PHYSICS OF FLUIDS

Presented by

Muhammad Rizqie ARBIE

Stability of Self-Propelled Body Wake

defended on December 14, 2016

Jury :

Paul BILLANT, LadHyx Palaiseau	Reviewer
Jean-Christophe ROBINET, ENSAM ParisTech	Reviewer
François GALLAIRE, EPFL, Switzerland	Examinator
Sabine ORTIZ, ENSTA ParisTech	Examinator
Uwe EHRENSTEIN, AMU	Co-Advisor
Christophe ELOY, ECM	Advisor

Abstract

The caudal fin of swimming animals can be modelled as a thrust-producing flapping foil. When considered alone, such a foil produces on average a jet wake with a positive net momentum. It has been argued that the instability characteristics of these averaged wakes are linked to the propulsion efficiency of swimming animals. Here, we reconsider this question by taking into account both the thrust and the drag exerted on a self-propelled swimming body. To do so, we study the stability of a family of momentumless wakes, constructed as the Oseen approximation of a force doublet moving at constant velocity. By performing a local stability analysis, we first show that these wakes undergo a transition from absolute to convective instability. Then, using the time-stepper approach by integrating the linearised Navier-Stokes system, we investigate the global stability and reveal the influence of a non-parallel base flow as well as the role of the locally absolutely unstable upstream region in the wake. Finally, to complete the global scenario, we address the nonlinear evolution of the wake disturbance. These results are then discussed in the context of aquatic locomotion. According to the present stability results, the momentumless wake of aquatic animals is generally stable, whereas the corresponding thrust part is unstable. It is therefore essential to consider all forces exerted on a self-propelled animal when discussing its wake stability and its propulsion efficiency.

Résumé

La nageoire caudale des animaux aquatiques peut être modélisée par un foil oscillant qui produit de la poussée. Le sillage moyen d'un tel foil oscillant est un jet de quantité de mouvement nette positive. Il a été proposé que les caractéristiques de stabilité de ces sillages moyens sont liées à l'efficacité de la propulsion des animaux aquatiques. Dans cet étude, nous reprenons cette question en tenant compte à la fois de la poussée et de la traînée exercée sur un corps auto-propulsé lorsqu'il nage. Pour ce faire, nous étudions la stabilité d'une famille de sillages ayant une quantité de mouvement nulle, construit comme l'approximation d'Oseen d'un doublet de force se déplaant à vitesse constante. En effectuant une analyse de stabilité locale, nous montrons d'abord que ces sillages subissent une transition convectif-absolu. Puis, en utilisant une approche "time-stepper" et intégrant le système de Navier-Stokes linéarisé, nous étudions la stabilité globale et mettons en évidence des effets non-parallèles de l'écoulement principal, ainsi que le rle de la région absolument instable dans l'écoulement. Enfin, pour compléter le scénario d'instabilité globale, nous abordons l'évolution non linéaire d'une perturbation injectée dans le sillage. Ces résultats sont ensuite discutés dans le contexte de la nage d'un animal aquatique. Selon les résultats de stabilité, les sillages de quantité de mouvement nulle produit par les animaux aquatiques sont généralement stables, tandis que le sillage qui correspondrait à la pousse seule est instable. Il est donc essentiel de considérer toutes les forces exercées sur un animal auto-propulsé lors de l'examen de la stabilité de son sillage et l'efficacité de sa propulsion.

Acknowledgements

I would like to express my sincere gratitude to my advisors Christophe Eloy and Uwe Ehrenstein for their all time support and guidance. Their patience and deep knowledge helped me through my study and the writing of this thesis. It has always been a great opportunity and honour having both of them as advisors and mentors. I have always been grateful with their encouragements, insightful warm discussions which widened my perspective about the very matter of the research and about research itself.

I am truly grateful being entrusted by Christophe Eloy with this doctoral position (I still remember how happy I was when he offered me to pursue my doctoral study at IRPHE) which I had never imagined when I was still an intern at IRPHE. It was a great experience having him as an advisor since my master's degree internship about architecture of tree (an exciting topic which showed me the importance of free thinking in research) until my doctoral study.

My sincere thanks to Uwe Ehrenstein for his encouragement, warm discussion and talk not only about research but also some other interesting yet important thing (literature, history, language) and some aspects of life which gave much more value to my study.

I would also like to thank the rest of the committee of jury for their insightful comments and questions which expanded my perspective and opened further possibility for improvement and development on my work.

Big thanks also goes to all staff of IRPHE for their help during my stay in France, for making things comfortable and easier (especially for immigration). I thank my fellow doctoral students for the fun chat which helped me enjoy my time (although I'm not good at making conversation, but still, they helped me go through the conversation).

Besides my advisors, I would like to thank Thomas Leweke for his help, warm discussion, and personal teachings that helped me through my early time in France as a master student which was an important step to come to this doctoral study.

Last but not the least, I would like to thank my parents, my brothers and sisters for their continuous support, to my Indonesian friends who also do their study in Marseille, to Adnya, Audy, Halik, and those who I can not mention one by one.

Contents

List of Figures

List of Tables

Chapter 1

Introduction

1.1 Swimming modes of aquatic animals

The large diversity of aquatic animals has given rise to scientific studies concerning swimming mechanisms provided by nature and their applications to man-made vehicles. Numerous studies have been performed on body shapes, body kinematics and its interactions with the surrounding fluid, wake structures, corresponding energy input and output, etc. Review for some of these important aspects are discussed by Lauder (2011).

Hydrodynamics of swimming depend on the size of the swimming organisms. Small organisms deal mostly with viscous effects while big organisms deal mostly with inertial effects. A dimensionless parameter called the Reynolds number may help one to make a quantitative classification for the terms "viscous dominant" and "inertial dominant". This quantity is defined as

$$Re = \frac{U^*\, l^*}{\nu^*} \tag{1.1}$$

where U^*, l^*, and ν^* are the characteristic velocity, the characteristic length, and the kinematic viscosity of the surrounding fluid. In the case of a swimming organism, U^* can be taken as the swimming speed of the corresponding organism while l^* can be taken as the body length. For small Reynolds number, that is $Re \ll 1$, the viscous effect determines the forces involved. On the contrary for large Reynolds number, that is $Re \gg 1$, the inertia dominates. Thus, the swimming mechanisms are also different. Some organisms, however, operates in an intermediate range. Daniel et al. (1992) referred to the range $1 < Re < 10^3$ as the intermediate range in which the hydrodynamics can be influenced by both viscous and inertial effects. Further studies are needed for this regime since there is no clear boundaries between this regime and the other two regimes. Reynolds number regimes from three different sources

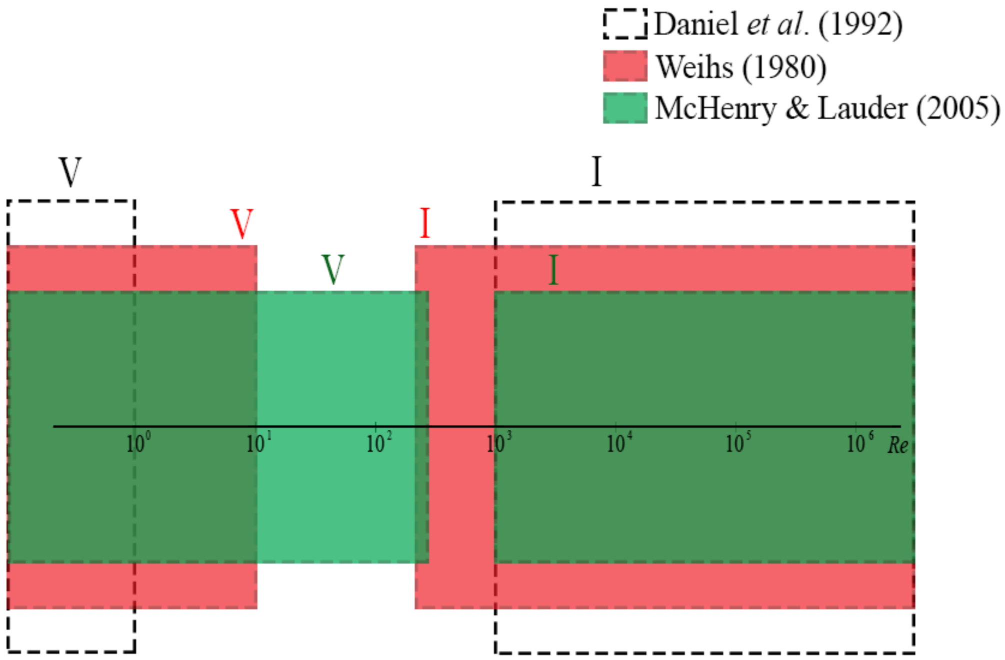

Figure 1.1: Hydrodynamics regime in terms of Reynolds number. V and I stand for "Viscous" and "Inertial" respectively.

are shown in figure 1.1. By examining the changes of inertial drag coefficient and viscous drag coefficient of anchovy following their growth, Weihs (1980) proposed that in larval stage, anchovy swim in viscous regime of $Re < 10$ while in adult stage, they swim in an inertial regime of $Re > 200$. McHenry and Lauder (2005) defined the viscous regime as $Re < 300$ and the inertial regime as $Re > 1000$ by examining "dead" drag of various zebrafish (*Danio Rerio*) ranging from larvae to adult fish.

However, one should note that although this classification is useful in order to obtain a general idea about the regime of a swimming organism, it does not provide a detailed physical descriptions of swimming hydrodynamics since viscous effects still contribute in inertial regime, for example in the boundary layer, which is crucial for drag and wake development.

Besides the flow regime in which aquatic animals operate, it is also important to know how they produce thrust forces, that is the mechanism of active swimming. This is very important since it determines the flow regime, how to approximate forces involved, energetic cost, wake dynamics, etc. In terms of swimming kinematics, aquatic animals employ very diverse modes. Based on the parts of body involved in propulsion, swimming mode have been divided

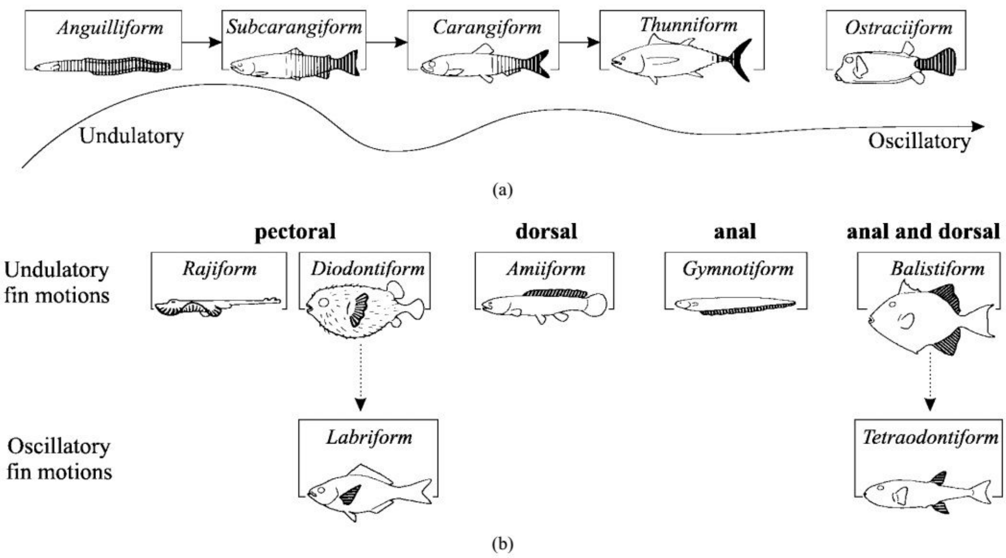

Figure 1.2: Classifications of swimming modes for family of fish taken from Sfakiotakis et al. (1999). (*a*) Body/caudal fin (BCF) class and (*b*) median/paired fin (MPF) class.

into three classes which are "body and/or caudal fin" (BCF) propulsion, "median and/or paired fin" (MPF) propulsion, and jet propulsion (squids, jelly fish). The majority of fish use BCF propulsion (Videler, 1993; Borazjani and Sotiropoulos, 2009; Sfakiotakis et al., 1999). Based on the movement of body parts imposed by the swimmer, one may identify two different swimming styles: undulatory and oscillatory motion. In undulatory motion, a swimming organism bends its body to create backward moving wave along its body to produce propulsion. In oscillatory motion, fish impose a back-and-forth motion of its propellers (can be the caudal or pectoral fins). These classifications are summarised in figure 1.2. One should note that fish, or aquatic animal in general, may employ more than one swimming mode during their lifetime or throughout their daily activities (unsteady swimming, cruising, and manoeuvring). The swimming mode likely determines their body morphology since form and function are probably correlated. Further description on functional morphology for swimming can be found in Webb (1984), Lindsey (1978), and Helfman et al. (2009).

The term anguiliform in figure 1.2 was named after the eel (*anguilla* genus). Eel is a slender fish which creates body waves moving backward with small increase in amplitude to propel forward. This swimming mode is also employed by larvae such as ascidian larvae (McHenry et al., 2003) and microorganisms which operates in the low Reynolds number regime (Azuma, 1992). Ostraciiform, named after the *ostraciidae* family (boxfish), is a mode of swimming in which only the tail is used to produce propulsion. This mode, unlike anguiliform swimming, seems to be useless for swimming in crowded environment (for example in the presence of surrounding corals) but is very useful at maintaining motion against currents. Fish, such as tuna, employ the thunniform mode (named after *thunnus* genera) which is considered as the most efficient locomotion mode that allows tuna to maintain relatively high swimming speed for long periods (Sfakiotakis et al., 1999) which is useful for migration. Amongst these different modes of swimming which involve body bending, anguiliform is supposed to be the least efficient compared to the rest since it has more moving anterior part which also contributes to more drag generation and therefore more waste of energy. One may consider to visit several literatures (Helfman et al. (2009), Vogel (1994), Lindsey 1978) for extended description over these broad range of swimming modes.

1.2 Forces in swimming

1.2.1 Theoretical approaches

Despite the different modes employed by swimming animals, all have something in common: an organism must generate thrust to overcome drag in order to propel through fluid. Here, we summarise the forces involved in swimming and how they are estimated both experimentally and theoretically. In the framework of continuum mechanics, the behaviour of an incompressible Newtonian fluid is described by the Navier-Stokes equations

$$\left(\frac{\partial}{\partial t^*} + \mathbf{u}^* \cdot \nabla^*\right)\mathbf{u}^* = -\frac{\nabla^* p^*}{\rho^*} + \nu^* {\nabla^*}^2 \mathbf{u}^* \ , \tag{1.2}$$

$$\nabla^* \cdot \mathbf{u}^* = 0 \ , \tag{1.3}$$

where $\mathbf{u}^*$ and p^* are respectively the velocity and pressure field of the fluid having density ρ^* and kinematic viscosity ν^*. Boundary and initial conditions are then assigned depending on the problem under consideration. By solving (1.2) and (1.3) to obtain $(\mathbf{u}^*, p^*)$, one can then obtain obtain the force $\mathbf{F}^*$ and torque $\mathbf{L}^*$ acting on a body submerged in the fluid by integrating all forces and torques along the surface of the body as the following

$$\mathbf{F}^*(t^*) = \iint_{S^*} \boldsymbol{\tau}^* \cdot \mathbf{n}^* \, \mathrm{d}S^* \ , \tag{1.4}$$

$$\mathbf{L}^*(t^*) = \iint_{S^*} \mathbf{x}^* \times (\boldsymbol{\tau}^* \cdot \mathbf{n}^*) \, \mathrm{d}S^* \ , \tag{1.5}$$

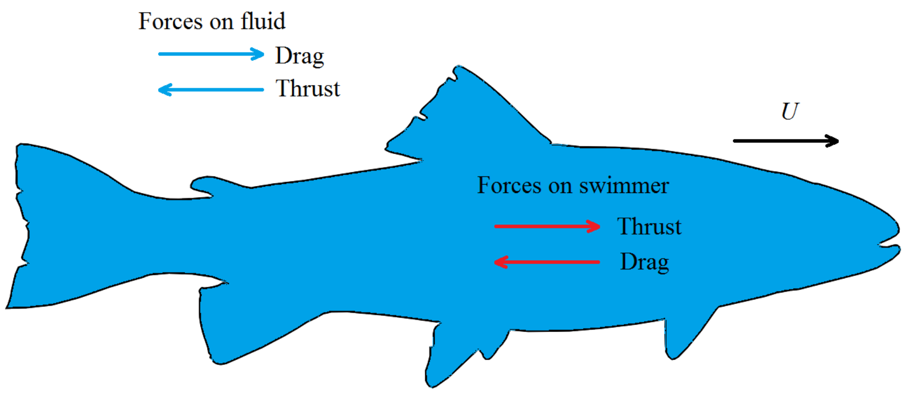

Figure 1.3: Forces interaction between fluid and swimmer.

where $\boldsymbol{\tau}^*$ is the stress tensor given by $\boldsymbol{\tau}^* = -p^*\mathbf{I} + \eta^* \left(\nabla^*\mathbf{u}^* + (\nabla^*\mathbf{u}^*)^\intercal\right)$ with η^* the dynamic viscosity. From (1.4) one can define the terms "form (or pressure) drag" and "skin friction". Form drag is given by the normal components of $\mathbf{F}^*(t^*)$ projected in the direction opposite to swimming motion. Note however that, when the body is moving, form drag and thrust forces cannot be easily separated since they both originate from normal forces. Skin friction, on the other hand, is given by the parallel components of $\mathbf{F}^*(t^*)$, i.e. by integration of the shear stress distribution along the surface of the body.

As mentioned before, an aquatic organism activates various portions of its body when swimming. This activation being itself dependent on the body deformation and motion, there is a strong interaction between the body movement and the surrounding fluid. For instance, in the inertial regime, the body movement will transfer momentum and displace certain amount of mass of the surrounding fluid. Inertia implies opposite reaction from fluid to the body and thus pushes the body into movement. This reaction of the fluid is called thrust. Force interactions between fluid and swimmer is illustrated in figure 1.3.

Mathematical models have been developed to find analytical expressions of the forces produced by body deformations. Lighthill (1960) considered the case of slender fish in the framework of inviscid flow (known as the elongated-body theory) where the flow consists of the steady flow in the vicinity of a stretched straight body and the flow due to the displacement of the body cross-section from its straight position from which mean thrust can be inferred. The variation of the body cross-section is however gradual and smooth giving no possibility for vortex separation but at the end section of the body. As an improvement, Lighthill (1970) took into account large-amplitude deformations of the body (large amplitude elongated-body theory). A more general case was addressed by Wu (1971) where the cross section was taken as a lenticular cross section with pointed edges shedding vorticity along the slender body. Candelier et al. (2011) extended the large amplitude elongated-body theory to arbitrary complex three-dimensional motions.

Since Lighthill's elongated-body theory considers the inertial flow regime where the body parts interact in reactive manner (by Newton's 3rd law of motion) with the surrounding fluid by pushing away a certain mass of fluid, this theory is termed as reactive theory. For animal swimming at low Reynolds number, the viscous effect is however dominant. An early study in the viscous regime was performed by Taylor (1951). By imposing undulatory motion on a sheet, he demonstrated that a propulsive tail animated with a backward propagating bending wave can push a body forward even in the absence of inertial effect. He also extended this concept in the case of two bodies swimming side by side. Various hydrodynamic models for different Reynolds number regime and different modes of swimming are summarised in figure 1.4 taken from Lighthill (1975).

1.2.2 Experimental measurements

Motivated by the ability to determine energetic costs and efficiency of swimming, methods for force measurement have been developed through several studies. Examining steadily swimming fish and assuming that thrust and drag have to balance each other, approximation of swimming efficiency, the Froude efficiency, can be calculated by the ratio of useful power (thrust times velocity) and input power (Lighthill, 1970). It is however difficult to measure either thrust or power output in real fish (Webb, 1971).

On the contrary, the measurement of drag appears to be easier. Earlier methods involve measurements of "dead body" drag, that is assuming that drag of a swimming organism can be approached by drag of a rigid body. Doing so, contributions from body movements are indeed neglected. Usually, freshly killed or anaesthetised fish are used in dead body drag measurements. Dead drag measurements can also be performed by using a technique called the terminal velocity technique, this technique consists of dropping dead fish in a large vertical water container until it reaches terminal velocity, the falling fish is then filmed with a grid on the background so distance in time can be determined (e.g. Richardson, 1936; Blake 1979). Other dead drag measurements consists of placing dead fish in a water tunnel as performed by Brett (1963) or by towing experiments. Towing experiments is reported to give highest drag coefficients (Kent et al. 1961). Although for most cases the results deviates from theoretical models, it provides good estimations for low

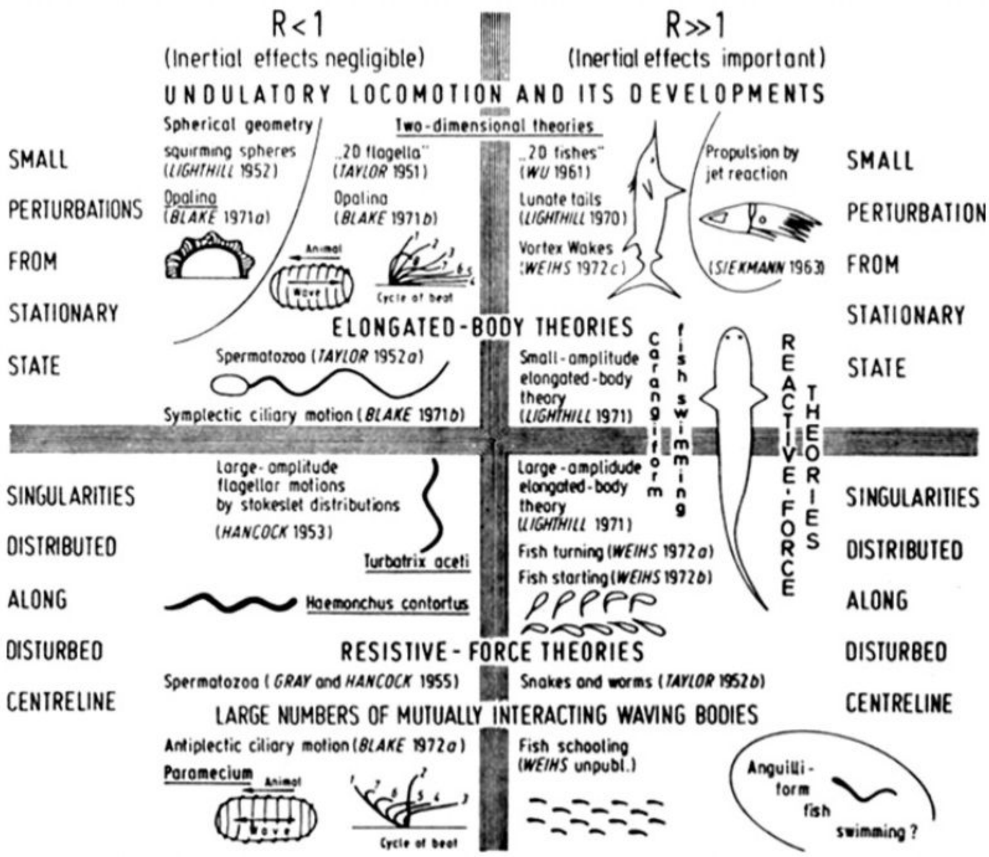

Figure 1.4: Hydrodynamic models with their corresponding swimming modes by Lighthill (1975).

speeds and is consistent with drag estimated during deceleration. Possible errors may arise from neglecting the active parts of fish such as undulating body and flapping fins which can contribute in drag or thrust generation. Webb (1971) investigated drag and thrust of rainbow trout by cleverly placing additional drag loads on the fish in order to obtain frequency and tail beat amplitude variation from which swimming speed and thus drag could be inferred. A different method, which exploits the use of accelerometers planted in the fish body of 1 cm depth, was performed by Dubois and Ogilvy (1978). This allowed them to deduce forces from the body acceleration. They also used pressure transducers attached to the two sides of the caudal fin's upper part which allow them to perform both lateral and forward forces measurement on the tail. The illustration of the experimental setup and the measurement results are given in figure 1.5.

More convincing attempts to estimate forces in swimming have also been done by means of visualisations and analysis of the wake structure behind a swimming organism, since downstream vortex shedding is a result of momentum transfer to the fluid. This can be performed on live fish. A moving part of the swimming organism applies contact forces given by $\int \boldsymbol{\tau}^* \cdot \mathbf{n}^* dS^*$ to its neighbouring fluid element which is equal to $\int (\nabla \cdot \boldsymbol{\tau}^*)\, dV^*$ where $\boldsymbol{\tau}^*$ is the stress tensor, while dS^* and dV^* are the surface area and the volume of the fluid element. Since the rate of change of momentum (of the fluid element) is $\int (\partial/\partial t^* + \mathbf{u}^* \cdot \nabla)\, \mathbf{u}^* \rho^* dV^*$ and considering that the fluid element undergoes body forces of $\int \mathbf{a}^* \rho^* dV^*$ where $\mathbf{a}^*$ corresponds to acceleration due to body force (e.g. gravitational acceleration), then the momentum balance for the fluid element is given by

$$\int \left(\frac{\partial}{\partial t^*} + \mathbf{u}^* \cdot \nabla \right) \mathbf{u}^* \rho^* dV^* = \int \mathbf{a}^* \rho^* dV^* + \int (\nabla \cdot \boldsymbol{\tau}^*)\, dV^* \tag{1.6}$$

which governs the fluid motion because of the momentum transfer. Therefore, the wake structure may give hints on the kinematics of the body that produces the wake. This was demonstrated by Godoy-Diana et al. (2008): they showed that frequency and amplitude of a flapping foil, as parameters of the foil kinematics, may determine the type of wakes generated. Considering different values of frequency and amplitude, they obtained the flapping frequency-amplitude phase diagram, which allows one to identify the transition from the Bénard-von Kármán vortex street to the reversed Bénard-von Kármán vortex street and the transition from drag to thrust generating kinematics.

Some studies used dyes as flow marker to visualise the boundary layer on swimming fish and determine whether there exists boundary layer separation or not in order to have insight into the magnitude of drag which could not

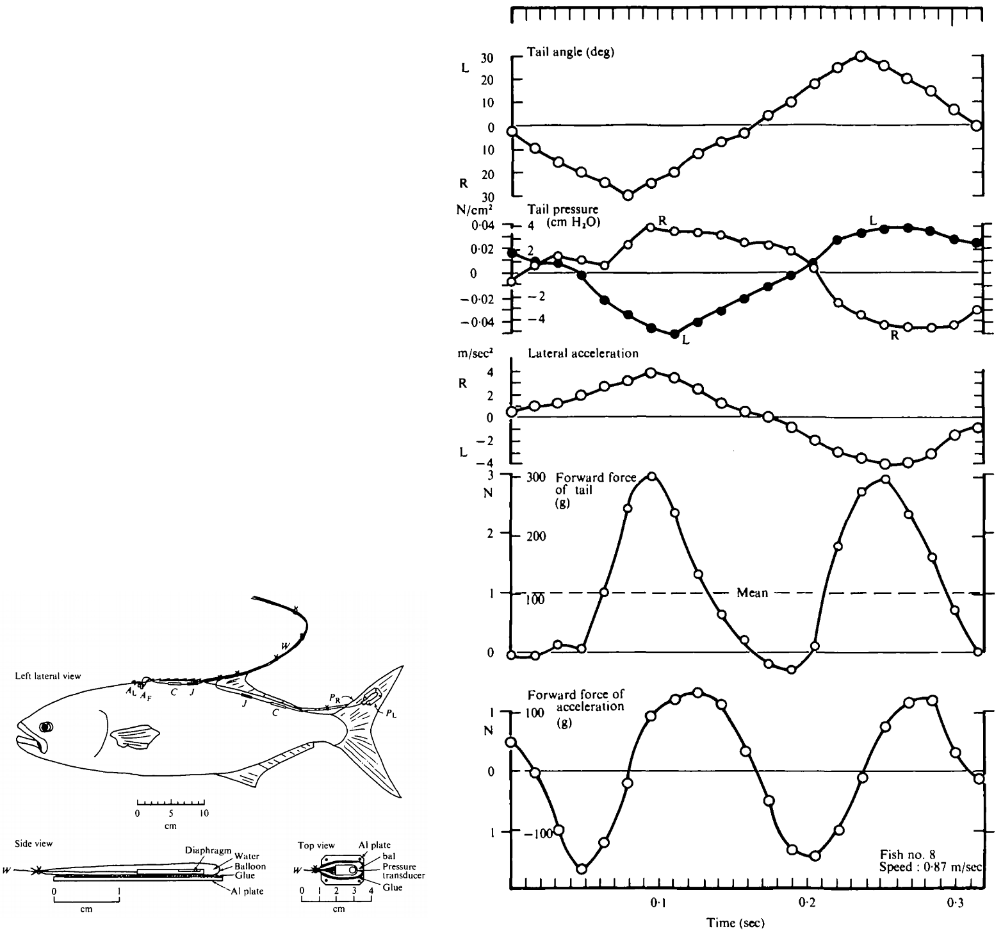

Figure 1.5: Schematic view of the measurement apparatus mounted on a bluefish and the measurements of pressures on the tail, lateral and forward accelerations. Two pressure gauges (for measuring forces) mounted on an Aluminium plate are attached on the right (P_R) and left (P_L) side of the upper caudal fin and are connected to the three wire leads (W) by compensating resistors (C) and epoxy coated juctions in heat shrink tubing (J). Forward (A_F) and lateral (A_L) accelerometers are placed in front of the anterior dorsal fin of the fish. Following the notation used in Dubois and Ogilvy (1978), the forward force of the tail is calculated by $F = (P_R - P_L)\,A\sin\theta$ where A is the area of the tail, $(P_R - P_L)$ is the pressure difference, and θ is the angle between the tail and the flow. This figure is taken from Dubois and Ogilvy (1978).

be measured accurately in some cases by the dead drag approaches. Particle image velocimetry (PIV) have been used to construct wake structures (Müller et al., 1997; Lauder and Drucker, 2002; Fish et al., 2014) as well as the boundary layer around fish body (Anderson et al., 2001). Force in the wake can be calculated from this velocity field by considering three different orientations of the laser sheet to obtain the three velocity components (Drucker and Lauder, 1999). Images from these three different light sheet orientations are not taken simultaneously for several planar sections from the fin base to the fin tip. Taking the images nonsimultaneously is accompanied by an assumption that there is a low variation of fin stroke. Propulsive forces calculated from velocity field produced by the digital PIV are then compared with total body drag and weight obtained empirically. In their study, body drag is measured via towing experiment.

This standard PIV technique has recently been extended to volumetric imaging which is capable of measuring the three dimensional wake structure produced by a swimming fish (for instance in Drucker and Lauder (1999)). However, constructing three dimensional wake structure from sequential two dimensional PIV image still needs improvement. Nauen and Lauder (2002) used a stereoscopic digital PIV instead by using two cameras with different angle of view to produce two simultaneous image recordings with one single laser light sheet. This method allows one to recover the three velocity components. This stereo imaging is used to study wake structure produced by a freely swimming salmoniform fish such as rainbow trout. They reported that the wake produced by the rainbow trout has a strong oscillating jet with large lateral component as the rainbow trout swam in steady motion (shown in figure 1.6).

Flammang et al. (2011) performed also volumetric imaging technique to construct instantaneous three dimensional structures of the wake behind a freely swimming fish. This technique consists of seeding 50 μm plastic tracer particles in the flow to be visualised. 3-components velocimetry is then achieved by tracking particle positions between two laser pulses. This volumetric method is capable of capturing vortical wakes produced by the fins of freely swimming bluegill sunfish eliminating the need to record multiple two dimensional planar fields (Drucker and Lauder, 1999).

The idea of having better techniques, which are capable of constructing instantaneous three dimensional wake structures of freely swimming fish, is often motivated by possible mechanisms for drag reduction. Barrett et al. (1999) performed an experimental measurement of force and power on an fish-like robot having streamlined body design and actively swimming. An illustration of the setup and the drag reduction as a function of swimming kinematics parameters are given in figure 1.7. A backward travelling wave

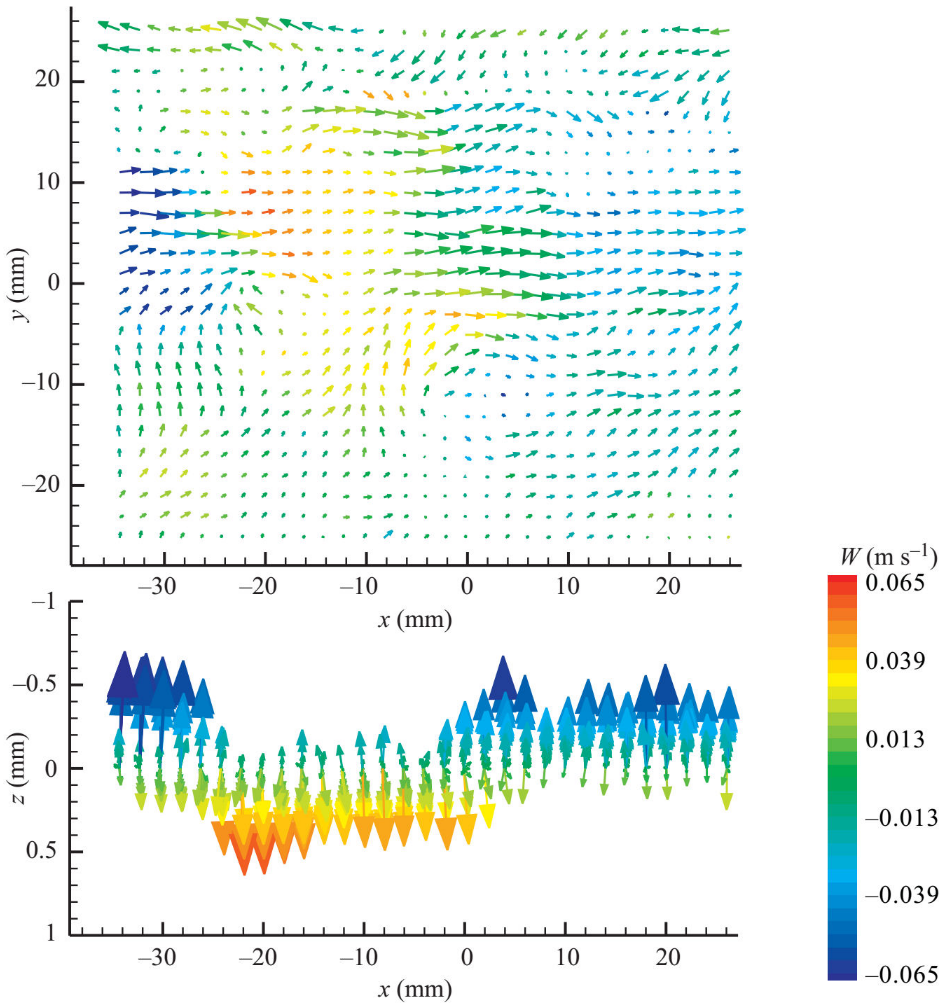

Figure 1.6: Stereo-DPIV measurement of the wake in the immediate downstream of the caudal fin of a rainbow trout (*Oncorhynchus mykiss*) having 16.5 cm bodylength (L^*) swimming at 1.2 L^*/s. The coordinates x, y, and z correspond to the streamwise, vertical, and lateral directions respectively. Here, the lateral component of the wake is 10-60% greater in magnitude with respect to the streamwise velocity component. This figure is taken from Nauen and Lauder (2002).

is imposed on the fish-like body (robotic fish-like mechanism with flexible skin covering the body and equipped with a tail fin) with smoothly varying amplitude from the head to the tail. The structure of the outer part of the fish-like mechanism at rest is an exact replica of bluefin tuna. They showed that the power requirement for propulsion is reduced and is significantly smaller than the power requirement on towed rigid body for a same value of forward velocity. They also showed that phase velocity of the backward travelling wave imposed on the body should necessarily be greater than the forward movement speed suggesting that a controlled lateral movement of body parts during propulsion serves a great deal in reducing drag. Swimming fish is expected to employ drag reduction mechanisms based on the observation of certain behaviour of fish such as long distance migration and the need to reach high speed within short periods (for instance to catch prey) as part of survival needs. Several drag reduction mechanisms have been proposed (see for instance Fish (2006)).

Fish streamlined body design has the advantage of minimizing pressure drag. Drag can also be reduced by minimizing the portion of body involved in thrust generation and thus reducing the amount of lateral movement. Lateral movements reduce the boundary layer thickness resulting in sharper velocity gradients and consequently larger skin friction. This argument is supported by the observation that fastest swimmers use only caudal peduncle and caudal fin to produce propulsion while the rest of the anterior part is held still (Bone and Moore, 2008).

Another proposed mechanism for drag reduction is based on the following idea: drag can be reduced by maintaining laminar flow since drag of laminar boundary layer is smaller than drag of turbulent boundary layer (Barrett et al., 1999). It is suggested that fish, especially in the case of large or fast swimming fish, have a mechanism to control boundary layer over the body, since for large or fast swimming fish, the boundary layer can be highly turbulent. Certain fish such as sharks have dermal denticle parallel to the flow across their skin which can reduce microturbulence and thus preventing laminar-turbulent transition of boundary layer to exist at the anterior part of the body. Barracuda and many other fish control the boundary layer by secretion of mucus containing long chain polymer that can stabilize the turbulent boundary layer and again delay boundary layer separation. It should be noted that boundary layer separation should be avoided in order to prevent pressure drag build up which resist the propulsion greatly.

Other fish, however, are observed to have mechanisms that trigger transition to turbulent boundary layer and maintain it. The advantage of turbulent boundary layer is that it is less sensitive to disturbance and it may delay separation as it is the case for the so-called “drag crisis” of a sphere (Lautrup,

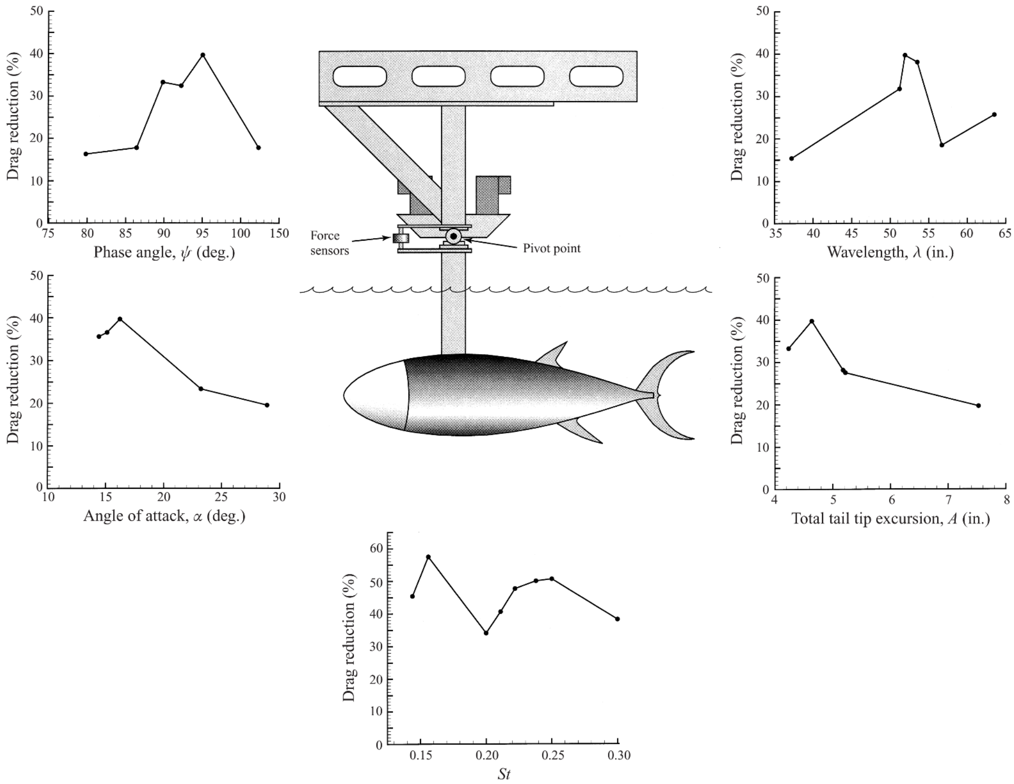

Figure 1.7: Schematic view of the fish-like robot tethered to a carriage along with the results showing drag reduction in self-propulsion as a percentage of rigid-body drag with respect to tail phase angle, tail angle of attack, backbone wavelength, total tail lateral excursion, and Strouhal number. This figure is taken from Barrett et al. (1999).

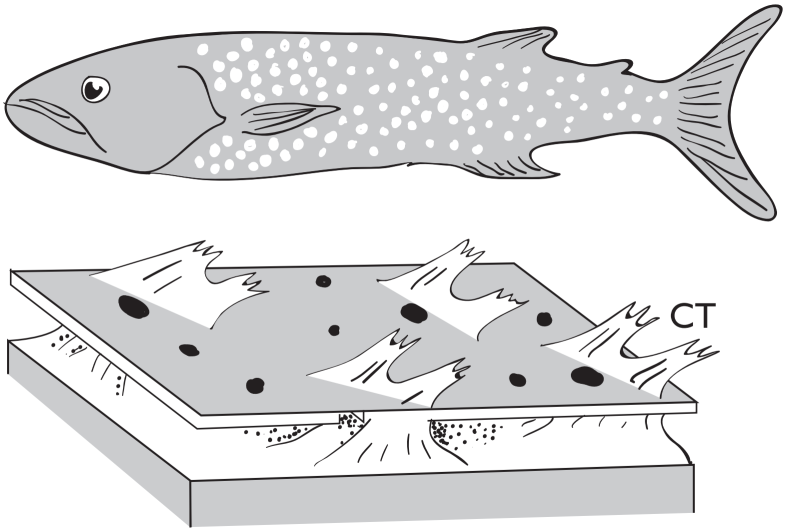

Figure 1.8: Illustration of ctenoid scales (CT) on the surface of fish body which used as vortex generators. They facilitate the transition from laminar to turbulent boundary layer and thus the drag crisis may occur at lower Reynolds number compare to smooth surface. This figure is taken from Bone and Moore (2008).

2011). It may also be more favourable for certain fish to have higher drag caused by turbulent boundary layer rather than having pressure drag by boundary separation. For those fish, boundary layer separation is more likely to happen at higher Reynolds number so they have body parts that may help them induce turbulent boundary layer and maintain it such as the idea of vortex generator in terms of ctenoid scales (Bone and Moore, 2008) as shown in figure 1.8. This conjecture still needs to be proven however. More comprehensive description of these mechanisms and other proposed mechanisms can be found in Bone and Moore (2008) and Bone (1975).

Other proposed mechanisms of drag reduction are related to fish behaviour, for instance schooling. Some fish tend to swim in group of similar body size. Each individual is then likely to take advantage of the energy of the wakes shed by its neighbours in a similar way as "drafting" is used by cyclists (see for instance Morrison (2013)). This behaviour can reduce drag forces. Other behaviour including smaller fish swimming nearby a bigger fish is also suggested as a drag reduction mechanism with the same idea of profiting from hydrodynamic interactions. It has also been proposed that drag is not reduced by fish, but on the contrary enhanced by the swimming motion. This is the Bone-Lighthill hypothesis (Lighthill, 1971).

1.3 Wake behind swimming body

Numerous undulatory swimming animals such as tuna, salmons, and cetaceans produce thrust with their caudal fins, while the anterior part of their body remains almost rigid (Lauder and Tytell, 2005). Motivated by applications to artificial propellers, these caudal fins have inspired studies on thrust generation by oscillating rigid foils (Freymouth, 1988; Koochesfahani, 1989; Schouveiler et al., 2005; Godoy-Diana et al., 2008), and oscillating flexible foils (Moored et al., 2012; Alben et al., 2012; Dewey et al., 2013; Quinn et al., 2014; Paraz et al., 2016).

The study of Koochesfahani (1989) is of interest since it inspired the idea of "wake resonance" (Triantafyllou et al., 1993) discussed below: beat frequency of oscillating foil should be tuned to the frequency of the most unstable mode of the wake instability to maximise efficiency. In this study, the vortical flow patterns produced by a pitching foil have been investigated with flow visualisation by injecting dye in the flow. Both sinusoidal and non-sinusoidal oscillations have been imposed to the foil. Mean velocity profile is constructed with a laser Doppler velocimetry apparatus in order to investigate whether the oscillation of the foil is drag producing or rather thrust producing for different frequencies and amplitudes of oscillation. It was also shown that the wake structure can be significantly altered by the choice of frequency, amplitude, and form of oscillation imposed on the foil. For instance, for a sinusoidal oscillation, a small frequency of oscillation gives a velocity deficit in the mean wake profile, while high frequency of oscillation gives a velocity excess. It could then be concluded that for frequency higher than a certain threshold, the jet with velocity excess is related to thrust-generating foil. It was also shown that for a value of frequency near the threshold, the wake has neither momentum deficit nor excess, that is the velocity profile is nearly uniform and the velocity gradient is nearly zero, which indicates that the wake has no momentum. In this case, the wake structure is neither a Bénard-von Kármán vortex street nor a reversed Bénard-von Kármán one, but is in the form of well-aligned alternating vortices. This is shown in figure 1.9

In these studies of oscillationg rigid foil, the thrust production and the propulsion efficiency are often linked to the characteristics of the wake, with the idea that most of the dynamical information is contained in the fish "footprint" (Müller et al., 1997). Investigation of the wake via visualisation and construction of the velocity field by means of particle image velocimetry on an undulatory swimmer, mullet in their case, allowed the authors to infer quantitative description of vorticity and momentum shed in the wake by the swimmer, which therefore allowed them to estimate the energetic cost.

(a)

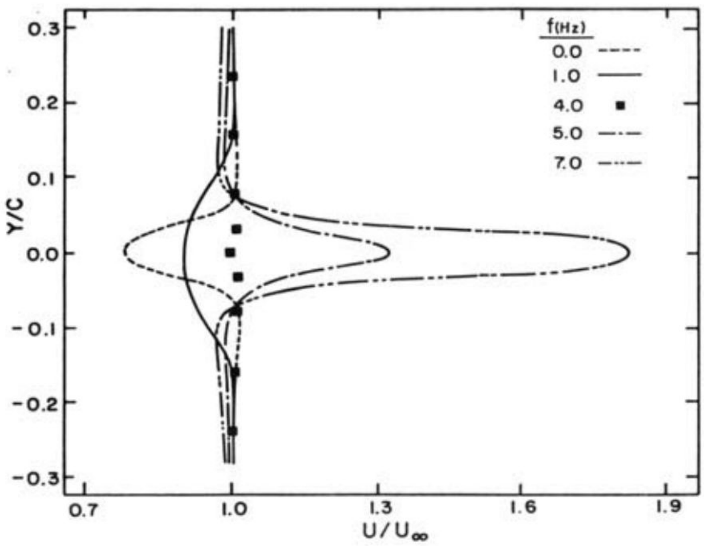

(b)

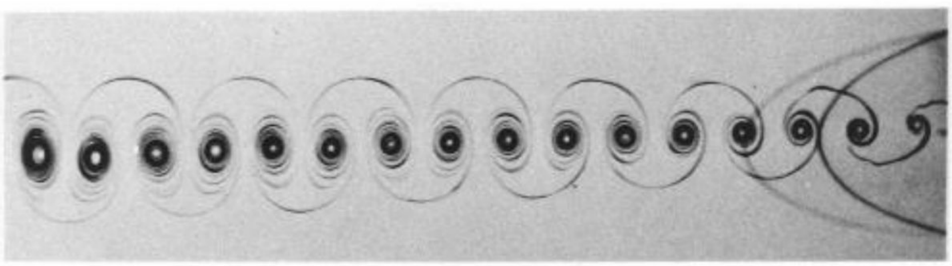

Figure 1.9: (a)Mean velocity profiles in the wake of an oscillating foil with a maximum angel of 2 degree sampled at distance-chord length ratio of $x/L = 1$. (b) Vortex pattern of an airfoil pitching sinusoidally at frequency of 4 Hz and angle of attack of 4 deg, at which the wake has neither a momentum deficit nor excess. Both pictures are taken from Koochesfahani (1989).

This analysis by Müller et al. (1997) on body kinematic and vortical flow pattern indicated an undulatory pumping mechanism during half-cycle of the tail (one stroke) by forming a vortex flow near the inflection point of the undulating body via suction and pressure flows. This vortex is shed when the inflection point reaches the tip of the tail (when the tail reaches its maximum stroke amplitude). As the stroke changes direction, a new opposite vortex build up takes place at the opposite side of the vortex about to be shed. Therefore a vortex ring is formed at each half-stroke.

The question of whether the oscillating frequency of a foil, or in the context of fish swimming the tailbeat frequency, is somehow related to the wake instability frequency has first been addressed by Triantafyllou et al. (1993). In their seminal paper, they considered the stability of the average experimental flow behind a pitching foil as reported by Koochesfahani (1989). A local linear stability analysis is performed by using the average thrust profile as a base profile to show that this profile is convectively unstable. They argued that, since thrust is obtained above a certain frequency threshold with the generation of a wake pattern in the form of a reversed Bénard-von Kármán vortex street, then the frequencies of the most unstable mode in the wake must be related to maximum efficiency of thrust production. The dimensionless parameter related to frequency is the Strouhal number, $St = f^* A^* / U^*$, with f^* the oscillating frequency, U^* the flow velocity, and A^* the width of the wake, taken to be the peak-to-peak amplitude of the foil trailing edge. From linear stability analyses, they found that the jet wake profile is likely to behave as a noise amplifier when excited close to the resonance frequency and the maximum amplification is obtained for $St = 0.25$. This value is compared with various Strouhal number from several fish and cetaceans, from which they conclude that optimal efficiency (and therefore the maximum amplification of perturbation in wake) is obtained when the Strouhal number falls within the range of $0.25 < St < 0.35$ (see also Huerre and Monkewitz (1990)).

Studying experimentally rigid foils activated in pitch and heave, Triantafyllou et al. (1993), and later Schouveiler et al. (2005), also showed that the Froude efficiency (i.e. the ratio between thrust power and input power) reaches a maximum within the same range of Strouhal number. They argued that swimming performance is intimately linked to the characteristics of the wake instability. Similar correlations between the flapping frequency and the frequency associated with the maximum amplification of the jet wake have also been reported in numerical simulations (e.g. Lewin and Haj-Hariri (2003)). It has also been claimed that swimming animals benefit from this efficiency peak by swimming within the same range of Strouhal number: $0.25 < St < 0.35$ (Triantafyllou et al., 1993; Taylor et al., 2003), although this argument is still debated today (Eloy, 2012; van Leeuwen et al., 2015).

More recently this so-called "wake resonance theory" has been reexamined by Moored et al. (2012, 2014), who performed stability analyses on averaged experimental profiles using a locally parallel flow assumption. They concluded that not only one but multiple local maximal efficiencies can be achieved, where each local maximum corresponds to a frequency of a different unstable mode of the average wake profile. They also extended the wake resonance theory to flexible propulsor suggesting that aquatic animal may be able to achieve peak efficiency with the same mechanism, even with flexible appendage. However, despite correlations between these two frequencies, the causal link between the stability properties of the averaged wake profile and the swimming performances has proved difficult to establish so far. In particular, one can argue that the wake instability does not affect the momentum in the wake and therefore will not enhance thrust production.

It should be noted that the wake resonance theory is based on a simplifying assumption: both the stability analysis and the experimental studies on pitching only consider the wake generated by a thrust-producing foil while most fishes or aquatic animals have both thrust generating parts and rigid parts that contribute to drag. Some of them even have thrust and drag intermingled: most body parts produce both thrust and drag simultaneously (for instance in the case of anguiliform swimmers). Therefore wake resonance theory neglects the influence of the rest of the body. Yet, when a self-propelled body swims at constant speed, thrust and drag over the body balance on average, and the wake produced behind such a body has no net momentum.

Considering that the features of wakes behind swimming bodies can be reduced to a combination of spatially localised forces acting on the fluid, a family of momentumless wakes has been proposed by Afanasyev (2004). It is worth mentioning that such consideration may be applicable for the case of small fish and insects or for even more smaller organisms such as microorganisms. In this work, the flow induced by non-translating impulsive localised forces described, for instance, by Cantwell (1986) is generalised to the case of forces translating at constant velocity acting continuously on the fluid. In this consideration, drag and thrust form a force doublet. When a doublet of such translating forces is considered, a family of momentumless wakes parametrised by the intensity of the force doublet, the swimming velocity, and the Reynolds number is obtained (figure 1.10). The objective of the present work is to address the stability of such momentumless wakes. Firstly, we describe the doublet model proposed by Afanasyev (2004) in chapter 2. Secondly, we examine the local stability analysis from which we may obtain the stability diagram on the parameter space of the momentumless

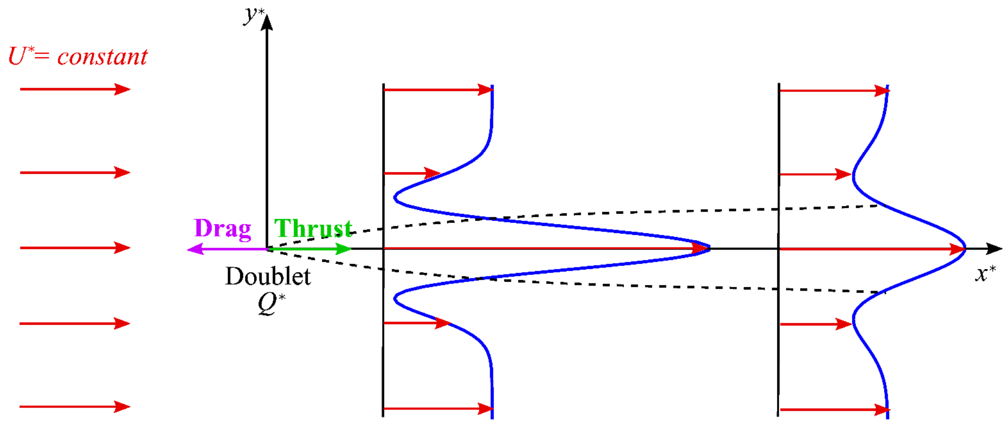

Figure 1.10: Illustration of development of wake produced by a force doublet Q^* acting continuously in time on a uniform flow velocity U^*. The wake width increases further downstream while the amplitude variation decreases showing the effect of viscous diffusion in the flow.

wake in chapter 3. Thirdly, we address its stability globally in both linear and nonlinear case also in chapter 3. Finally in chapter 4, we discuss the relation between the stability results with possible application in swimming of animals in.

Chapter 2

Family of momentumless wakes

Studies concerning wakes produced by self-propelled bodies have been motivated by applications to the design and the detection of man-made vehicle and fish robot. Schooley and Stewart (1963) studied experimentally the turbulent wake produced by a self-propelled body (represented by a tube having permanent-magnet-field motor) in a stratified fluid. More recently, Voropayev et al. (2007) used a radio-controlled submarine model to represent a momentum source moving through stratified fluid in order to study the propagation of momentum disturbance in the presence of buoyancy force. Meunier and Spedding (2006) performed an experimental study on the wake of a bluff body towed in a linearly stratified fluid. In this study, they considered three different wake regimes, which are a wake with strong momentum flux, vanishing momentum flux, and zero momentum flux. When a self-propelled body is moving steadily, that is with a constant velocity, drag exerted on the body and thrust must be in balance resulting in a momentumless wake. Meunier and Spedding (2006) showed that small deviations from momentumless (small momentum wake), can cause the expected behaviour to be qualitatively different from momentumless wake, suggesting that having a momentumless wake is practically rare.

Afanasyev and Korabel (2006) performed an experimental study on a translating force singlet and force doublet in fluid for a moderate Reynolds number. In their study, the forcing is generated electromagnetically. Permanent magnets (one magnet for single force and two magnets for force doublet) are translated near the surface of fluid having two layers of salt water with different concentrations. Electric current is then imposed in the fluid. The interaction between magnetic field produced by each magnet gives a local force as a consequence of Lorentz interaction between moving charged particles and the magnetic field. By this experiment they were able to recover a quantitative similarity between the flow of single force and flow around cylinder. They were also able to recover the reversed Bénard-von Kármán vortex street (typical for a self-propelled object). The case of localised forcing was studied experimentally by Voropayev and Smirnov (2003) in which the localised force was represented by a moving jet. The size of the jet source is of 0.12 cm in diameter which can be considered as point-like momentum source compared to the size of the experimental setup (a long rectangular water tank of $30 \times 40 \times 400$ cm^3). Although, both studies stated the importance of body size in the characteristics of vortex formation behind the body, Voropayev and Smirnov (2003) however concluded that localised momentum source may generate a similar vortex structures (both qualitatively and quantitatively) as a finite body size source in the far field.

2.1 Point-like forcing

An asymptotic model of momentumless wake in the moderately low Reynolds number regime (without turbulence) is given by Afanasyev (2004) based on the formulation of transient flow produced by a moving force doublet. For a single point force, the formulation of the flow as an axisymmetric round jet can be found in Sozou (1979) while a more general family of solutions (for both three dimensional axisymmetric and planar cases) which describes the flow produced by a point source is described in Cantwell (1986). Note that these single force flow formulations are derived by considering the Stokes flow approximation, while boundary layer approximation of such localised forces can be found in Smirnov and Voropayev (2003).

As already mentioned earlier, a self-propelled body moving at constant speed experiences a drag equal and opposite to the thrust produced. Both thrust and drag trigger a momentum transfer between the self-propelled body and the fluid. In the fluid this momentum is evidenced by the emission of vortex dipoles in two dimensions and vortex rings in three dimensions. If one considers a streamwise distance of several body length (in the far field) these two opposite forces can be reduced to a translating force doublet as described by Afanasyev (2004).

In the Stokes approximation, as given by Cantwell (1986) and Afanasyev (2004), the two-dimensional stream function of a single impulsive force located at the origin of the coordinate system (x^*, y^*) (noting dimensional quantities with asterisks) is

$$\psi^*_{I^*}(I^*, x^*, y^*, t^*) = \frac{I^* y^*}{2\pi \left(x^{*2} + y^{*2}\right)} \left(1 - \exp\left(-\xi^2\right)\right), \tag{2.1}$$

with

$$\xi = \sqrt{\frac{x^{*2} + y^{*2}}{4\,\nu^* t^*}}, \tag{2.2}$$

I^* the impulsive force intensity ($[I^*]$=L^{3}T^{-1}) and ν^* the kinematic viscosity. Note that in the above equations x^* is the streamwise coordinate while y^* is the transverse coordinate. The stream function of two opposite forces separated by distance ϵ^* is

$$\psi^*(x^*, y^*, t^*) = \psi^*_{I^*}(x^* + \epsilon^*/2, y^*, t^*) - \psi^*_{I^*}(x^* - \epsilon^*/2, y^*, t^*). \tag{2.3}$$

Performing Taylor's expansion in the limit $\epsilon^* \to 0$ and neglecting second and higher order terms, (2.3) reduces to

$$\begin{aligned} \psi^*_{M^*}(M^*, x^*, y^*, t^*) &= \epsilon^* \frac{\partial \psi^*_{I^*}}{\partial x^*} \\ &= \frac{M^* x^* y^*}{\pi \left(x^{*2} + y^{*2}\right)^2} \left(1 - \left(1 + \xi^2\right) \exp\left(-\xi^2\right)\right), \end{aligned} \tag{2.4}$$

with M^* ($[M^*]$=L^{4}T^{-1}) the doublet intensity

$$M^* = \lim_{\epsilon^* \to 0, I \to \infty} I^* \epsilon^*. \tag{2.5}$$

Since distribution of forces is not important, this limiting procedure is necessary when one takes $\epsilon^* \to 0$ in order to keep the doublet intensity finite.

Let a force, either a single force or a force doublet, moves with a constant speed U^* in the negative x^* direction. By solving the diffusion-advection equation corresponding to the Oseen approximation, one can obtain the stream function of a moving force with intensity J^* ($[J^*]$=L^{3}T^{-2}) for a single force or Q^* ($[Q^*]$=L^{4}T^{-2}) for a force doublet

$$\psi^*_{J^* \text{ or } Q^*}(x^*, y^*, t^*) = \int_0^{t^*} \psi^*_{I^* \text{ or } M^*}(x^* - U^*(t^* - \tau^*), y^*, t^* - \tau^*) d\tau^*. \tag{2.6}$$

In other words, by performing such integration in time, the impulsive force intensities (I^* and M^*) become continuous force intensities (J^* and Q^*), which start to act constantly on the fluid from time 0 to t^*. Taking the derivative of (2.6) with respect to y^*, one obtains the expression for the steady streamwise velocity $u^*(x^*, y^*, t^*)$.

2.2 Profile non-dimensionalisation

The wake behind an object moving in a fluid is a consequence of the boundary layer's development and separation along the surface of the object. At the rear end, the boundary layers of all sides of the body detach and the velocity profile of the wake can partly be viewed as a consequence of this detachment. By viscous diffusion, fluid elements with higher velocity transfer their momentum to slower fluid, which in turn slows down faster fluid elements. This diffusive process results in an increase width of wake and a decrease of velocity deviations as one observes the velocity profile further from the body. By imposing equilibrium of inertial and frictional forces, one obtains that the boundary layer thickness is proportional to the square-root of distance (in the streamwise direction).Therefore, the wake's width should also vary proportional to the square-root of distance from the object. Since in this case, forces distributions is not important, i.e. considering point source forcing, the appropriate choice for characteristic length of the problem is the wake width instead of the usual body length. Therefore, to make the problem dimensionless, we choose the constant swimming speed U^* as the reference velocity, and

$$\delta^* = \sqrt{\frac{\nu^* x^*}{U^*}}, \tag{2.7}$$

as the reference length, which is analogous to a boundary-layer reference length giving $Re = U^*\delta^*/\nu^*$ as the Reynolds number.

Noting dimensionless variables without stars, the relation between dimensional variables and dimensionless variable is given by

$$x^* = \delta^*\, x \qquad y^* = \delta^*\, y \qquad t^* = \frac{\delta^*}{U^*}\, t\,. \tag{2.8}$$

Subtituting (2.8) into relation (2.2) one obtains

$$\xi = \frac{1}{2}\sqrt{Re}\sqrt{\frac{x^2+y^2}{t}}. \tag{2.9}$$

The same procedure can be performed for the streamfunction given by (2.4). Noting that $[\psi^*] = L^2T^{-1}$, one then needs to make ψ^* dimensionless by multiplying it with $\frac{1}{\delta^* U}$ which now gives

$$\psi\,(x,y,t) = \frac{M^* xy}{\pi U^* {\delta^*}^3 \left(x^2+y^2\right)^2}\left(1-\left(1+\xi^2\right)\mathrm{e}^{-\xi^2}\right). \tag{2.10}$$

As stated earlier, to obtain the expression for the streamwise velocity component, one needs to perform the first derivative of ψ with respect to y which will give

$$\frac{\partial\psi}{\partial y} = \frac{M^*}{\pi U^* {\delta^*}^3}\frac{x\mathrm{e}^{-\xi^2}}{\left(x^2+y^2\right)^3}\left(\left(x^2-3y^2\right)\mathrm{e}^{\xi^2} - \left(x^2-3y^2\right)\left(1+\xi^2\right) + 2\xi^4 y^2\right). \tag{2.11}$$

Note that here we have

$$x = \frac{x^*}{\delta^*} = Re = \frac{U^*\delta^*}{\nu^*} = \sqrt{\frac{U^*x^*}{\nu^*}}. \tag{2.12}$$

Now, according to the expression of the streamfunction (2.6), for sufficiently large integration time, one obtains a steady-state solution with dimensionless streamwise velocity profiles for the single force and force doublet given respectively by (in the framework attached to the translating body)

$$u_J(Re, y) = 1 + \frac{J}{2\pi Re}\int_0^\infty \Phi_J[Re - (t-\tau), y, t-\tau]\,\mathrm{d}\tau, \tag{2.13}$$

$$u_Q(Re, y) = 1 + \frac{Q}{\pi Re^2}\int_0^\infty \Phi_Q[Re - (t-\tau), y, t-\tau]\,\mathrm{d}\tau \tag{2.14}$$

with

$$\Phi_J(Re, y, t) = \frac{\mathrm{e}^{-\xi^2}}{(Re^2+y^2)^2}\left((\mathrm{e}^{\xi^2}-1)(Re^2+y^2) + 2y^2(1+\xi^2-\mathrm{e}^{\xi^2})\right), \tag{2.15}$$

$$\begin{aligned}\Phi_Q(Re, y, t) = \frac{Re\ \mathrm{e}^{-\xi^2}}{(Re^2+y^2)^3}((Re^2 - 3y^2)\mathrm{e}^{\xi^2}\\ - (Re^2-3y^2)(1+\xi^2) + 2\xi^4y^2),\end{aligned} \tag{2.16}$$

and

$$\xi = \frac{1}{2}\sqrt{Re}\ \sqrt{\frac{Re^2+y^2}{t}}\ . \tag{2.17}$$

The dimensionless intensities of the single force and doublet are given by

$$J = \frac{J^*}{U^*\nu^*} \quad \text{and} \quad Q = \frac{Q^*}{\nu^{*2}}, \tag{2.18}$$

these two quantities being connected via the doublet size ϵ^* through

$$Q = \frac{\epsilon^* J^*}{\nu^{*2}} = \epsilon\, Re\, J, \tag{2.19}$$

where $\epsilon = \epsilon^*/\delta^*$. The expression (2.14) describes a family of momentumless wakes, parametrised by the dimensionless force doublet intensity Q and the Reynolds number Re (Re can also be viewed as a dimensionless streamwise distance). In the same manner, (2.13) is a family of jet wakes parametrised by the force intensity J and Re. Figure 2.1 shows the streamwise velocity component with respect to the transverse y-coordinate. In Chapter 3, we will study the linear stability of the momentumless wakes with a locally parallel flow assumption. We will also consider a non-parallel case for global

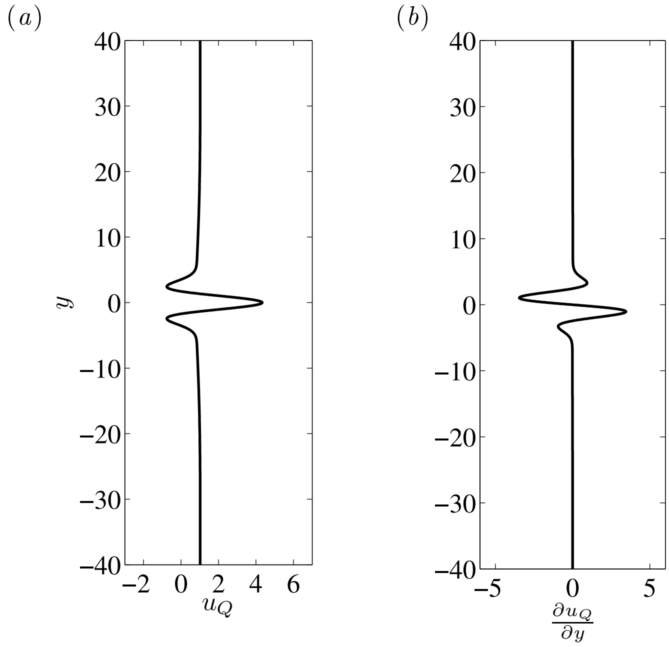

Figure 2.1: An example of a non-dimensionalised streamwise velocity profile behind a force dipole at $Re = 20$ and $Q = 1.9 \times 10^5$.

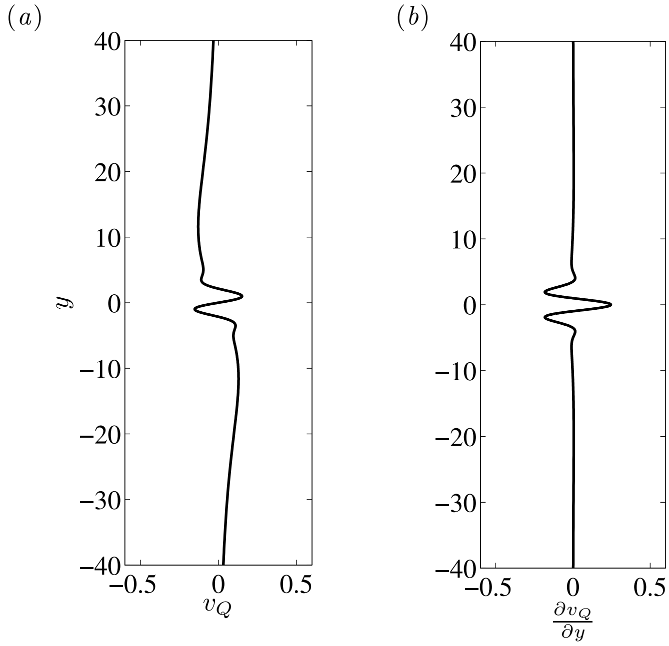

Figure 2.2: An example of a non-dimensionalised lateral velocity profile behind a force dipole at $Re = 20$ and $Q = 1.9 \times 10^5$.

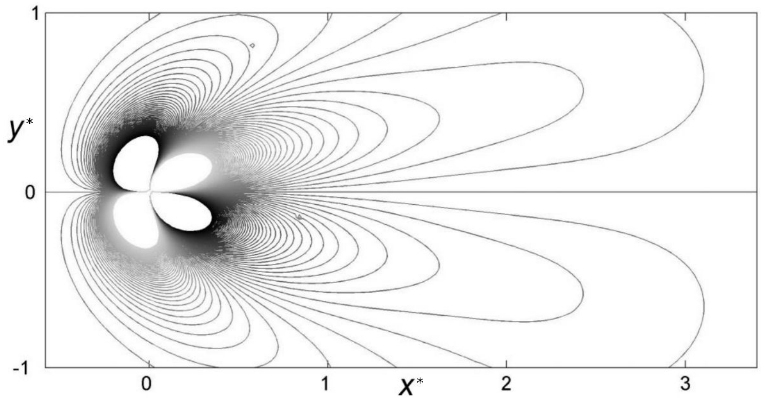

Figure 2.3: Two dimensional vorticity field generated by a force doublet situated at the origin of a Cartesian coordinate showing a quadruple vortex pattern (x^* and y^* are in cm scale). This figure is taken from Afanasyev (2004).

considerations (in both linear and nonlinear cases) in which we also need the lateral velocity component. Performing similar procedures as for the streamwise velocity component, with the only difference is that one needs the first derivative of ψ with respect to x, the lateral velocity is given by

$$v_Q(Re,y) = -\frac{Q}{\pi Re^2}\int_0^\infty \varphi_Q[Re-(t-\tau),y,t-\tau]\,\mathrm{d}\tau, \qquad (2.20)$$

with

$$\begin{aligned}\varphi_Q(Re,y,t) = \frac{y\ \mathrm{e}^{-\xi^2}}{(Re^2+y^2)^3}&(-(3Re^2-y^2)\mathrm{e}^{\xi^2}\\ &+(3Re^2-y^2)(1+\xi^2)+2\xi^4Re^2).\end{aligned} \qquad (2.21)$$

Figure 2.2 shows this lateral velocity component with respect to the transverse y coordinate.

It should be noted that the doublet is a positive force-dipole which induces a flow directed away from the doublet on x-axis, while it attracts flow on both its lateral sides which forms a vortex quadruple around it which is shown in figure 2.3. This can be thought as a typical pusher. Taking the negative sign of doublet gives a negative force-dipole which induces a flow attracted to the doublet on its longitudinal direction while repelling flow on both its lateral side which forms also a vortex quadruple around it but in reversed sense of the first one. This can be thought as typical puller.

Examples of velocity profiles of momentumless wake for different Re values are given in figure 2.4. The wake width appears to be not varying here.

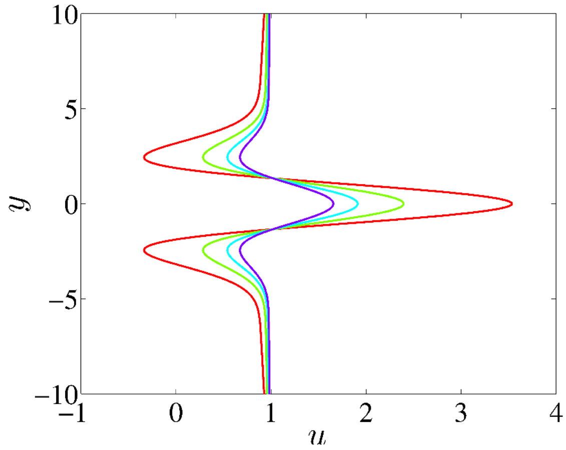

Figure 2.4: Dimensionless wake profiles behind a force doublet at $Q = 1.52 \times 10^5$ for $Re = 20$, red; $Re = 24.5$, green; $Re = 28.3$, light-blue; $Re = 31.6$, purple.

This can be understood since the choice of characteristic length implies that any position along the tranverse y coordinate is always normalised by the corresponding wake width at each streamwise distance. Variation of wake width would be obvious when we consider the non-parallel case where the characteristic length has to be chosen at a fix streamwise distance. One should note also that the multiplication factor Q/Re^2 in equation (2.14) gives different amplitude as we consider different streamwise distances. Equation (2.14) also shows that any two profiles taken at different streamwise distances (or different Re) are not self-similar. This is different from the Blasius boundary layer problem where the base profile is self-similar. Here, the maximum and minimum values are gradually attenuated in a nontrivial way as one considers higher value of Reynolds number, keeping dimensionless doublet intensity constant. This is what one would expect since viscosity results in energy dissipation as the wake travels downstream.

Both the jet and the momentumless wake profiles are parametrised by their impulsive force or doublet strength and Reynolds number. In chapter 3, the stability of both wake profiles will be investigated in this two-dimensional parameter space. We also introduce concepts which will be useful for the stability analysis. For the momentumless wakes, the role of these parameters is investigated not only in the local regime but also in the global regime, in which these parameters are replaced by the inlet parameters that controls the stability of the global structure. The linear stability of the jet-wake profiles (2.13) will be considered in Chapter 5, in connection with results from literature and with the momentumless wake instability results.

2.3 Doublet model and swimming

In this section, we will see how we can interpret the doublet model in the context of swimming animals. In active swimming, an aquatic organism applies thrust to the surrounding fluid to produce propulsion, while being subjected to the fluid drag due to its motion through fluid. The parameter Q in this model can be regarded as a representation of the forcing being applied to the surrounding fluid by the swimmer (see figure 1.3). In this model, the forcing term appears as a multiplication factor as being shown in equation (2.14) and thus it is a major parameter which controls the magnitude of the velocity profile. But how can one determine its value for a particular swimming case?

Consider an aquatic animal of body length L^* swimming with a constant velocity U^* (typically 1 to 10 $L^*\mathrm{s}^{-1}$ for fish) when subjected to skin friction. McHenry et al. (2003) showed that for Reynolds number based on the body length Re_{L^*} at the order of magnitude of 10 or less, drag is primarily generated by skin friction. However, they also showed that the role of form force in generating drag is increasingly important for greater Re_{L^*}. Here we neglect the contribution of the form force. Now, the animal will experience drag proportional to ${U^*}^2$ which allows one to estimate the drag forces (here we neglect the contribution of form drag to the total drag). This skin friction drag per unit length is $F^* \sim \rho^* {U^*}^2 L^* Re_{L^*}^{-1/2}$ which is a boundary-layer scaling (Schlichting and Gersten, 2003) where Re_{L^*} is the Reynolds number based on the body length. Since in constant swimming, drag is balanced by the thrust, the thrust would have the same magnitude in the opposite direction of this drag. Now, the doublet intensity Q^* can be estimated as the multiplication of this drag force per unit density and a length (which is equivalent to relation (2.5), that is $I^*\epsilon^*$), which will give $Q^* \sim U^{*3/2} L^{*3/2} \nu^{*1/2}$.

Therefore, if one has the information of typical swimming parameters, such as the typical swimming speed and body length, or even the total drag (or thrust) estimated from measurements, one can estimate the parameter Q, while the Reynolds number Re (recall that this is the local Reynolds number in the wake) is determined by choosing how far from the forcing one would like to investigate the wake as being shown in figure 2.5 for two cases of 1 cm and 10 cm fish. Figure 2.5 may help one to imagine the order of magnitude of the parameters for other cases.

Before we go any further in addressing the stability of momentumless wakes, other remarks should be made regarding the doublet model. Since

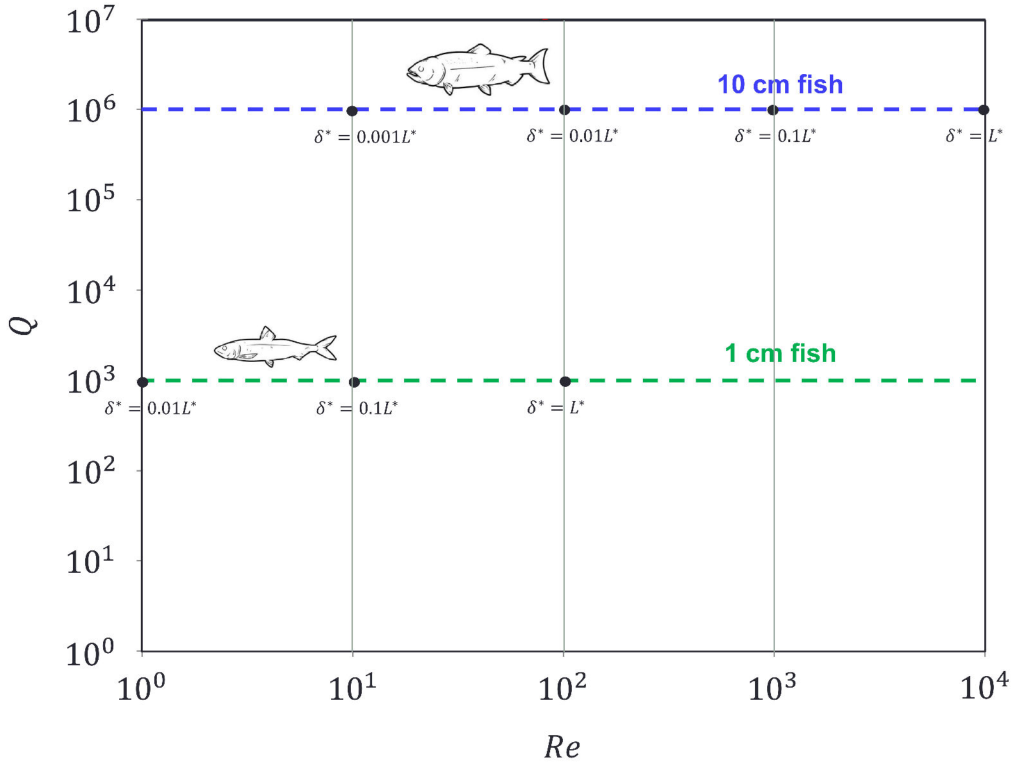

Figure 2.5: Examples of the determined parameters Q and Re for 1 cm and 10 cm fish swimming with $U^* \sim L^* \mathrm{s}^{-1}$.

the doublet is derived by considering the far field, the forcing can be regarded as an artificial source situated at a certain distance in front of the actual body. To imagine this, let us consider the case of an aquatic animal swimming by performing tail beating movement to produce propulsion. In the viscinity of the beating tail of the swimmer, the wake half-width should approximately be the amplitude of the tail beating itself. However, in order to construct a wake profile having half-width equals to the tailbeat amplitude, one may consider a certain distance from the doublet, which may not be likely in the vicinity of the doublet. Nevertheless, not every self-propulsion is produced by tail-beating mechanism. In some other cases, such as in the case of man made object producing propulsion with a turbine, the wake width can be narrower suggesting a smaller distance between the artificial source of forcing and the actual body. It has also been explained earlier that the doublet model is obtained in the Oseen approximation. One may expect that the doublet model is a good approximation for small Reynolds numbers based on the body length. For larger Re_{L^*}, there is no simple wake family corresponding to self-propelled objects. However, one may still use the wake family obtained in the Oseen approximation and fit any wake profile to find the corresponding doublet intensity Q^* and distance from the source.

Some cases relevant to the small Re_{L^*} limit may be worth mentioning: swimming microorganisms (at 100 μm to 1 mm large which gives Re_{L^*} of the order of 1), swimming larvae with undulating tail (where drag and thrust are intermingled since the undulatory motion produce thrust while generating drag at the same time), or fish producing propulsion by using paired fin in which thrust and drag can be produced at small distance in the anterior part of its body.

We will revisit this applicability issue in chapter 4 when we will try to interpret our stability results with regard to for real swimming cases by considering two examples having different Reynolds regime, which are a typical swimming of 10 cm fish and a swimming larva.

Chapter 3

Stability of momentumless wakes

Stability analysis can be regarded in local and global contexts. Since the study covers both local stability analysis and the global dynamics of the momentumless wake, we introduce some basic concepts related to stability analysis of a flow. Particular techniques for handling the full global dynamics are also introduced. Applying non-dimensionalisation to the Navier-Stokes system (1.2) by using a characteristic velocity U^*, a characteristic length l^*, and kinematic viscosity ν^*, one has

$$\begin{aligned} \frac{\partial \tilde{\mathbf{U}}}{\partial t} + (\tilde{\mathbf{U}} \cdot \nabla)\tilde{\mathbf{U}} &= -\nabla \tilde{\mathrm{P}} + \frac{1}{Re}\Delta \tilde{\mathbf{U}} \\ \nabla \cdot \tilde{\mathbf{U}} &= 0 \end{aligned} \tag{3.1}$$

where $\tilde{\mathbf{U}}$ is the velocity field, $\tilde{P}$ is the pressure field, and Re is the Reynolds number. Note that the dimensionless quantities are without the asterisks sign.

To study the linear stability of a particular flow, one can investigate the dynamics of a perturbation around the steady solutions of (3.1) which will be termed as base flow. In this study, we consider two dimensional flow. Suppose that one has a steady solution $U(\mathbf{x})$ and $P(\mathbf{x})$ of the Navier-Stokes equation. The steady solution is not always convenient to find, it is sometimes approximated by finding a mean velocity profile or rather by taking limits of particular Reynolds number regime (based on a certain characteristic length). For instance, in our case, we construct a base flow resulting from the Oseen approximation. Now, by writing the total flow as

$$\begin{aligned} \tilde{\mathbf{U}}(\mathbf{x},t) &= \mathbf{U}(\mathbf{x}) + \mathbf{u}(\mathbf{x},t) \\ \tilde{\mathrm{P}}(\mathbf{x},t) &= \mathrm{P}(\mathbf{x}) + p(\mathbf{x},t) \ , \end{aligned} \tag{3.2}$$

the dynamic around the steady solution is given by the following perturbation equation

$$\frac{\partial u}{\partial t} + (\mathbf{U}\cdot\nabla)\,\mathbf{u} + (\mathbf{u}\cdot\nabla)\,\mathbf{U} + (\mathbf{u}\cdot\nabla)\,\mathbf{u} = -\nabla p + \frac{1}{Re}\Delta\mathbf{u} \qquad \nabla\cdot\mathbf{u} = 0\ . \tag{3.3}$$

In linear stability analysis the perturbation $\mathbf{u}$ and p are considered to be infinitesimal. Thus, the term $(\mathbf{u}\cdot\nabla)\,\mathbf{u}$ disappears resulting in the following linear perturbation equation

$$\frac{\partial u}{\partial t} + (\mathbf{U}\cdot\nabla)\,\mathbf{u} + (\mathbf{u}\cdot\nabla)\,\mathbf{U} = -\nabla p + \frac{1}{Re}\Delta\mathbf{u} \qquad \nabla\cdot\mathbf{u} = 0\ . \tag{3.4}$$

3.1 Local linear stability analysis

Here we make the assumption that the flow is locally parallel. It means that, in the present case, at each streamwise location x^* we consider the base flow as to be locally independent of x^*. The base flow is given by (2.14). Here the lateral velocity component (2.20) is neglected. It should be noted that the flow we consider, which is a momentumless wake produced by a doublet forcing, is in fact non-parallel. Its degree of non-parallelism will however decrease with the distance from the doublet and the locally parallel assumption will be more relevant. The reliability of the local parallel assumption will be visited later as we consider the flow globally.

Now, by taking the local parallel flow assumption, one may write the flow as the following

$$\mathbf{U}(\mathbf{x}) = (U(y), 0)\ . \tag{3.5}$$

We will briefly visit the basic concept of local linear stability analysis. Subtituting the basic flow into the linear perturbation equation (3.4), one obtains the following equations

$$\begin{aligned} \frac{\partial u}{\partial t} + U\frac{\partial u}{\partial x} + v\frac{\partial U}{\partial y} &= -\frac{\partial p}{\partial x} + \frac{1}{Re}\Delta u \\ \frac{\partial v}{\partial t} + U\frac{\partial v}{\partial x} &= -\frac{\partial p}{\partial y} + \frac{1}{Re}\Delta v \\ \frac{\partial u}{\partial x} + \frac{\partial v}{\partial y} &= 0\ . \end{aligned} \tag{3.6}$$

Expressing the infinitesimal perturbation in terms of normal modes, that is

$$\begin{pmatrix} u \\ v \\ p \end{pmatrix} = \begin{pmatrix} \hat{u}(y) \\ \hat{v}(y) \\ \hat{p}(y) \end{pmatrix} e^{\mathrm{i}(\alpha x - \omega t)}, \tag{3.7}$$

with $\omega \in \mathbb{C}$ their frequency and $\alpha \in \mathbb{R}$ their wavenumber in the conventional temporal theory, one obtains the following equations

$$\begin{aligned}\left[-i\omega + i\alpha U - \frac{1}{Re}\left(\frac{\partial^2}{\partial y^2} - \alpha^2\right)\right]\hat{u} &= -i\alpha\hat{p} - \hat{v}\frac{\partial U}{\partial y}\\ \left[-i\omega + i\alpha U - \frac{1}{Re}\left(\frac{\partial^2}{\partial y^2} - \alpha^2\right)\right]\hat{v} &= -\frac{\partial \hat{p}}{\partial y}\\ i(\alpha\hat{u}) + \frac{\partial \hat{v}}{\partial y} &= 0\ .\end{aligned} \tag{3.8}$$

This is equivalent to applying a Fourier transform to the linear perturbation equations. The stability problem in terms of normal modes is to be solved numerically (the discretisation procedure will be described later) with the boundary conditions such that the perturbation vanishes when $|y|$ tends to infinity. This gives rise to the following dispersion relation

$$D(\alpha, \omega(\alpha), Re) = 0 \tag{3.9}$$

as solution of a generalised large matrix eigenvalue problem. Here Reynolds number Re appears as a control parameter. The complex frequency can be written as $\omega = \omega_r + i\omega_i$, the flow being unstable when $\omega_i > 0$.

3.1.1 Absolute versus convective instability

Here we visit the absolute and convective instability nature of a perturbation. The stability problem given by (3.6) can be written formally as

$$\mathcal{L}\left(\frac{\partial}{\partial x}, \frac{\partial}{\partial y}, \frac{\partial}{\partial t}, Re\right)\mathbf{u}(x, y, t) = 0\ . \tag{3.10}$$

In general, the linear perturbation will be a wave packet triggered by an initial condition, for instance a localised impulsive initial perturbation. We refer to the review of Huerre and Rossi (1998) for a more comprehensive description on the fundamental concept of absolute and convective instability. Applying Fourier transform on (3.6) with respect to x together with Laplace transform in time as well, the system given by (3.10) becomes the following non-homogeneous equation

$$\mathcal{L}(\alpha, \omega, y, Re)\hat{\mathbf{u}}(\alpha, \omega, y) = \hat{S}(\alpha, y)\ . \tag{3.11}$$

where $\hat{S}(\alpha, y)$ is the Fourier transform of an initial perturbation $S(x, y)$. One may imagine for instance a localised impulsive perturbation as Dirac type impulse at $t = 0$.

This system may formally be solved by introducing a Green's function and the asymptotic behaviour is determined by the poles $\omega(\alpha)$ of the dispersion relation $D(\alpha, \omega(\alpha), Re) = 0$, in particular those which correspond to the most unstable modes (or the least stable ones) which will give dominant contributions in the inverse Laplace transform. Applying the inverse Fourier transform as well, the dominant perturbation will be in the form of a wave packet given by

$$I \sim \int_{F_\alpha} G(\alpha, \omega(\alpha), y, Re) e^{i(\alpha(x) - \omega(\alpha)t)} \tag{3.12}$$

where F_α is the Fourier integral path ($\alpha \in \mathbb{R}$, $F_\alpha =]-\infty, \infty[$). We emphasize that $\omega(\alpha)$ is such that $D(\alpha, \omega(\alpha), Re) = 0$.

Introducing $x = \mathrm{v}t$, one may write $e^{i(\alpha x - \omega(\alpha)t)} \sim e^{i\rho(\alpha)t}$ where $\rho(\alpha) = \alpha \mathrm{v} - \omega(\alpha)$. Considering the asymptotic behaviour $t \to \infty$, evaluation of the integral (3.12) results in

$$I \sim G(\alpha_0, \omega(\alpha_0), y, Re) e^{i\rho(\alpha_0)t} \tag{3.13}$$

where $\alpha_0 \in \mathbb{C}$ such that

$$\frac{d\rho}{d\alpha}(\alpha_0) = 0 \quad \text{which gives} \quad \mathrm{v} = \frac{d\omega}{d\alpha}(\alpha_0). \tag{3.14}$$

This asymptotic expansion may be derived by the method of stationary phase (see for instance Bender and Orszag (2013)). The time asymptotic behaviour is therefore governed by α_0 and ω_0 where $\omega_0 = \omega(\alpha_0)$ and the amplification rate being $\gamma_{\mathrm{v}} = -\rho_i = -\mathrm{v}\alpha_{0,i} + \omega_i(\alpha_0)$. Absolute instability occurs when $\mathrm{v} = 0$ which corresponds to an unstable direction in the (x, t)-plane. Therefore one looks for α_0 such that

$$\frac{d\omega}{d\alpha}(\alpha_0) = 0. \tag{3.15}$$

The base flow is said to be absolutely unstable if $\omega_{0i} > 0$ and convectively unstable when $\omega_{0i} < 0$.

Let us now summarise the stability properties of a given base profile (in the framework of local stability analysis). Suppose that a system is subjected to a localized impulsive initial perturbation. Considering the time-asymptotic ($t \to \infty$) behaviour of the perturbation, different stability situations along a fixed spatio-temporal ray $\mathrm{v} = x/t$ are given in tabel 3.1. According to table 3.1, a basic flow is said to be absolutely unstable if the impulse disturbance grows in time and spread around a point in a fixed space coordinate where it was initially triggered. It is said to be convectively unstable if the impulse disturbance is convected away by the flow so the flow

Stability of a system	**Condition**
Linearly stable	$\lim_{t\to\infty} \mathbf{u}(\mathbf{x},t) = 0$ along all rays $x/t = \text{const.}$
Linearly unstable	$\lim_{t\to\infty} \mathbf{u}(\mathbf{x},t) = \infty$ along at least one ray $x/t = \text{const.}$
Linearly convectively unstable	$\lim_{t\to\infty} \mathbf{u}(\mathbf{x},t) = 0$ along the ray $x/t = 0$
Linearly absolutely unstable	$\lim_{t\to\infty} \mathbf{u}(\mathbf{x},t) = \infty$ along the ray $x/t = 0$

Table 3.1: Stability conditions of a flow system subjected to an impulsive initial perturbation.

relaxes to its unperturbed state at any fix point in space when $t \to \infty$ but the disturbance grows in time as one observes its evolution in a frame moving, for instance, with a group velocity of the convected disturbance. Graphic representations of these different stability situations is given in figure 3.1.

Here, we briefly illustrate the spatio-temporal stability analysis by considering the celebrated Ginzburg-Landau equation

$$\frac{\partial u}{\partial t} + U\frac{\partial u}{\partial x} = \mu u + \frac{\partial^2 u}{\partial x^2} - |u|^2 u \tag{3.16}$$

Although only one dimensional, this equation serves as a model having ingredients of fluid flow equations with an advection term $U\partial u/\partial x$, a control parameter μ, a diffusion terme $\partial^2 u/\partial x^2$, and a nonlinear term $|u|^2 u$. This equation is often used to model wide variety of physical phenomena such as nonlinear waves, phase transition, etc. The equation (3.16) is linearised around the trivial solution of $u = 0$. Now, consider an initial condition in the form of Dirac delta function

$$u(x, t = 0) = \delta(x). \tag{3.17}$$

The Fourier transform on this function is a constant function of 1. Performing the combined Laplace-Fourier transformation on the linearised equation one arrives at the following expression

$$\hat{u} = \frac{1}{-i\omega + Ui\alpha + \alpha^2 - \mu} \tag{3.18}$$

and the dispersion relation is given by

$$D(\omega, \alpha) = -i\omega + Ui\alpha + \alpha^2 - \mu = 0. \tag{3.19}$$

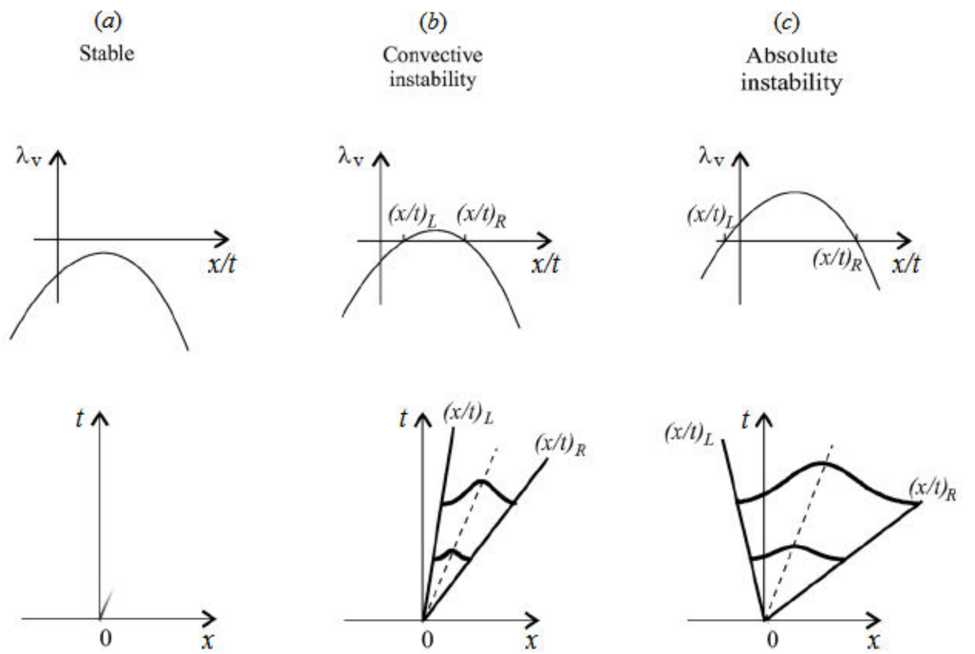

Figure 3.1: Evolution of an impulse disturbance triggered at $t = 0$: (a) Stable, disturbance propagates downstream while being attenuated so the system relaxes to its unperturbed state at any point in space. (b) Convective instability, disturbance propagates downstream so for any fixed point in space, the disturbance decays in time but grows as being observed in a moving coordinate system. (c) Absolute instability, disturbance grows in time while being spread in space.

One can then obtain the expression of ω as a function of α

$$\omega(\alpha) = U\alpha + i\left(\mu - \alpha^2\right). \tag{3.20}$$

The flow is unstable for $\mu > 0$ and $|\alpha| < \sqrt{\mu}$. Looking for α_0 such that $d\omega(\alpha_0)/d\alpha = 0$, one may perform the inverse Laplace and Fourier transform and the following expression is obtained

$$u(x,t) = \frac{1}{2\pi}\int_{-\infty}^{\infty} e^{i\alpha(x-Ut)}e^{(\mu-\alpha^2)t}d\alpha. \tag{3.21}$$

The asymptotic $t \to \infty$ behaviour of this integral is given by

$$\frac{1}{4\sqrt{\pi t}}e^{i\pi/4}e^{i\rho(\alpha_0)t} \tag{3.22}$$

where $\rho(\alpha) = \alpha \mathrm{v} - \omega(\alpha)$, $x = \mathrm{v}t$, and α_0 is the value of α such that

$$\frac{d\rho}{d\alpha}(\alpha_0) = \mathrm{v} - \frac{d\omega}{\alpha}(\alpha_0) = \mathrm{v} - U + 2i\alpha_0 = 0\,. \tag{3.23}$$

Maximum amplification is obtained for $\alpha \in \mathbb{R}$ such that $\frac{d\omega_i}{d\alpha}(\alpha_{max}) = 0$ and by (3.20), we obtain $\alpha_{max} = 0$ and the group velocity is given by $\mathrm{v}_g = U$. More generally

$$\alpha_0 = \frac{i(\mathrm{v} - U)}{2} \tag{3.24}$$

and of course the amplification rate (γ_{v}) is given by

$$-\rho_i(\alpha_0) = \gamma_{\mathrm{v}} = \left(\mu - \frac{(\mathrm{v} - U)^2}{4}\right)\,. \tag{3.25}$$

The nature of absolutely unstable dictates that $\mathrm{v} = 0$ and we obtain that the absolute frequency is given by

$$\omega_0 = i\left(\mu - \frac{U^2}{4}\right). \tag{3.26}$$

Since the amplification rate of the flow is determined by ω_i, then the flow is absolutely unstable if $\mu > U^2/4$ so $\omega_i > 0$ and convectively unstable if $\mu < U^2/4$ so $\omega_i < 0$.

3.1.2 Discretisation of the stability system

Spectral methods are conventionally used for discretisation of flow stability problem. In the class of spectral approximations, functions or solutions of a partial differential equation is approximated by a finite series of orthogonal functions, that is a sum of $N+1$ terms of orthogonal functions $f_k(y)$ as in the following

$$u(y) \approx \sum_{k=1}^{N} a_k f_k(y). \tag{3.27}$$

Some orthogonal functions which can be chosen are the Fourier series, Bessel, Legendre, and Chebyshev. The choice depends on the case being considered. For example, when considering a problem with periodic domain, Fourier series can be a good choice. Here we used the Chebyshev polynomials

When solving a partial differential equation, the solution can be evaluated at specific points in space, that is at the interpolation points which is the Gauss-Lobatto points. For Chebyshev polynomials which is represented as

$$T_k(y) = \cos(k \arccos(y)) \tag{3.28}$$

these points are

$$y_j = \cos\left(\frac{j\pi}{N}\right), \quad j = 0, 1, ..., N. \tag{3.29}$$

This set of points are more concentrated near the boundary of the domain which is $[-1, 1]$, making it suitable for certain case where details near boundaries are important such as boundary layer problems and confined flows. The values of derivatives of the Chebyshev polynomial at this set of points can be obtained easily by means of matrix-vector multiplication, that is by multiplying the vector containing the values of function at the set of points by a derivative matrix $\mathbf{D}$. Fortunately, for the Chebyshev Gauss-Lobatto points, explicit expressions for every component of the derivative matrix do exist. For the first derivative, the components of the derivative matrix is given by

$$\begin{aligned}
D_{j,k} &= \frac{c_j(-1)^{j+k}}{c_k(y_j - y_k)} \quad (j, k = 0, 1, .., N;\ j \neq k) \\
D_{j,j} &= -\frac{y_j}{1 - y_j^2} \qquad\qquad (j \neq 0, N) \\
D_{N,N} &= \frac{2N^2 + 1}{6} \\
D_{0,0} &= -\frac{2N^2 + 1}{6}
\end{aligned} \tag{3.30}$$

where

$$c_j = \begin{cases} 2, & \text{for } j = 0 \text{ or } j = N \\ 1, & j = 1, 2, ..., N-1. \end{cases} \tag{3.31}$$

The derivative for higher order m, can be obtained by taking simply

$$\mathbf{D}^{(m)} = \mathbf{D}^m. \tag{3.32}$$

Particular care needs to be taken when using the Chebyshev collocation method for stiff problem where the solution exhibits large variation in a narrow region. The collocation points should be clustered carefully in the narrow region where the large variation takes place since smoothness and regularity of the solution to be approximated are important aspects in any spectral method. For the Chebyshev collocation method, it is natural that the method can nicely handle stiff problems where the large variation is situated close to $y = \pm 1$. If however the stiff region is situated at the center of the computational domain, one has to use a coordinate transformation to cluster the collocation points in the region of strong variation.

A coordinate transformation in the form $y = f(\eta)$ (where η is the Chebyshev collocation points) has to fulfill some requirements. The first requirement is that the inversion can easily be performed. The choice of $f(\eta)$ should be chosen such that the new coordinates should represent the solution approximation better than the original one. The last requirement is, of course, that the coordinate mapping should cluster the points $y_j = f(\eta_j)$ in the narrow stiff region. Detail description of some typical mappings and the considerations regarding their applicabilities are discussed in a comprehensive manner in Peyret (2002).

In our problem, the domain is within the interval $]-\infty, \infty[$ in the y-direction and significant variation of the velocity profile under consideration is situated around the center line ($y = 0$). Since we want to account both these two constraints in our eigenvalue problem, we use the following mapping Peyret (2002)

$$y = \frac{a\eta}{\sqrt{1 + (a/H)^2 - \eta^2}}, \quad -H \le y \le H, \tag{3.33}$$

with $\eta \in [-1, 1]$ is now the Chebyshev collocation points.

Figure 3.2 illustrates how the distribution of points change for different values of parameter a in (3.33). It can be seen that as we increase the value of a, the points become less clustered around $y = 0$. The value of $a = 1.5$ appears to be appropriate to obtain a distribution of points which concentrate near the center line of the velocity profile (see figure 2.1 for an example of a profile) while conveniently approximating the flow quantities for the rest of the domain. The parameter H has been chosen large enough for the perturbation to vanish at $y = \pm H$. We found that for H larger than 30 the unstable modes could be captured accurately and in order to guarantee the absence of finite height effects we used $H = 100$. In order

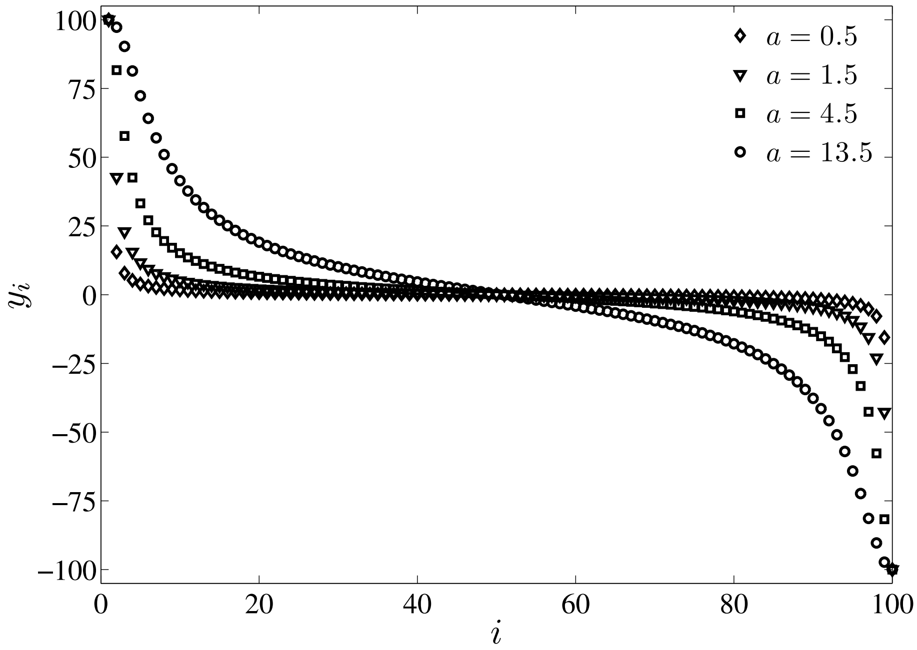

Figure 3.2: Distribution of points after applying the mapping (3.33) for different choice of a.

to guarantee the curve smoothness over the entire domain and to obtain a good convergence, we use 1000 discretisation points. Discretisation of the linearised Navier-Stokes system by using the Chebyshev collocation points in y-direction results in a generalised eigenvalue problem. This generalised eigenvalue problem can be solved by using standard method.

3.2 Local analysis of momentumless wake

In this part, we will use the momentumless wake given by (2.14) as base flow and examine its local stability in its parameter space of Re and Q. Using the numerical procedure described earlier, we first validate the convergence of the computed most unstable mode. The convergence of the computed most unstable mode for varying number of discretisation points is shown in figure 3.3. It can be seen from figure 3.3 that the errors for both the real and the imaginary parts of frequency exponentially decrease as we increase the number of the discretisation points which indicates the spectral accuracy before they reach the limit of round-off error for $N > 500$.

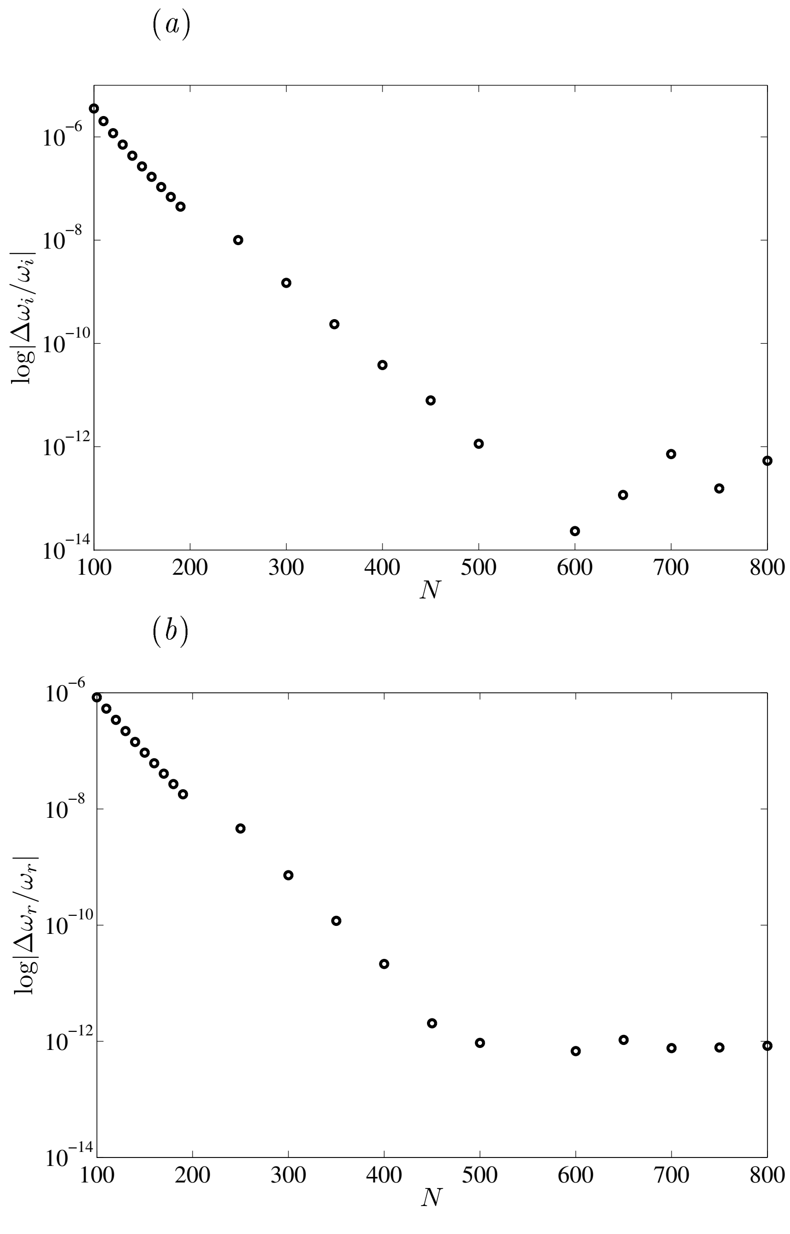

Figure 3.3: The convergence of computed most unstable mode as we increase the number of discretization in transverse y-direction for $Q = 1000$ and $Re = 1$: (a) imaginary part of the frequency and (b) its corresponding real part show convergency.

Starting form temporal stability, that is for $\alpha \in \mathbb{R}$, one may obtain the frequency spectrum related to the most unstable mode as shown in figure 3.4 a for the case of $Q = 10^5$ and $Re = 30$ (the corresponding velocity profile is shown in figure 3.7(c)). In this case the base profile is unstable in the range of $0.1 < \alpha < 1.1$. the most amplified mode is given by $\alpha = 0.663$, $\omega = 0.698 + i0.068$ and its corresponding vorticity perturbation is shown in figure 3.4 (b). Absolute and convective instability can be identified by seeking for what is called the absolute frequency ω_0, which is the solution of the dispersion relation, and such that $d\omega_0(\alpha_0)/d\alpha = 0$ with $\alpha_0 \in \mathbb{C}$. This may be achieved using the so-called cusp map procedure described in Kupfer et al. (1987) where one evaluates the mapping of a varying path in complex α-plane to find a cusp or pinch point in the ω-plane (which fulfils the condition $d\omega_0(\alpha_0)/d\alpha = 0$).

A systematic way to perform the cusp map procedure is as follows: first, we consider the temporal stability by varying α_r for $\alpha_i = 0$, and evaluate $\omega(\alpha)$ values. Then we evaluate another line with $\alpha_i < 0$ and compute again $\omega(\alpha)$. This procedure is repeated by successively decreasing α_i until we find a cusp as shown in figure 3.5. Absolute instability occurs when the imaginary part of the absolute frequency $\omega_{0,i} > 0$, and convective instability occurs when $\omega_{0,i} < 0$. This procedure is demonstrated for the case of $Re = 1$ and $Q = 1000$. Figure 3.5 shows that the corresponding momentumless wake is absolutely unstable since the cusp appears on the upper half of the complex ω-plane, i.e. for $\omega_{0,i} > 0$.

To find the transition between absolute and convective instability, we look for wake parameters Re and Q, such that the cusp appears for real frequency, i.e. $\omega_{0,i} = 0$. An example of transition from convective to absolute instability for low Reynolds number is given by figure 3.6, where the cusp moves from the upper half to the lower half of the complex ω-plane. Therefore, in order to have the stability diagram of the momentumless wake in its parameter space (Re, Q), we located the cusp by varying Re at each value of Q. By tracing the neutral curve and the absolute-convective transition curve together in the (Re, Q)–plane, we obtain the instability map shown in figure 3.7(a). The (Re, Q)–plane is divided into three regions: a stable region, a convectively unstable region, and an absolutely unstable region. As an example, two profiles corresponding respectively to an absolutely unstable and a convectively unstable wake are shown in figure 3.7(c).

For larger Reynolds numbers Re (i.e. $Re \gtrsim 20$), it is found that the transition from absolute to convective instability occurs for $Q = 18.4\ Re^3$, while the neutral curve satisfies $Q = 35.22\ Re^2$. In this framework of the locally parallel flow assumption, we also obtain the dimensionless frequency at the convective–absolute transition, which seems to converge asymptotically

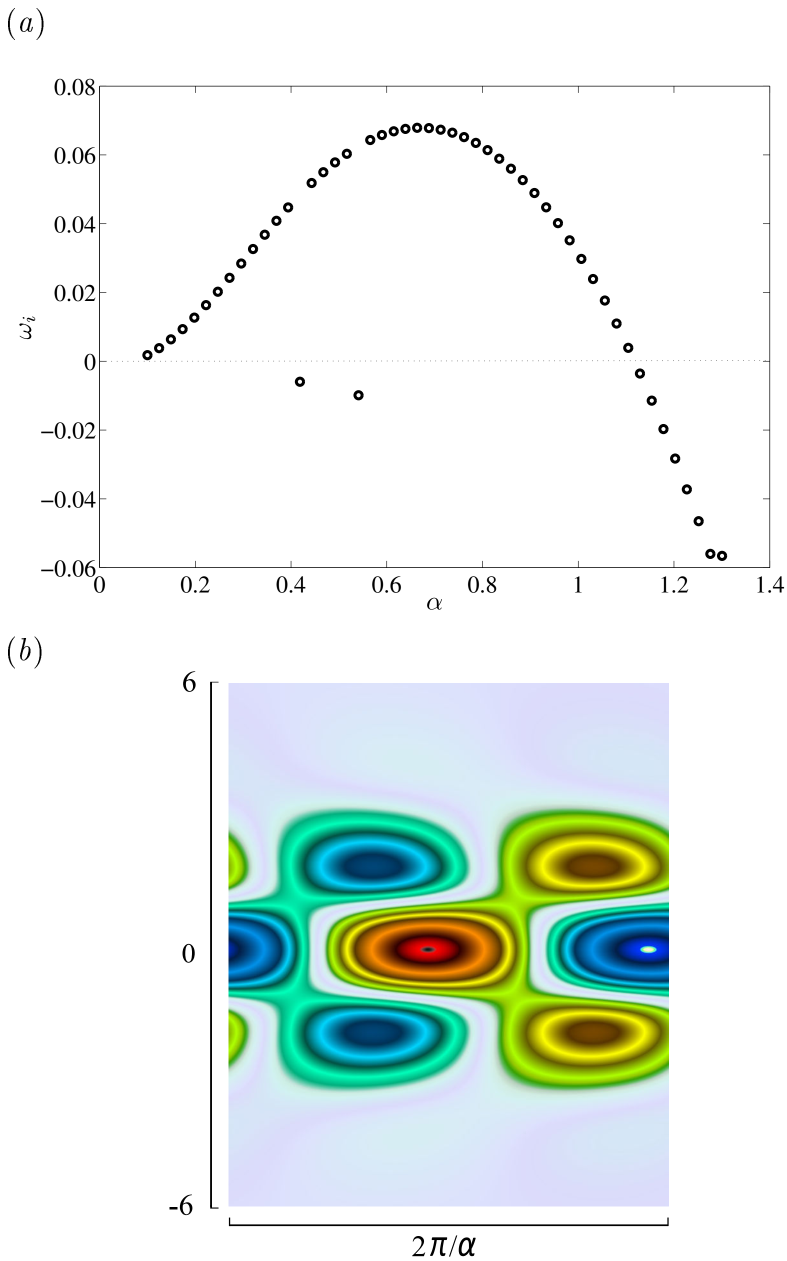

Figure 3.4: Temporal stability for the case of $Q = 10^5$ and $Re = 30$. (a) Amplification rate (ω_i) of the most unstable mode for $\alpha \in \mathbb{R}$. (b) Vorticity perturbation of the most amplified mode over one wavelength with $\alpha = 0.663$.

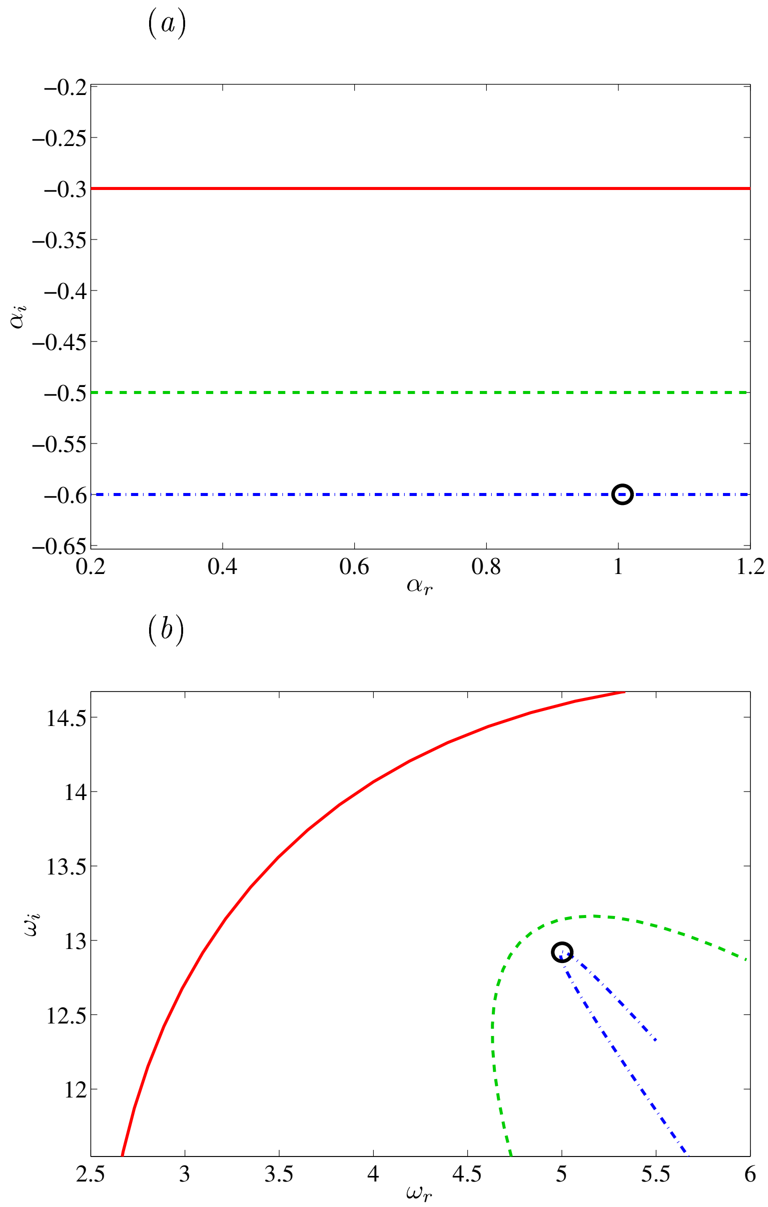

Figure 3.5: Mapping from (a) the α-plane to (b) the ω-plane for a wake profile with Re = 1 and Q = 1000 (each line corresponds to a different value of α_i). This mapping shows a cusp (marked by the circle) on the upper-half of the ω-plane, thus indicating an absolute instability.

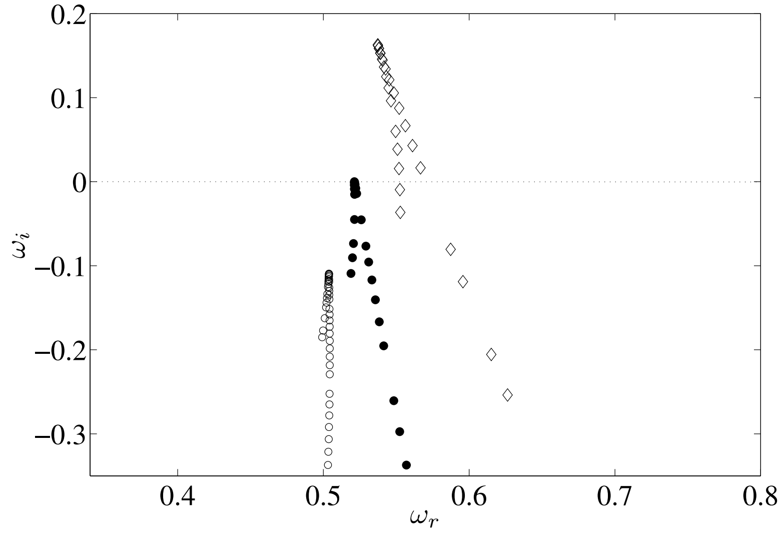

Figure 3.6: Absolute instability to convective instability at $Q = 571.37$ for three different values of Reynolds number: $\Diamond$, Re = 2.3827; $\bullet$, Re = 2.6458; $\circ$, Re = 2.8849.

to 0.93 as both the doublet intensity and the Reynolds number increase as shown in figure 3.7(*b*).

3.3 Global momentumless wake dynamics

Given the non-parallelism of the wakes described by (2.6), a question naturally arises: are the stability predictions based on the locally parallel flow assumption reliable? Is it necessary to have local absolutely unstable region in order to have a global instability (as discussed for instance in Chomaz (2005) for open flows problems)? To address these questions, we perform a global linear stability analysis of the non-parallel base flow. The nonlinear behaviour is also visited to see how an initial perturbation evolves in the full Navier-Stokes system.

3.3.1 Global linear stability

In the previous section, we considered the basic flow as to be locally parallel, even though it depends of course on both the sreamwise and cross-stream

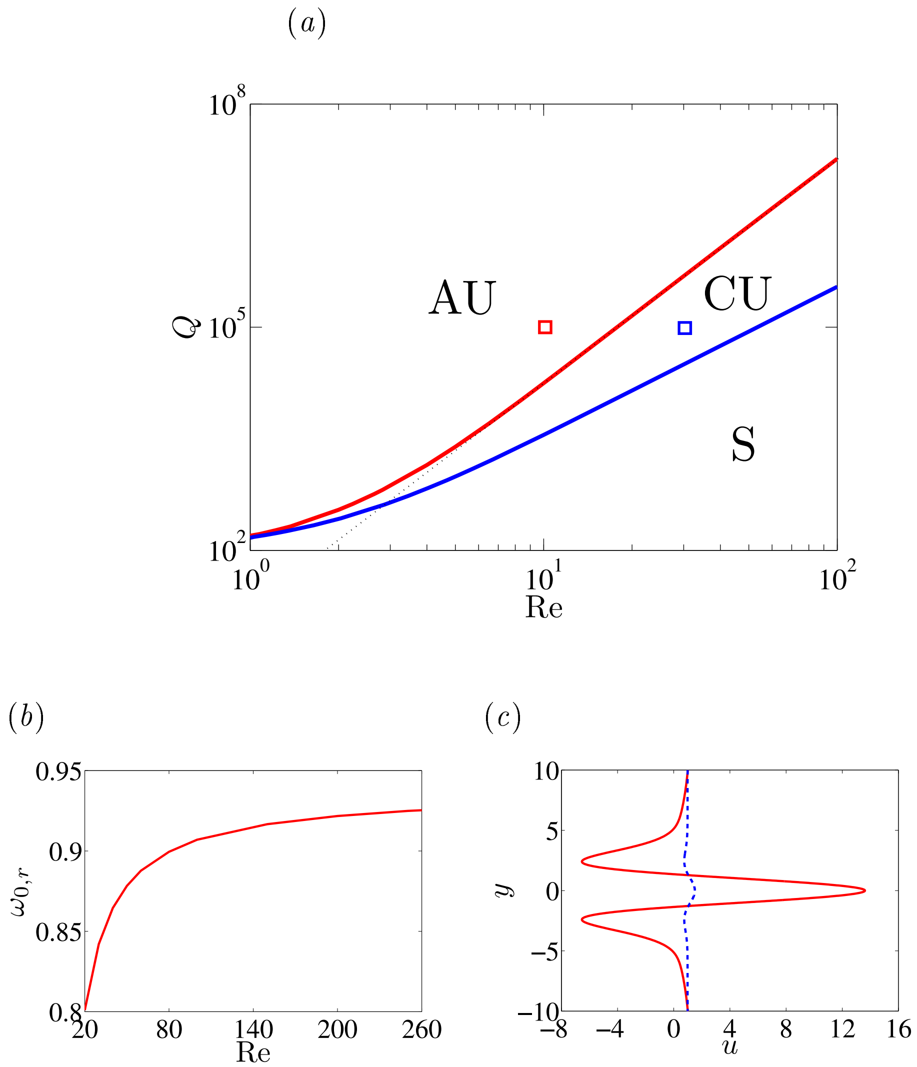

Figure 3.7: (*a*) Instability map in the *Re*–*Q* plane for a momentumless wake. AU, CU and S stand respectively for absolutely unstable, convectively unstable and stable. (*b*) Dimensionless frequency $\omega_{0,r}$ at the convective-absolute transition. (*c*) Absolutely unstable profile for $Q = 10^5$, $Re = 10$ (solid line), and convectively unstable profile for $Q = 10^5$, $Re = 30$ (dashed line). Parameters of the two profiles are marked by coloured rectangles in (*a*).

coordinates. We hence consider now that the base flow is

$$\mathbf{U}(\mathbf{x}) = (U(x,y), V(x,y))\,. \tag{3.34}$$

The linearised Navier-Stokes system given by (3.4) can be written in the following matrix form

$$\mathrm{J}\mathbf{q} = \mathrm{B}\frac{\partial \mathbf{q}}{\partial t} \tag{3.35}$$

where

$$\mathbf{J} = \begin{bmatrix} -(\mathbf{U}\cdot\nabla) - \nabla\mathbf{U} + \frac{\Delta}{Re} & -\nabla \\ \nabla\cdot & 0 \end{bmatrix}, \qquad \mathbf{B} = \begin{bmatrix} \mathbf{I} & 0 \\ 0 & 0 \end{bmatrix} \tag{3.36}$$

where $\mathbf{q} = [u, v, p]^{\intercal}$. The global stability analysis of the flow consists of finding global mode solutions $\hat{\mathbf{q}}(x,y)e^{-i\omega_G t}$. The global stability properties can then be categorised as linearly stable for $\mathrm{Im}(\omega_G) < 0$ and linearly unstable for $\mathrm{Im}(\omega_G) > 0$.

In the case of weakly non-parallel flows, the studies of Chomaz et al. (1991) and Monkewitz et al. (1993) show that the presence of a finite region being locally absolutely unstable is a necessary condition for an unstable global mode to arise through a continuously self-triggering perturbation (in terms of travelling wave in both downstream and upstream direction) and the asymptotic analysis, as demonstrated in local stability analysis, gives a good prediction of the corresponding unstable global mode. Le Dizès et al. (1996) and Hammond and Redekopp (1997) showed that, in the weakly non-parallel setting, the unstable global frequency is given by the local absolute frequency which satisfies $d\omega/dx = 0$, where x being the streamwise coordinate extended in complex plane. It is also shown in Marquillie and Ehrenstein (2003) for a separated boundary layer that the appearance of finite amplitude global mode can be predicted by applying the local absolute instability concept.

3.3.2 Matrix-free method

The attempts to study the stability of a flow, with a strong non-parallelism, has been increasingly progressing by the availability of more powerful computer capacities. On the following, a brief discussion of a matrix-free method is presented which is very useful from practical point of view to study the global instability of a non-parallel flow (see for instance Bagheri et al. (2009)).

The linearised Navier-Stokes system can be recast as

$$\frac{\partial \mathbf{q}}{\partial t} = \mathbf{A}\mathbf{q}. \tag{3.37}$$

The solution at time T for any initial condition $\mathbf{q}_0$ can formally be written as

$$\mathbf{q}(T) = e^{\mathbf{A}T}\mathbf{q}_0. \tag{3.38}$$

In practical fluid flow problems, the explicit exponentiation is of course not tractable computationally. However, the action of the exponential matrix on the vector $\mathbf{q}_0$ can be computed by simply time-marching the discretised linearised Navier-Stokes system from the initial state whatever method of time-integration for the linearised Navier-Stokes system is used.

We are seeking for eigenvalues σ of $\mathbf{A}$, or equivalently eigenvalues $\lambda = e^{\sigma T}$ of $e^{\mathbf{A}T}$. The time-stepping matrix free method consists precisely of computing the significant, with respect to stability, eigenvalue of $e^{\mathbf{A}T}$. One may apply the so-called Rayleigh iteration by computing $\mathbf{q}^{(k+1)} = e^{\mathbf{A}T}\mathbf{q}^{(k)}$ and it is well known that the quotient $q_i^{(k+1)}/q_i^{(k)}$ (with $q_i^{(k)}$ a non-zero component of $\mathbf{q}^{(k)}$) converges towards the maximum (in modulus) eigenvalue λ of $e^{\mathbf{A}T}$, which provides the global leading stability eigenvalue

$$\sigma = (\log\lambda)/T. \tag{3.39}$$

For real operators, the standard Rayleigh iteration converges under the assumption that there is one leading eigenvalue which is hence necessarily real. However, in fluid flow stability problems, complex leading eigenvalue are expected and the Rayleigh iteration procedure has to be adapted.

Suppose that λ_1 and λ_2 are eigenvalues that form a complex conjugate pair ($\lambda_2 = \bar{\lambda}_1$). To obtain both the instability amplification rate and the frequency, a variant of the simple Rayleigh iteration has been considered, by computing the coefficients $\gamma_{0,k}$ and $\gamma_{1,k}$ for every three steps in the procedure such that

$$\frac{1}{||\mathbf{q}^{(k)}||}\left(\gamma_{0,k}q_j^{(k)} + \gamma_{1,k}q_j^{(k+1)} + q_j^{(k+2)}\right) = 0 \tag{3.40}$$

(by selecting two components $q_j, j = j_1, j_2$ of the vector fields to compute $\gamma_{0,k}, \gamma_{1,k}$). Convergence implies that $\gamma_{0,k} \to \gamma_0$, $\gamma_{1,k} \to \gamma_1$. The complex conjugate pair of λ can then be obtained by solving

$$\gamma_0 + \gamma_1\lambda + \lambda^2 = 0 \tag{3.41}$$

while the leading stability eigenvalue $\sigma = \sigma_r \pm i\sigma_i$ is calculated by using the relation (3.39). The choice of T is important in this matter since it is related to the oscillation of the perturbation and so the characteristic of the flow structure. The Nyquist criterion can give the maximum time interval between two successive sampling, i.e. there should be at least two sampling points in one period must be captured by the time interval (Bagheri et al., 2009). We will show in section 3.34 how this procedure is applied on the momentumless wake profiles considered in our stability problem and how this procedure converge.

3.3.3 Numerical method

By the time-stepper procedure, recall that the exponential matrix can be approximated by simply time-marching the discretised linearised Navier-Stokes system from an initial state. Here, we briefly introduce the numerical method used to solve the full Navier-Stokes system. It is documented in Marquillie and Ehrenstein (2002) for the study of a two-dimensional boundary layer flow over a bump. This code was adapted to our open flow case to study the global stability and the nonlinear behaviour of the momentumless wake. The streamwise direction is discretised by high order finite difference schemes (the details are given in the Appendix B), while the transverse direction is discretised by the Chebyshev collocation method. The Chebyshev collocation approach has already been described previously. The open domain of $]-\infty,\infty[$ in y coordinate is mapped onto a finite domain of $[-1,1]$ by using the same transformation given by (3.33).

A semi-implicit second-order backward Euler method is used to integrate the Navier-Stokes system in time. The Laplacian term is taken implicitly, whereas the nonlinear and convective terms are evaluated explicitly using a second-order Adams-Bashforth scheme. The discretised formulation of the linearised Navier-Stokes system is then

$$(\Delta - 3\tau)\mathbf{u}^{(n+1)} = Re\ \nabla p^{(n+1)} + \mathbf{f}^{(n,n-1)} \tag{3.42}$$

$$\nabla \cdot \mathbf{u}^{(n+1)} = 0 \tag{3.43}$$

where $\mathbf{f}^{(n,n-1)}$ is given by

$$\mathbf{f}^{(n,n-1)} = -4\tau\mathbf{u}^{(n)} + \tau\mathbf{u}^{(n-1)} + Re\left[(\mathbf{U}\cdot\nabla)\,\mathbf{u} + (\mathbf{u}\cdot\nabla)\,\mathbf{U}\right]^{(n,n-1)}. \tag{3.44}$$

In the above equations $\tau = Re/(2\Delta t)$ while the superscript $(n, n-1)$ denotes the explicit Adams-Bashforth time differencing where $[\cdot]^{(n,n-1)} = 2[\cdot]^{(n)} - [\cdot]^{(n-1)}$. At both inlet and outlet, the following advective boundary condition is used

$$\frac{\partial \mathbf{u}}{\partial t} + U_{ad}\frac{\partial \mathbf{u}}{\partial X} = 0 \tag{3.45}$$

in order to allow the perturbation to escape the computational domain with U_{ad} being a conveniently chosen convective velocity. A zero Dirichlet boundary conditions are imposed at infinity in Y-coordinate. This is to be solved using the projection method in order to recover divergence-free velocity field which is recalled in the Appendix B.

3.3.4 Global linear stability results

For some inlet position x_0^*, we define Re_0 as the Reynolds number formed with the reference length $\delta_0^* = \sqrt{\nu^* x_0^*/U^*}$ at inflow. We define X as the dimensionless (using δ_0^*) distance from inflow and the corresponding local Reynolds number may be written as

$$Re = Re_0\sqrt{1 + \frac{X}{Re_0}}. \tag{3.46}$$

The non-parallel evolution of the base flow may be taken into account by simply using (3.46) in the base-flow (2.14) formula. The transverse coordinate Y made dimensionless with δ_0^* is then

$$Y = y\sqrt{1 + \frac{X}{Re_0}}. \tag{3.47}$$

The domain we consider is shown by a straight dashed line in figure 3.8(a) where I, II, III (corresponding to $Re_0 = 20, 21.83, 22.4$ respectively) are the 3 different upstream inflow boundaries which have been used to solve the linearised Navier-Stokes system, for the force doublet intensity $Q_0 = 1.9 \times 10^5$. The inflow position I has been chosen to be inside the absolutely unstable parameter region, whereas III is inside the convectively unstable domain, II being approximately on the absolute-convective transition boundary. In all the computations performed the outflow boundary corresponds to the point IV on the dashed line. The streamwise velocity profiles at the positions I, III and IV are shown in figure 3.8(b) while the streamwise velocity variation along the centerline is shown in figure 3.9 which illustrates the important non-parallelism. The non-parallelism is naturally stronger for small X and diminishes further downstream. Also, the profiles exhibit strong variations in Y as in the local stability which makes it necessary to use a high discretisation when aiming at solving the linearised Navier-Stokes system (3.4). In order to obtain a fully resolved flow field, the transverse Y-direction is discretised with 600 points in the range $-40 \le Y \le 40$, which extends sufficiently far from the region with significant variations of the base flow profiles (cf. figure 3.8(b)). Note that in the direct numerical simulation the coordinate system is now normalised by δ_0^*. The streamwise direction is therefore discretised using $\Delta X = \Delta x/\delta_0^* = 0.02$. Since we used 2400 discretisation points in the streamwise direction for the largest domain from I to IV, the distance from I to IV in the direct numerical simulation coordinate system is $X = 48$.

The initial (divergence free) flow field $\mathbf{q}^{(0)}$ considered is a Gaussian func-

(a)

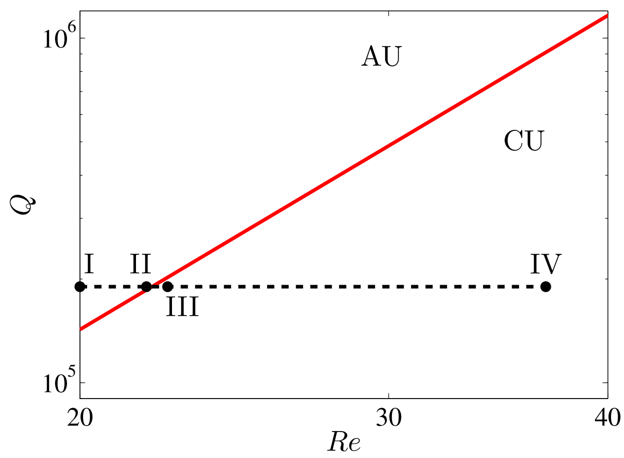

(b)

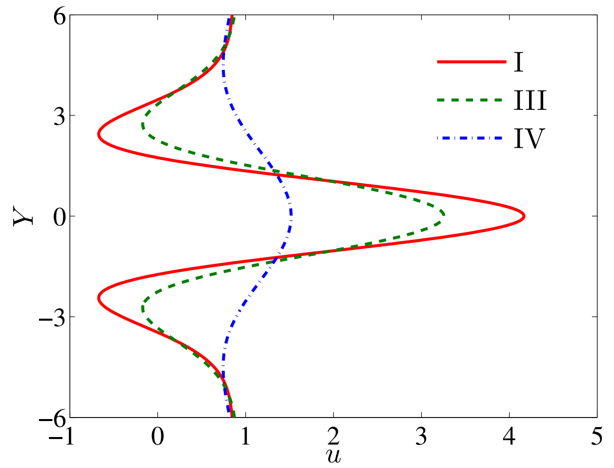

Figure 3.8: (a) Set of non-parallel profiles at $Q_0 = 1.9\times10^5$ on the Q-Re-plane that ilustrates our system. I is the inlet at $Re_0 = 20$ while IV is the outlet at $Re = 36.87$. (b) Streamwise variation of the base flow used in the direct numerical simulation at 3 different locations marked on (a).

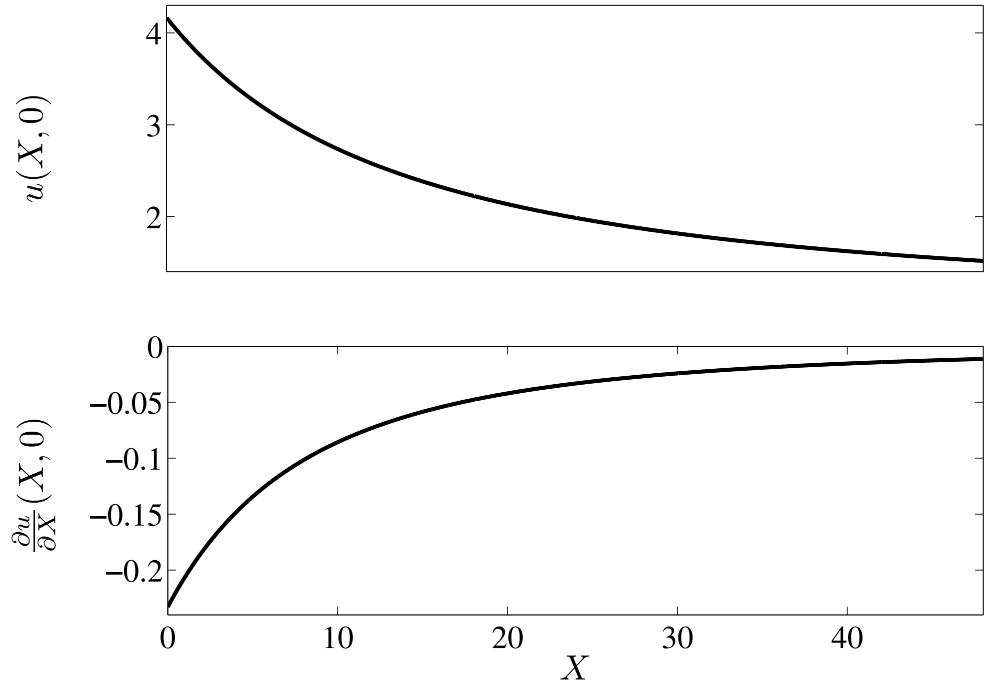

Figure 3.9: Variation of the streamwise velocity component and its first derivative with respect to X along the centerline of the domain.

tion

$$\begin{pmatrix} u \\ v \end{pmatrix} = A \begin{pmatrix} -(Y - Y_0) \\ (X - X_0)\sigma_Y^2/\sigma_X^2 \end{pmatrix} \exp\left(- \frac{(X - X_0)^2}{2\sigma_X^2} - \frac{(Y - Y_0)^2}{2\sigma_Y^2} \right), \tag{3.48}$$

centred at $Y_0 = 0$ and located relatively close to the inlet (with $X_0 = 8$ for the inlet at I). Note that since the initial condition is a Gaussian like perturbation, the two parameters σ_X and σ_Y controls the variance of the perturbation in streamwise X- and cross-stream Y-direction. Since strong flow is expected to be in the streamwise direction, σ_X should be chosen as small as possible in order to excite wider range of spatial modes. Here, we choose $\sigma_X = 0.5$ and $\sigma_Y = 1$. At outlet, the advective boundary condition given by (B.6) has been considered. The value of $U_{ad} = 0.12$ proved to be appropriate to let the pertubation leave the domain without reflection. Also, the computed frequency of oscillation of the global structure appeared to be fairly insensitive to the exact choice of U_{ad} (the values 0.12 or 0.06 for U_{ad} giving the same global eigenvalue results). A zero Dirichlet boundary

Inlet	σ_r	σ_i
I	0.027	0.63
II	3.82×10^{-3}	0.51
III	-3.57×10^{-3}	0.52

Table 3.2: Global linear eigenvalue $\sigma = \sigma_r \pm \sigma_i$ for 3 different inlets : inlet I ($Re_0 = 20$), inlet II ($Re_0 = 21.83$), and inlet III ($Re_0 = 22.44$).

condition proved to be appropriate for the inlet positions II and III since the corresponding velocity profile is at the margin of local absolute instability for position II and locally convectively unstable for position III indicating that no upstream propagations of perturbation were encountered.

For the inlet I, inside the absolutely unstable region, upstream propagating perturbations are expected and indeed the use of a Dirichlet condition led to spurious reflections at inflow and ultimately divergence was encountered. An advective boundary condition (4.6) has therefore also been applied at inflow in this case, with a negative advective velocity. Given the weak absolute instability, a small (in absolute value) advective velocity proved to be suitable and $U_{ad} = -10^{-3}$ has been chosen as about the smallest value such that no perturbation wave reflections were encountered at inflow. The time interval T for the successive flow snapshots has to be appropriately chosen such that it satisfies the Nyquist criterion Bagheri et al. (2009), i.e. there should be at least two sampling points in one period of oscillation. The value $T = 1.1$ has been considered, which is small enough given that the period at the absolute-convective transition is roughly 7.7.

Considering the inflow at I, The modified Rayleigh iteration is shown to converge towards an eigenvalue pair after 300 iterations as shown in figure 3.10. The value of σ_r is positive and a globally unstable mode is hence found. The real part of the eigenfunction's streamwise and cross-stream velocity component in the (X, Y)–plane is shown in figure 3.11. It is obtained that the corresponding frequency of oscillation, given by $\sigma_i = 0.63$, is different from the frequency at the absolute–convective transition calculated by considering the local stability analysis of the previous section. The absolute frequency of the local profile of approximately position II (the transition point from convective to absolute instability) is found to be $\sigma_i \approx 0.8$ which would be the expected instability frequency of the global mode if the basic flow were only weakly non-parallel (Chomaz, 2005). This discrepancy illustrates the influence of the base flow's non-parallelism in the present problem. Interestingly, for the inlet II very close to the location of the local absolute–

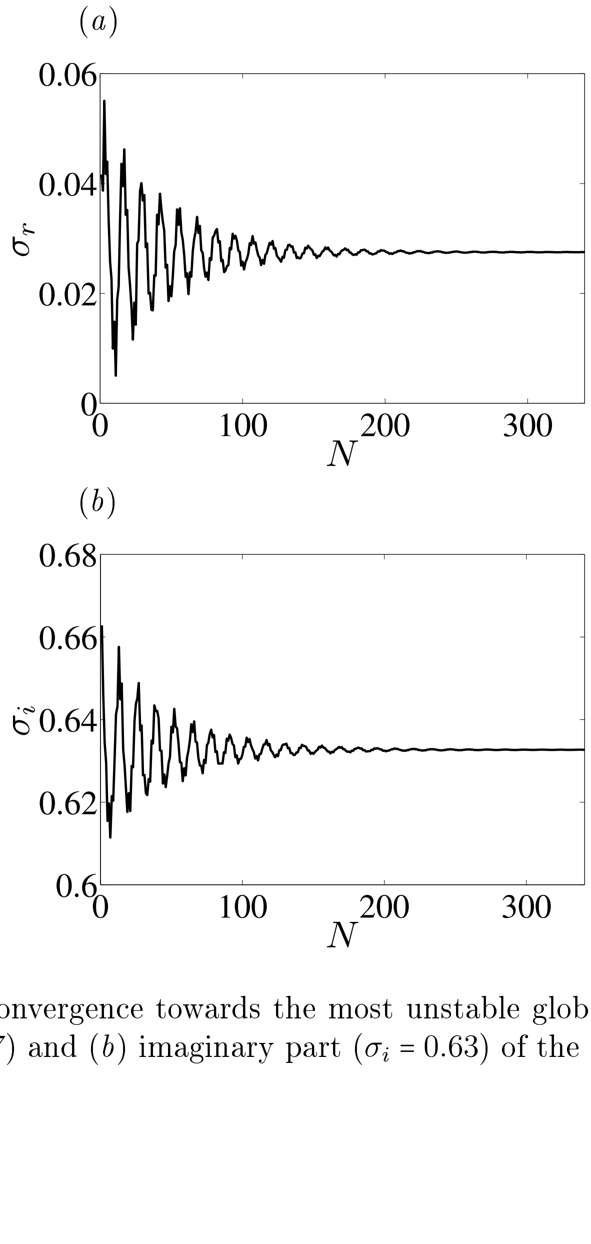

Figure 3.10: Convergence towards the most unstable global mode: (a) real part (σ_r = 0.027) and (b) imaginary part (σ_i = 0.63) of the global eigenvalue.

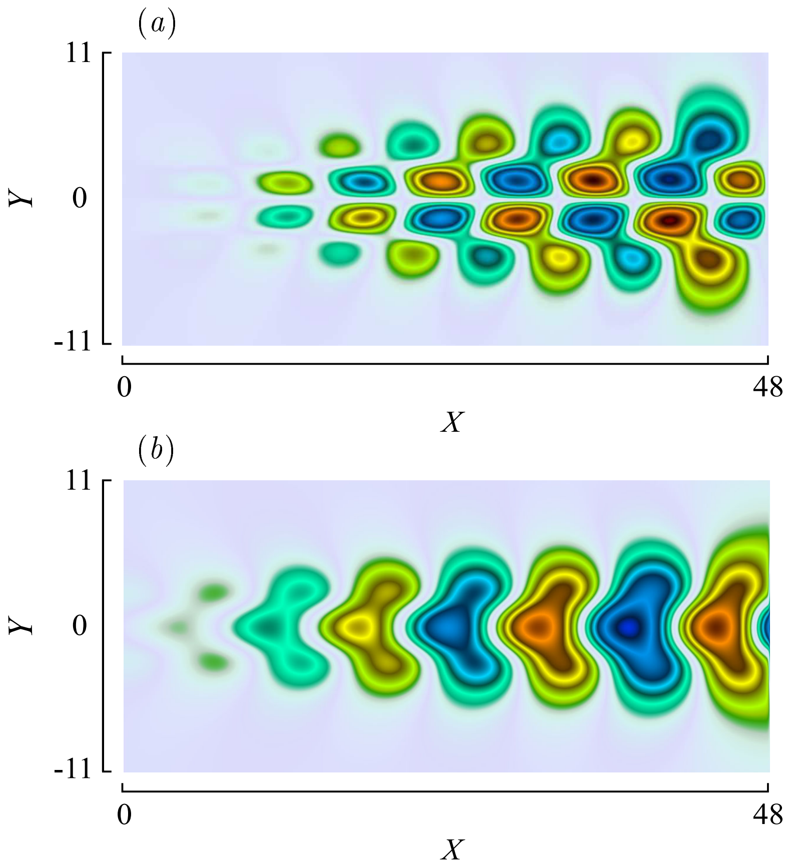

Figure 3.11: Most amplified global mode : real part of the streamwise and cross-stream velocity perturbation.

convective transition, the global mode is only weakly amplified while for the inlet III in the convectively unstable region, $\sigma_r < 0$ and the leading global mode is damped. This provides evidence that the existence of a finite region of absolute instability is also necessary in this highly non-parallel case for a global unstable mode to emerge.

3.4 Nonlinear disturbance evolution

The study of Marquillie and Ehrenstein (2003) showed that self-sustained oscillation of perturbation in the case of boundary layer separation over a double-bump structure results in the appearance of finite amplitude global mode, that is the global structure of the self-sustained perturbation saturates to a nonlinear oscillation of a finite amplitude. As well as the concept of absolute and convective instability for the local linear stability, a nonlinear instability can be either nonlinearly stable, nonlinearly convectively unstable, and nonlinearly absolutely unstable. A flow system is said to be nonlinearly stable if a system undergoes a finite initial perturbation relaxes back to its unperturbed state everywhere in the flow domain whatever moving frame of observation is considered. A flow system is said to be nonlinearly convectively unstable if a system undergoes a finite initial perturbation relaxes ultimately back to its unperturbed state at every fixed location in the flow domain, while the perturbation evolves to a nonlinear saturation in a moving frame of observation being convected downstream, that is the upstream front of the traveling wave has a positive velocity (positive in the sense of the downstream direction). It is nonlinearly absolutely unstable if the perturbation having negative upstream front velocity grows and reaches a nonlinear saturation. A nonlinear self-sustained oscillations may be triggered by having a finite domain of locally absolutely unstable region. Couairon and Chomaz (1996) demonstrate the relation between nonlinear global mode and local instabilities of a basic state by considering a one dimensional Ginzburg-Landau system in a semi-infinite domain. They showed that a nonlinear global mode, which a nonlinear saturated steady solution, may exist even the basic state is stable or rather convectively unstable.

For the case of finite region of local absolute instability in a flow domain, Pier and Huerre (2001) performed a study on the linear as well as the nonlinear stability behaviour of a synthetic wake flow. They showed, by examining the associated frequency spectra of the developed self-sustained nonlinear travelling wave at three different stations in the domain, that any station in the flow domain is tuned to a same global fundamental frequency. While the station closer to the absolute instability region (according to the locally parallel linear stability analysis) shows an almost sinusoidal time variation, the other stations off center situated further downstream show the excitation of harmonics. This case demonstrate the role of locally absolute region as a wave maker.

To asses how the global instability evolves when considering the full nonlinear Navier-Stokes equations for the present momentumless wake, the same numerical procedure as described above has been used, only now we have the following nonlinear Navier-Stokes equation

$$\frac{\partial}{\partial t}\mathbf{u} = -(\mathbf{u}\cdot\nabla)\,\mathbf{u} - (\mathbf{U}\cdot\nabla)\,\mathbf{u} - (\mathbf{u}\cdot\nabla)\,\mathbf{U} - \nabla p + \frac{1}{Re_0}\nabla^2\mathbf{u}\,, \tag{3.49}$$

that is by adding the nonlinear term $-(\mathbf{u}\cdot\nabla)\,\mathbf{u}$ to the right-hand side of the linearised Navier stokes system. Consequently, the time integration described in Appendix B needs to be adapted, that is the term $f^{(n,n-1)}$ given by relation (B.5) becomes now

$$\mathbf{f}^{(n,n-1)} = -4\tau\mathbf{u}^{(n)} + \tau\mathbf{u}^{(n-1)} + Re\left[(\mathbf{U}\cdot\nabla)\,\mathbf{u} + (\mathbf{u}\cdot\nabla)\,\mathbf{U} + (\mathbf{u}\cdot\nabla)\,\mathbf{u}\right]^{(n,n-1)}\,. \tag{3.50}$$

The same Gaussian-type initial condition (3.48) is considered, choosing an amplitude $A = 10^{-2}$. The inlet corresponds to $Re_0 = 20$ and the domain is reaching from I to IV (cf. figure 3.8(a)). The spatial discretizations are chosen to be the same as for the global stability analysis and a semi-implicit time marching is used. The position in space where the initial perturbation is triggered is the same as in the global linear computation. In its initial stage, the perturbation grows while spreading in the flow domain. The initial perturbation then evolves and eventually reaches a globally tuned structure having a fundamental frequency. It has been assessed by performing additional direct numerical simulation, that when triggering the initial perturbation right inside the locally absolutely unstable region, the same nonlinear structure and fundamental frequency along with its harmonics are recovered.

The instantaneous vorticity perturbation and the total vorticity in the fully nonlinear regime (at $t = 1140$) is shown in figure 3.12 while images of instantaneous streamwise and cross-stream velocity perturbation are depicted in figure 3.13. They show a small amplitude perturbation near the inlet suggesting the wave maker role of the locally absolutely unstable region. In figure 3.12(b), alternating vortices array with upper vortices having positive sign (counter clockwise circulation) and lower vortices having negative sign (clockwise circulation), which is a typical wake pattern called the reversed Bénard-von Kármán vortex street, can be observed in the second half of the flow domain. This is very different from the resulting wake pattern in the

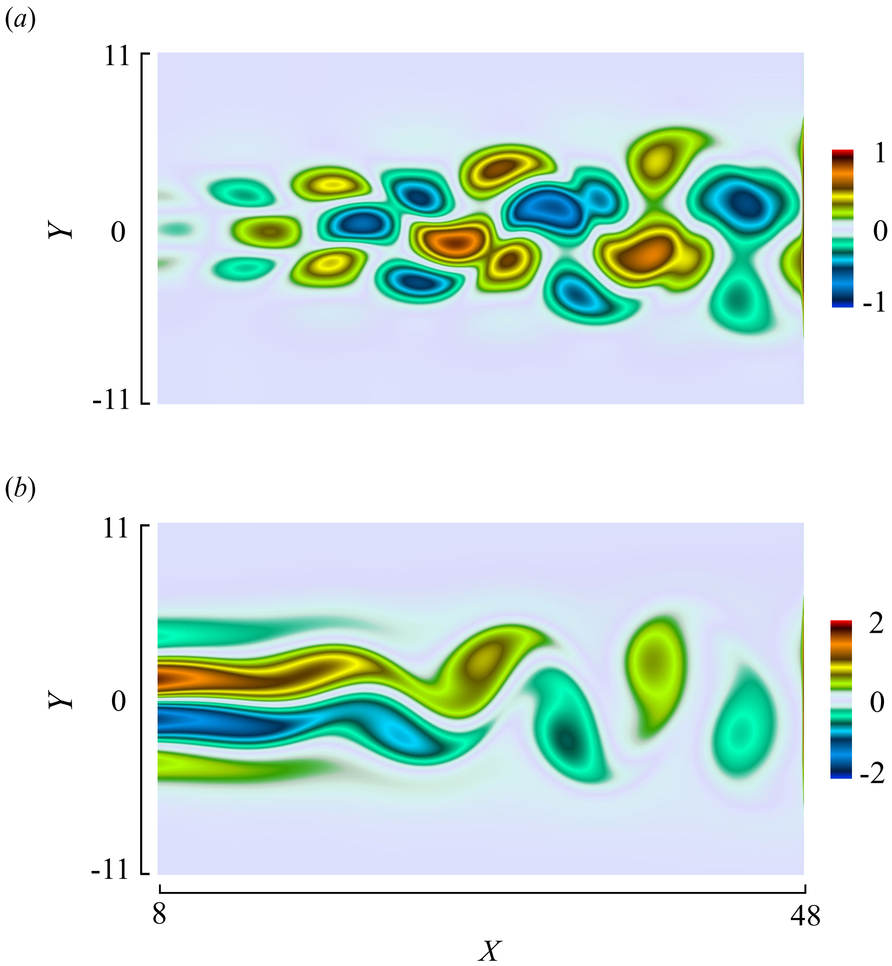

Figure 3.12: Instantaneous field structures: (a) vorticity of the perturbation and (b) total vorticity at $t = 1140$.

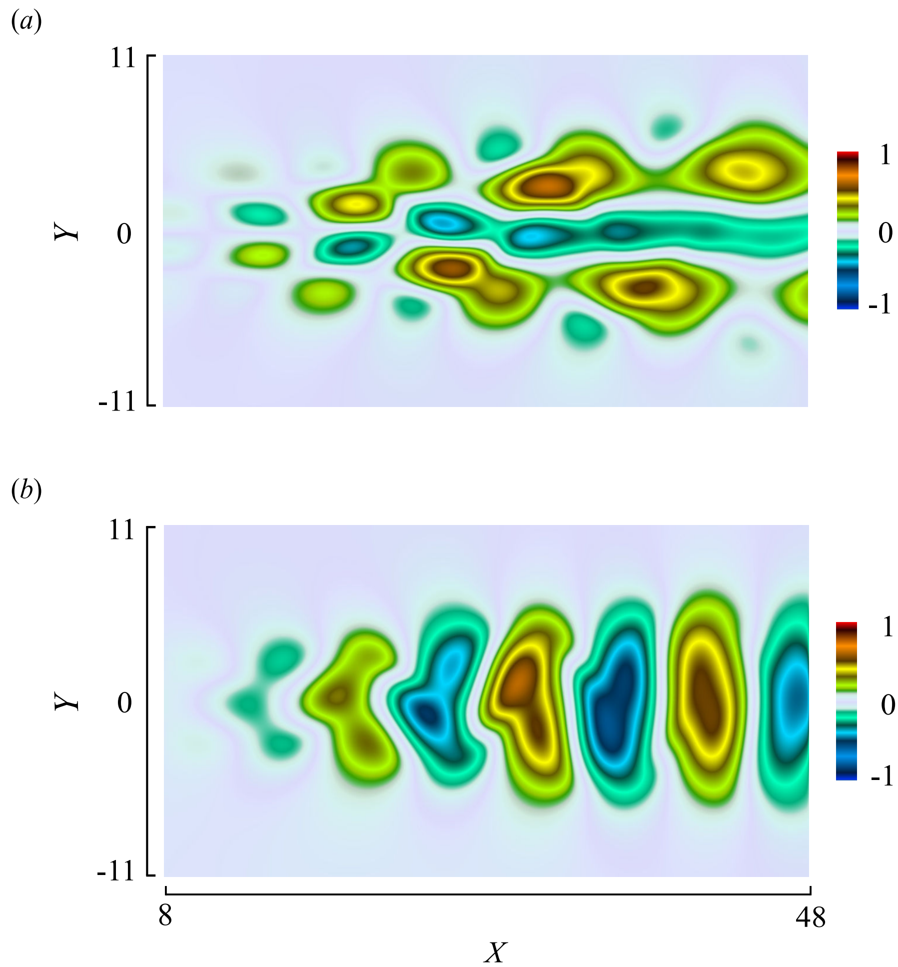

Figure 3.13: Instantaneous field structures: (a) streamwise velocity perturbation and (b) cross-stream velocity perturbation at $t = 1140$.

case of velocity deficit flow as shown for instance in Pier & Huerre (2001) which takes the form of a Bénard-von Kármán vortex street.

From the time evolution of the perturbation (figure 3.14), frequency spectra associated to the nonlinear dynamics can be calculated. The frequency spectra have been computed at two different locations slightly off the centerline: $(X, Y) = (20, 1.06)$ and $(X, Y) = (40, 1.06)$. Figure 3.15 shows that the global nonlinear structure is tuned to a unique fundamental frequency of $\sigma_i = 0.646$ (the harmonics being visible as well), which is in agreement with the frequency of the linear global mode (with a frequency of $\sigma_i = 0.63$). At a station $(X, Y) = (0.4, 1.06)$ near the inlet, the fluctuations of the perturbation are however nearly sinusoidal. This can be shown by computing its frequency spectra (given by figure 3.16) from its time evolving perturbation. It is now apparent that the global nonlinear structure in terms of the reversed Bénard-von Kármán vortex street is determined by the imposed locally absolutely unstable basic flow profile at inflow. Some other Navier-Stokes computations have been performed by considering the domain's inlet inside the convectively (according to the local stability analysis) unstable region. In these simulations no wave maker type behaviour was encountered, the initially triggered perturbation being washed away. This clearly shows that in the present case, an upstream finite absolutely unstable region is necessary for a self-sustained oscillation dynamics.

3.5 The Oseen solution

In the present analysis, the base flow is obtained in the Stokes approximation and using the Oseen assumption. This may be debatable at first glance since the underlying base flow is not the solution to the full Navier-Stokes equations. One may expect that the Oseen solution may undergo transient development when it is used as an initial condition for the full Navier-Stokes system. To assess the reliability of this approximation, the Oseen solution has been considered as the initial condition for the full Navier-Stokes system which has been integrated in time. The Oseen solution profile is held fixed at the inlet as a Dirichlet boundary condition and at outflow an advective boundary condition (similar to that for the flow perturbation in §3) is considered. It is observed that inside the domain, the Oseen solution slightly evolves from $t = 0$ to $t = 20$ (see figure 3.17), but then the profile undergoes no significant change any more until $t = 165$. These quasi-steady profiles slightly different from the steady Oseen solution have been considered for local stability computations, focusing in particular on position of absolute to convective instability transition. This new transition is found roughly at

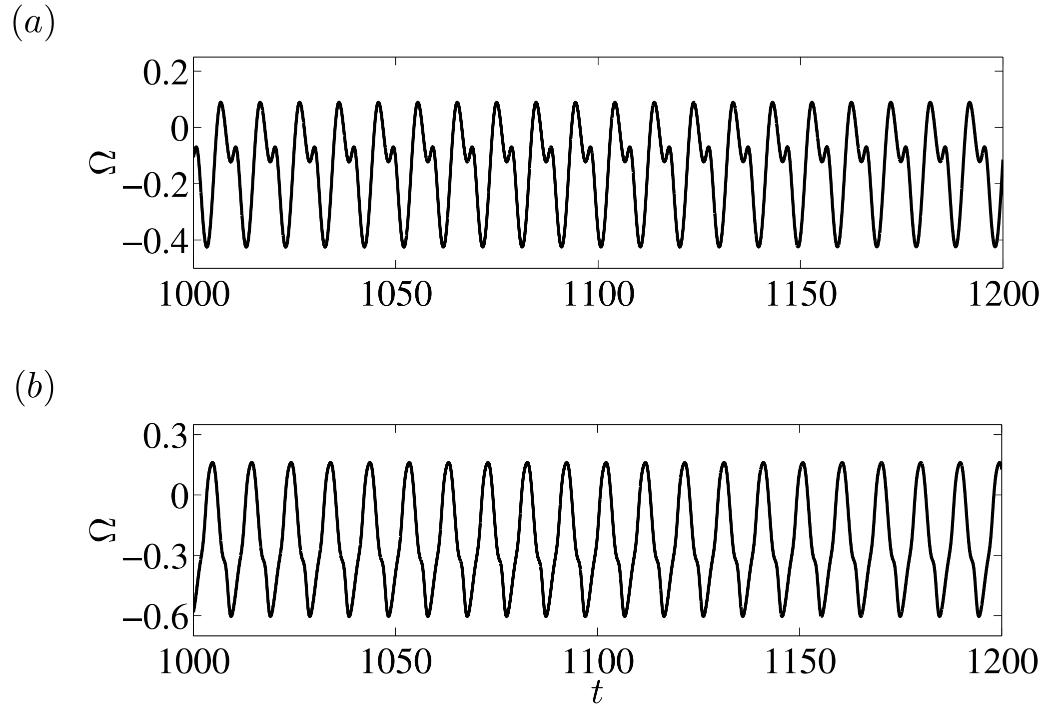

Figure 3.14: Evolution of vorticity perturbation in time recorded at (a) $(X, Y) = (20, 1.06)$ and (b) $(X, Y) = (40, 1.06)$. Both signals exhibit the same fundamental frequency $\sigma_i = 0.646$ (figure 3.15).

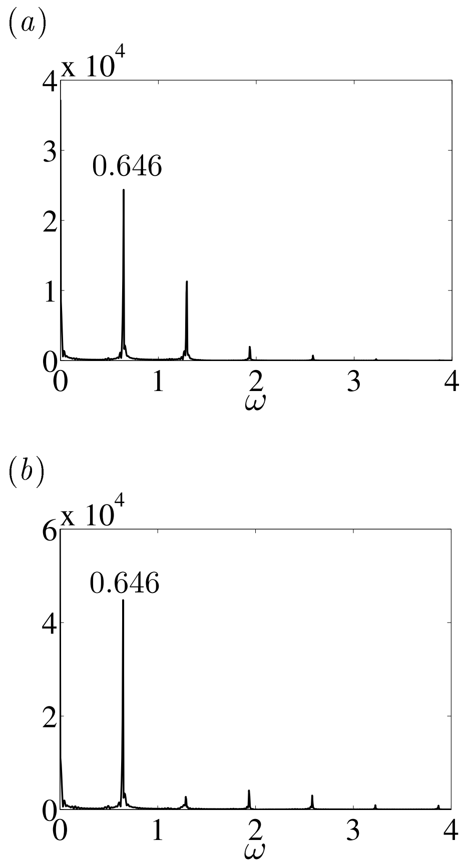

Figure 3.15: Frequency spectra of the vorticity perturbation shown in figure 3.14 for the time range $400 \le t \le 1200$.

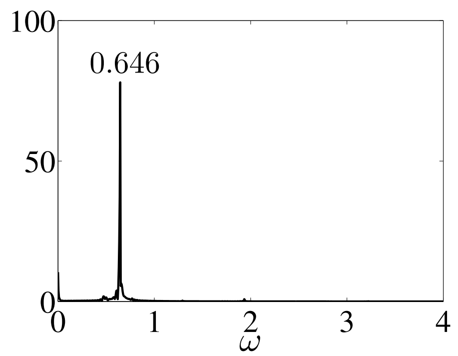

Figure 3.16: Frequency spectra of vorticity perturbation for the time range $400 \le t \le 1200$ recorded at $(X, Y) = (0.4, 1.06)$. Almost no harmonic observed.

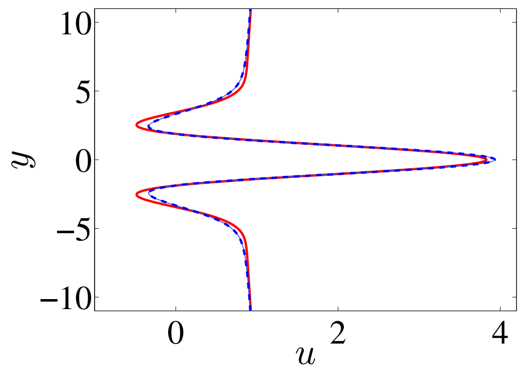

Figure 3.17: Evolution of the steady Oseen solution from $t = 0$ (solid line) to a new profile at $t = 20$ (dashed line) for $Re = 20.78$.

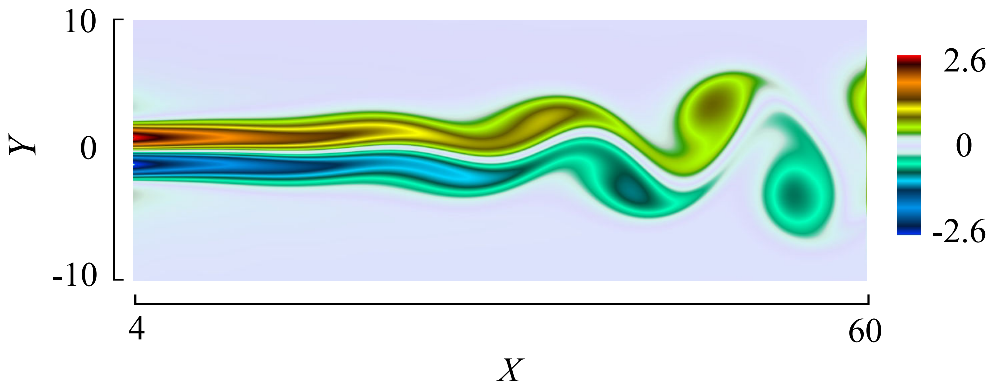

Figure 3.18: Instantaneous vorticity field structure at $t = 750$.

$Re = 20.8$ which is quite close to the value of $Re = 21.83$ (cf. figure 3.8(a)) for the pure Oseen profile.

Pursuing the time integration of the Navier-Stokes system where the Oseen solution has been used as initial condition, the flow starts to oscillate (for $t > 165$) and ultimately the flow dynamics reaches nonlinear saturation. The vorticity pattern is shown in figure 3.18 and the reverse von Karman vortex street similar to figure 3.12(b) is observed. Frequency spectra of the flow are depicted in figure 3.19 which shows that the flow is tuned to a frequency of 0.66. This frequency is close to 0.646 found in the analysis of section §4 with the Oseen approximation as the base flow.

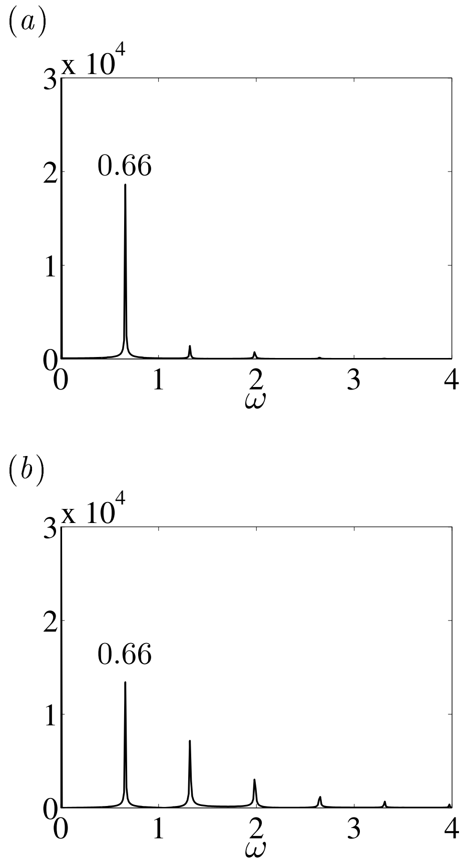

Figure 3.19: Frequency spectra of the vorticity in time recorded at two stations off-center: (a) $(X,Y) = (30,-2.2)$ and (b) $(X,Y) = (40,-2.2)$, for the time range $750 \leq t \leq 1200$.

Chapter 4

Application to swimming animals

In this part, we will see how the results we have obtained from previous chapters may be put in the context of swimming animals. Firstly, we discuss the transition from absolute to convective instability and what it implies. Two different cases with different Reynolds number regime (based on the body length) are discussed for this particular matter. Secondly, we discuss the comparison of the present momentumless wakes with velocity excess profiles usually used in connection with the "wake resonance theory" (Triantafyllou et al., 1993). The velocity excess profile we consider is no other than the thrust component extracted from the momentumless wake. Then we discuss the limit of validity of the present results by considering the doublet model as a momentumless wake generator.

4.1 Absolute instability

Figure 3.7(a) shows that, when the force doublet intensity is large enough ($Q \gtrsim 100$), the near wake (corresponding to small Re) is always absolutely unstable. Moving further away from the doublet, there is first a transition from absolute to convective instability, and then to stability. The existence of an absolute region is important, because, in that case, the wake is expected to behave like an oscillator triggering a self-sustained instability process.

To examine the consequences of the present stability analyses on a swimming animal, we consider a self-propelled body of length L^* and moving at a constant speed U^*. In two dimensions, the skin friction drag (per unit length) exerted on this swimmer is of the order of

$$F^* \sim \rho^* {U^*}^2 L^* Re_{L^*}^{-1/2}, \tag{4.1}$$

which is nothing else than the Blasius boundary layer law (Schlichting and

Gersten, 2003), where $Re_{L^*} = U^*L^*/\nu^*$ is the Reynolds number based on body length.

For a constant swimming speed, this drag has to be balanced by an equal but opposite thrust. Assuming that the points of application of these two forces are separated by a distance of order L^*, the dimensional force doublet intensity can be estimated to be

$$Q^* = \frac{F^*L^*}{\rho^*} \sim U^{*3/2}L^{*3/2}\nu^{*1/2}. \tag{4.2}$$

At the transition from absolute to convective instability, recall that we found $Q = 18.4\,Re^3$ for $Re > 20$. By recalling that $Re = U^*\delta^*/\nu^*$ and by using the definition of Q in (2.18), we can infer the following relation

$$\delta^*_{ac} = \frac{0.38}{U^*}\left(Q^*\nu^*\right)^{\frac{1}{3}}, \tag{4.3}$$

which states that the value of δ^* corresponding to the absolute–convective transition (denoted by δ^*_{ac}), can be estimated from Q^*, U^* and ν^*. Following the same line of reasoning, the neutral stability curve corresponds to $Q = 35.22\,Re^2$ for $Re > 10$ (figure 3.7a) and is associated to a critical δ^* above which the wake is stable

$$\delta^*_c = \frac{0.17}{U^*}Q^{*\frac{1}{2}}. \tag{4.4}$$

Let us first consider a fish swimming in water ($\nu^* = 10^{-6}\,\mathrm{m^2\,s^{-1}}$) having body length $L^* = 10\,\mathrm{cm}$ and moving with a velocity $U^* = L^*\,\mathrm{s^{-1}}$. Based on (4.2), we have $Q^* \approx 10^{-6}\,\mathrm{m^4\,s^{-2}}$. By substituting these values into (4.3) and (4.4), we find $\delta^*_{ac} = 0.38\,\mathrm{mm}$ and $\delta^*_c = 1.6\,\mathrm{mm}$. These values are far smaller than the width of the wake right behind the beating tail or even the tailbeat amplitude itself, which is generally about one fifth of the body length (Videler, 1993). For a 1 cm fish moving with $U^* = L^*\,\mathrm{s^{-1}}$ we have $Q^* \approx 10^{-9}\,\mathrm{m^4\,s^{-2}}$. Thus we obtain $\delta^*_{ac} = 0.38\,\mathrm{mm}$ (3.8% L^*) and $\delta^*_c = 1.6\,\mathrm{mm}$ (5.4% L^*) which are more reasonable. This means that, for a fish, the wake is likely to lie entirely in the stable region as shown in figure 4.1.

Now consider the case of a swimming ascidian larva. The hydrodynamics of locomotion for these small swimmers has for instance been addressed in McHenry et al. (2003), focusing in particular on the relative contribution of viscous and inertial forces for the production of thrust and drag during steady undulatory swimming. The larva's body is divided into a spherical trunk and a tail with a rectangular cross section, modelling the skin friction of the trunk using the Stokes law (Batchelor 1967), valid for very low Reynolds numbers, the skin friction of the tail being modelled using the Blasius boundary layer law with a correction taking into account the wall normal velocity of the

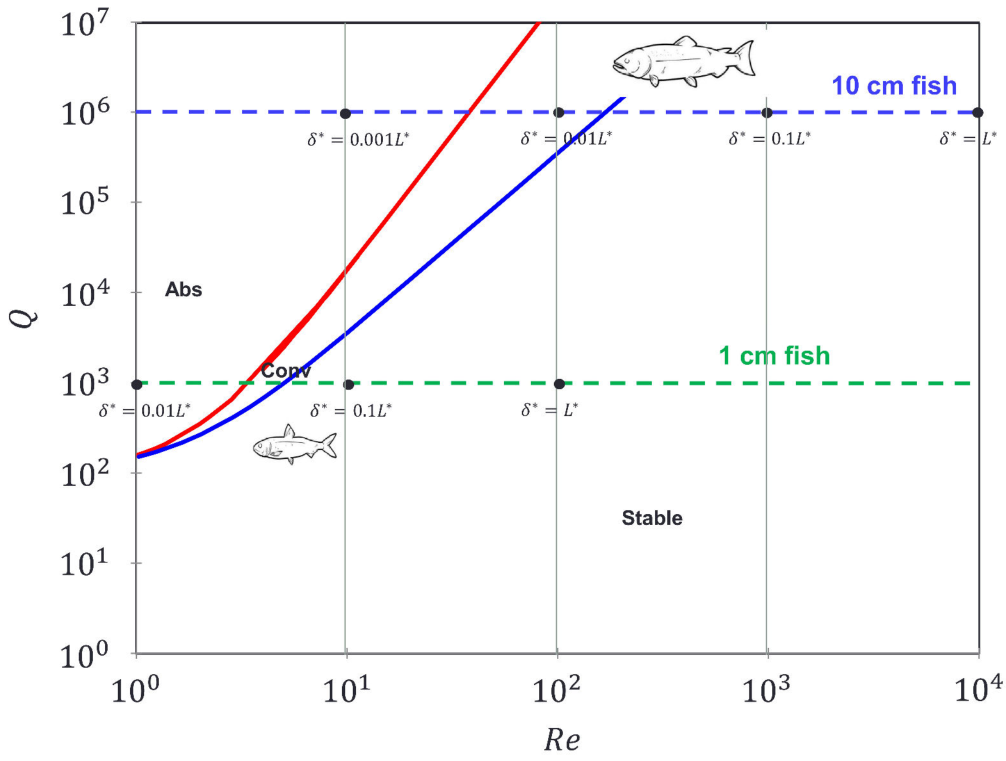

Figure 4.1: Stability diagram for the determined parameters Q and Re for 1 cm and 10 cm fish swimming with $U^* \sim L^* \mathrm{s}^{-1}$.

undulatory swimming. The authors provide evidence, that only for small Reynolds numbers ($Re^*_L < 10$) the drag is almost entirely due to skin friction. However, the contribution of form drag is becoming increasingly important as one considers cases corresponding to higher Reynolds numbers.

In McHenry et al. (2003), the model is validated by comparisons with measurements of thrust produced by ascidian larvae of body length $L^* = 1.9$ mm, the provided thrust value being approximately 6×10^{-6} N for a mean swimming speed of about 31 mm s^{-1}. The corresponding Reynolds is $Re^*_L = 58.9$ and the two-dimensional skin friction Blasius drag formula (4.1) used here would predict a drag force (per unit length) of $\sim 2.4 \times 10^{-4}$ N/m. Although the extrapolation of a two-dimensional model to a three dimensional body geometry is problematic, one may consider the analysis in Ehrenstein et al. (2014), who addressed numerically the boundary layer of a periodically flapping plate with finite width in uniform incoming flow, assessing the longitudinal skin friction force (per unit length) expression, at the plate's section normal to the uniform flow, $F^*_{3D} = C_{3D}\sqrt{r < |U_\perp| >}\rho^* {U^*}^2 L^* Re_L^{-1/2}$, with r the plate's width to length ratio and $< |U_\perp| >$ the mean absolute value of the dimensionless (with the swimming speed) periodic wall-normal velocity, the coefficient C_{3D} being ≈ 1.8. This expression is hence equivalent to (4.1), for a conveniently chosen coefficient of proportionality (assuming a simple plate motion with a constant value $< |U_\perp| >$).

It is however hardly possible to precisely connect this formula to the larva case, given that in Ehrenstein et al. (2014) only simple flapping motions have been considered and it is also questionable whether these results (obtained for Reynolds numbers higher than 100) can be extrapolated to the present low Reynolds number regime. Furthermore, in McHenry et al. (2003) it is shown that for Reynolds numbers $Re > 10$ inertial (form) forces absent in our model increasingly contribute to the drag. Assuming nevertheless this drag force law and multiplying the above expression by the larva's measured length, one gets the skin friction drag force of $C4.6 \times 10^{-7}$ N, which is to be compared to the measured thrust of 6×10^{-6} N, given the uncertainty of the value of the unknown multiplicative constant C.

Subtituting the measured larva data into formula (4.2), one finds a value $Q^* \approx 4.5 \times 10^{-10}\,\mathrm{m^4\,s^{-2}}$. Using (4.3), we then find $\delta^*_{ac} \approx 0.094\,\mathrm{mm}$ and $\delta^*_c = 0.12\,\mathrm{mm}$, which correspond to about 5% and 6.3% of the body length respectively. In this particular case, the wake is thus likely to be unstable and there may even be an absolute-convective transition in the near wake, provided that our model applies at least qualitatively to this swimming ascidian larva case. It is however unclear whether the instability properties of the wake will affect the swimmer performance since the instability cannot produce momentum.

4.2 Momentumless wake vs. jet wake

Triantafyllou et al. (1993) proposed that the swimming efficiency of a self-propelled body reaches a maximum when there is a resonance between the frequency of the wake instability and the tailbeat frequency. As it has already been noted in the introduction, the wake profiles considered by Triantafyllou et al. (1993) are jets with a net positive momentum. In the case of animal swimming with constant velocity, the balance between thrust and drag results in momentumless wakes. The separation between thrust and drag often becomes difficult, especially in the case of anguiliform swimmers such as eels where almost all body parts produce drag and thrust simultaneously.

Bale et al. (2014) proposed a drag-thrust decomposition which shows that this separation can be performed. Although Tytell and Lauder (2004) suggested the idea of temporal and spatial separation of thrust and drag which gives zero total force on average since drag and thrust may appear to be intermingled, the drag-thrust decomposition proposed by Bale et al. (2014) does not rely on spatio-temporal decomposition. The idea is to separate body movements that produce drag and those that produce thrust such that the combination of resulting forces gives back the original observed value and while the combination of the decomposed movements recovers the observed movement. The proposed decomposition procedure is as follows. Suppose that one observes a swimming body with generic wave in the form of backward travelling wave of velocity c_w and lateral movement velocity of $U_\perp$ with no amplitude variation in longitudinal direction. The body swims with a constant velocity U. This generic wave can be decomposed into two kinds of movement. The first one is the slithering movement where any point on the body appears to follow a sinusoidal path. This movement occurs when the the swimming velocity matches the wave velocity of the backward travelling wave. Bale et al. (2014) used the term drag-causing slithering for this motion since fluid is dragged forward by the lateral movement of every point on the body. The second one is the backward frozen movement. It can be imagined as the wavy body is frozen and being drifted backward with a velocity equal to the difference between the velocity of the backward travelling wave and the forward velocity of the body. This movement is apparent when the velocity of the backward travelling wave is greater than the forward velocity of the body. This movement is thrust-causing motion since it causes fluid to be pushed backward and the reaction of fluids pushes the body forward. If we superimpose the two motions, we obtain the undecomposed generic body wave motion described earlier. Figure 4.2 shows the drag-causing and the thrust-causing motions along with their resultant.

The constant amplitude assumption used in this proposed drag-thrust decomposition however poses problem when one tries to apply it in the case of swimming animals. Swimming animals have amplitude variation as they form a wavy motion to create propulsion and this amplitude variation is different between every mode of swimming imposed by aquatic animals (see chapter §1 for the classification of swimming mode). However, Bale et al. (2014) shows, by examining four different animal, that the decomposition procedure can still be carried out for swimmers with small rate of amplitude change such as in the case of eel, larval zebrafish, and knifefish. Small rate of amplitude change means that the deviation from slithering motion is small rendering the decomposition is still meaningful for anguiliform and sub-carangiform swimmers. In the case of Mackerel (carangiform swimmer), they found a discrepancy between the expected undecomposed force and resultant of force obtained from the decomposition. This means that the decomposition does not apply to such carangiform swimmers since they have large rate

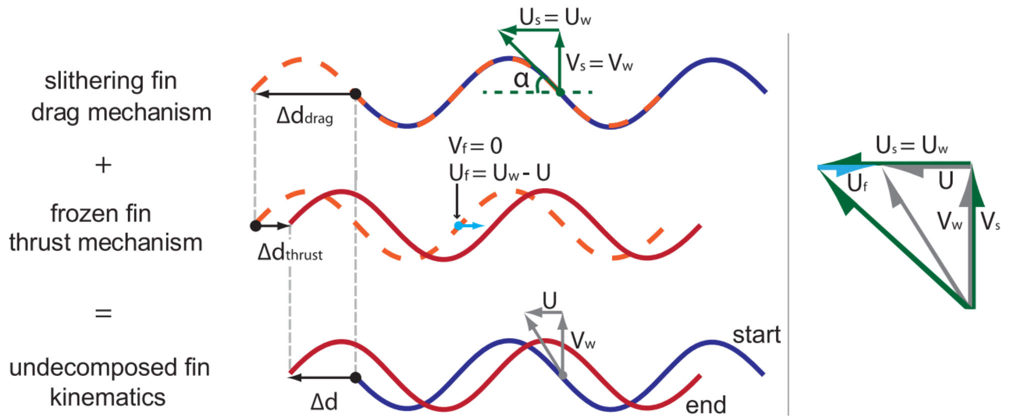

Figure 4.2: Kinematic decomposition of drag-causing motion and thrust-causing motion and the superposition of the two of them resulting the generic undecomposed kinematic. This figure is taken from Bale et al. (2014).

of amplitude change at the rear end (caudal part). Deviation from slithering motion is therefore large in this case.

In the present study, we consider momentumless wake profiles that can be decomposed into one part due to the thrust and one due to the drag. The decomposition however can be performed in a straightforward manner. The doublet model is derived from two opposite forces as given by (2.3) and obtained by taking the limit given by (2.5). Back to the formula of single force given by (2.13) and (2.15) we can construct the drag and thrust parts of their corresponding momentumless wake by considering finite separation distance between the two forces. To compare our results with those of Triantafyllou et al. (1993), we propose to use this decomposition and to extract the thrust part of our family of momentumless wakes and assess its stability properties.

We consider a swimming fish of body length L^* and wake half-width or tailbeat amplitude of about $\delta^* \approx 0.1L^*$ (which is approximately the case for most undulatory swimmers). Thrust is generally produced by the caudal fin or by the posterior part of the body Lighthill (1969), while skin friction is expected to decrease along the length of the body as boundary layer thickness increases. We can thus safely assume that the separation distance between the points of application of thrust and drag is in the interval $0.1L^* < \epsilon^* < L^*$, which means that the dimensionless doublet size is in the interval $1 < \epsilon < 10$. Now, using (2.19), we find that the force doublet intensity Q is connected to the thrust intensity J through the relation: $J = Q/(\epsilon\, Re)$.

We now compare the stability properties of the momentumless profiles and jet profiles. To do so, we have performed a linear stability analysis of

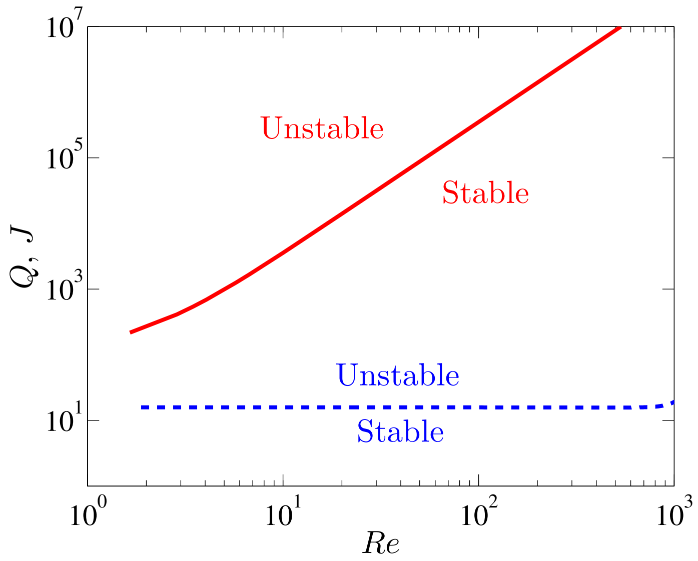

Figure 4.3: Stability diagram of a jet wake profile of intensity J (dashed line) and a momentumless wake profile of intensity Q (solid line).

the jet wake profile of intensity J given by (2.13), using a method similar to that explained in §3.1 for the momentumless wake profiles. The result of this analysis is shown in figure 4.3 together with the results of the momemtumless wake. In these stability diagrams plotted in the (Re, Q) or (Re, J)–plane, for a given doublet intensity Q and Reynolds number Re, the corresponding jet thrust intensity (for a specific ϵ) has to be chosen on the ordinate as $J = Q/(\epsilon\, Re)$ and the stability property may be inferred.

Using again the example of a $L^* = 10\,\text{cm}$ fish swimming at constant speed $U^* = L^*\,\text{s}^{-1}$, we have $Re = U^*\delta^*/\nu^* \approx 10^3$ and $Q = Q^*/(\nu^{*2}) \approx 10^6$. In that case, the momentumless wake is stable according to figure 4.3. Yet, its jet counterpart associated to the production of thrust only has an intensity $10^2 < J < 10^3$ (with $1 < \epsilon < 10$), which corresponds to an unstable wake profile. The same holds for larger or faster fish. Hence, for most fish, the momentumless wake is stable while the jet profile due to the thrust alone is unstable.

To go further, we plot in figure 4.4 three jet profiles for different values of ϵ together with their stability properties. As stated above, for these values of ϵ, the profiles are unstable ($\omega_i > 0$). Moreover, the (real) frequency ω_r associated to the maximum of ω_i is almost constant: $\omega_r \approx 0.5$. This frequency correspond to a Strouhal number based on the wake width A_{wake},

$$St \approx \frac{A_{\text{wake}}\,\omega_r}{2\pi}, \tag{4.5}$$

where A_{wake} is estimated as the y-distance between the two inflection points of the thrust profiles. By substituting the value of A_{wake} ($A_{\text{wake}} \approx 3.2$ for all values of ϵ) and ω_r into (4.5), the Strouhal number is found to be $St \approx 0.25$. This results is similar to the range of Strouhal number found by Triantafyllou et al. (1993) from stability analyses of experimental jet profiles: $0.25 < St < 0.35$. However, as it has already been noted above, the corresponding momentumless profiles, found when both thrust and drag forces are taken into account, are stable (and therefore Strouhal number can not be defined in that case). The physical basis for this difference is however unclear. It may be due to the fact that velocity gradients are smaller in norm for the momentumless wakes since the velocity increase due to the thrust tends to be compensated by the velocity deficit due to the drag. Indeed, computing the maximum, in norm, of the velocity gradient for the three jet profiles (figure 4.4), one finds approximately the values 0.12, 0.06, 0.01, for respectively $\epsilon = 1, 2, 10$, and the maximum values of the gowth rates decrease accordingly, as seen in figure 4.4(c). The maximum of the velocity gradient for the corresponding stable momentumless profile, not shown here, is however much smaller ($\approx 1.5\times10^{-4}$).

4.3 Limit of validity

We will now examine the limit of validity of the present results. We will first discuss the validity of the Oseen approximation. We will then examine if the exchange of momentum between the swimming body and the flow can be described by a force doublet. Finally, we will discuss how three-dimensional effects may affect the results.

It has been shown before that using the Oseen solution as an initial condition in the direct numerical simulation gives a similar results to that of perturbed Oseen base flow. The similarity of the results clearly lends credit to the justification of the Oseen assumption, at least for the relatively low Reynolds number considered.

The Oseen approximation has also been addressed in Gustafsson and Protas (2012), who performed a detail study on the solutions of the two-dimensional Oseen equations for the flow behind an obstacle for a broad range of Reynolds number (here, Reynolds number is based on the characteristic dimension of the obstacle). They compared their study with numerical simulations of Fornberg (1985) on a steady viscous flow around a two-dimensional

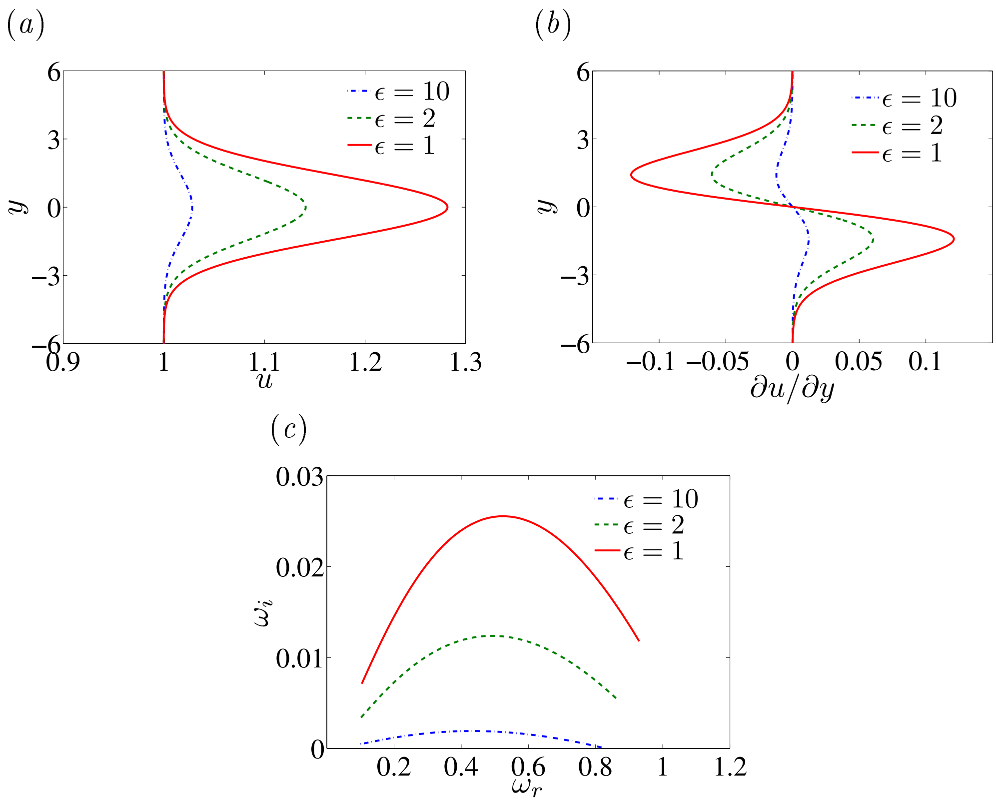

Figure 4.4: (a) Jet wake profiles of extracted thrust for three different values of ϵ and (b) their first derivative with respect to y. (c) Most unstable modes of the three Jet wake profiles. The parameters used are $Re = 10^3$, $Q = 10^6$, and $J = Q/(\epsilon\, Re)$.

cylinder. They concluded that the flow structures have a number of similarities with that of Oseen flow in terms of recirculation length, drag coefficient, and separation angle. However, these similarities can only be observed up to a Reynolds number of about 100. For higher Reynolds number, the Oseen approximation is therefore debatable. In the present context, we make the assumption that the family of momentumless wakes still *qualitatively* describe the flow even for large Reynolds number. This assumption could however be assessed in the future by performing stability analyses of different families of momentumless wakes (e.g. profiles obtained from averaged nonlinear numerical simulations).

The family of momentumless wake profiles used in the present study is obtained by assuming that the contribution of thrust (resp. drag) forces can be reduced on average to a point force. Further, we assume that the flow field is that of a force doublet, which means that we consider the far field, i.e. distances large compared to the separation distance between the points of application of thrust and drag. Yet, as we saw above, most of the instability properties of the flow are related to the near wake, where these hypotheses do not hold. Nevertheless, the family of wake profiles used here captures qualitatively the principal features of momentumless wakes: no net momentum, profiles parametrised by their amplitude and width. As already proposed above, it would be interesting to extend the present investigation by studying the stability of average profiles obtained from numerical simulations of self-propelled bodies.

Finally, one may wonder how the present two-dimensional results may generalise to three dimensions. First, it should be noted that the flow behind swimming animals is generally “very three-dimensional”, or said differently, the wake in a given horizontal slice may appear to have a positive or negative momentum depending on its depth (Nauen and Lauder, 2002; Müller et al., 1997; Drucker and Lauder, 2000; Lauder and Drucker, 2002). The only exception seems to be the flow behind eels Tytell and Lauder (2004) and, of course, two-dimensional numerical simulations. An interesting avenue for future works would be to extend the stability analyses to three dimensions. But, at the present time, it is difficult to extrapolate our two-dimensional results to three dimensions. It is however safe to assume that the stability properties of a momentumless wake and its jet part will still be very different, even in three dimensions.

Chapter 5

Conclusions and perspectives

5.1 General conclusions

In this study, a linear stability analysis of a family of momentumless wake profiles has been performed. As a base flow, we used the flow generated by a translating force doublet in the Oseen approximation, as initially proposed by Afanasyev (2004). This flow takes into account the opposite drag and thrust that are exerted on average on a self-propelled body swimming at constant speed U^*. For this family of momentumless wakes, a transition from absolute to convective instability has been found, in contrast with the jet profiles usually considered for bio-inspired wakes, which are only convectively unstable. Within the locally parallel flow assumption, it has been found that this absolute-convective transition occurs at

$$\delta^*_{ac} = \frac{0.38}{U^*} \left(Q^* \nu^*\right)^{\frac{1}{3}}, \tag{5.1}$$

where δ^* is a measure of the wake half-width and Q^* is the intensity of the force doublet. This value is too small to be meaningful for fish longer than about 1 cm. It may however be relevant for swimming organisms with low Reynolds number (based on the body length of the swimmers) such as tadpoles or larvae.

In this study, we also performed a global stability analysis in both linear and nonlinear regime for the family of momentumless wakes that exhibit relatively strong non-parallelism. The time-stepper technique, along with the modified Rayleigh iteration, proved to be quite successful to isolate the most unstable global mode. The existence of a global instability behaviour tuned at a specific frequency has been found whenever the wake's inflow boundary is chosen in the local absolute instability region. Having inflow boundary close to the transition from local absolute to convective instability, the flow is weakly unstable, while the flow is damped when the inflow boundary is chosen in the local convective instability region. The self-sustained structure have been shown to be a reversed Bénard-von Kármán vortex street and resulting from the locally absolutely unstable region. This absolutely unstable region acts as a wavemaker creating waves that will in turn develop downstream into a nonlinear wavetrain. The nonlinear development of the wake showed a nonlinear saturation in which harmonics are excited in the wake further downstream, while the local dynamic is almost sinusoidal near the inlet. The fundamental frequency in the nonlinear stability regime matches the frequency of oscillation obtained from the global linear stability analysis.

For a specific dimensionless intensity of the force doublet, possibly in the range of centimetre size swimming organisms, the Oseen approximation used has been validated by performing a direct numerical simulation where the Oseen solution was considered as an initial condition for the full Navier-Stokes system. For the boundary conditions, the Oseen solution at the inlet was held fix as a Dirichlet boundary coundition and an advective boundary condition was used for the outlet. After long-time evolution, using this Oseen solution as an initial condition, the wake also evolved into a nonlinear wave train. The transition from absolute to convective instability however moved closer to the inlet. It has also been shown that this setting shows a transient evolution of the Oseen solution to a new quasi-steady state before oscillations took place. Eventually a nonlinear saturation was also reached and the frequency spectra (showing the fundamental frequency and its harmonics) could be obtained. The fundamental frequency has a value close to the case where the Oseen solution was used as a base flow. The reversed Bénard-von Kármán vortex street was also observed.

From the momentumless wake profiles the thrust part can be extracted. By performing a local stability analysis on the thrust wake, when the thrust is intense enough, the corresponding jet profile is found to be (convectively) unstable, even though the momentumless wake from which it has been extracted may well be stable. Although further investigations on the Oseen approximation, different wake profiles, and three dimensions may be required, the present analysis demonstrates that physical interpretations of swimming efficiency based on jet wakes have to be taken with great care and cannot be easily transposed to a whole self-propelled body. In other words, for swimming animals, the selection of Strouhal number through a “wake resonance”, as originally proposed by Triantafyllou et al. (1993) and later revisited by Moored et al. (2014), seems to be unlikely.

5.2 Perspectives

The model used in this study is derived by considering a force doublet in the Oseen approximation which limit its applicability. Deriving a force formulation from the full Navier-Stokes equations is tantalizing since it would lead to various applications in a wide range of Reynolds numbers. One other interesting way would be to construct the average wake profile from a direct numerical simulation or from measurements to assess its stability locally and globally both in linear and nonlinear regime. Full three-dimensional direct numerical simulations, however, require large computational resource and may be challenging.

Standard PIV techniques, which in principle measures flow field on a plane, requires assumptions one tries to avoid for a full 3D reconstruction of the wake. However, the volumetric imaging technique described in chapter 1 used by Flammang et al. (2011) may be useful for this purpose. The momentumless wake may then provide drag and thrust simultaneously. However, another problem would naturally follows once the full three dimensional wake structure is obtained. It is the problem of extracting thrust and drag from the wake (drag-thrust separation). More appropriate method to separate both forces is required and needs to be confirmed by direct numerical simulation. Although, Bale et al. (2014) had proposed a kinematic decomposition of drag and thrust which does not rely on spatio-temporal separation, many fish swim by imposing body movements that deviate form perfect slithering, rendering the proposed separation has also been limited to small rate of amplitude change.

The wake unsteadiness has also been beyond the scope of this study. Although, in the context of swimming animals, the average forces can be seen to be in equilibrium for an animal moving with constant velocity, producing a momentumless wake, thrust generation however varies during strokes. For a sinusoidal stroke, maximum thrust generation is achieved when the tail is in its zero amplitude position while minimum thrust generation is achieved when the tail reaches its maximum amplitude and changes its direction. One may say that a swimming activity can be seen to have short period of acceleration and deceleration. Therefore to take into account the unsteadiness in swimming, one might want to revisit a spatio-temporal separation of drag and thrust.

Appendices

Appendix A

Validation

As a comparison and validation to our procedure, here we briefly address, whether single force profiles of type (2.13) may capture conventional mean wake profile characteristics taken from literatures by appropriately tuning the parameters. As an example, we consider the profile proposed by Monkewitz (1988) and given by

$$U(y) = 1 - \Lambda + 2\Lambda F(y) \tag{A.1}$$

$$\Lambda = (U_c^* - U_{max}^*)/(U_c^* + U_{max}^*) \tag{A.2}$$

$$F(y) = (1 + \sinh^{2N}(y \sinh^{-1}(1)))^{-1}. \tag{A.3}$$

For particular values of the parameters ($\Lambda = -1.105$ and $N = 1.34$, at $Re = 12.5$) the stability characteristics of the Monkewitz's profile have been recomputed, showing that the flow is absolutely unstable, the absolute frequency and wavenumber being

$$\omega_0 = 0.952 + i0.058, \quad \alpha_0 = 0.8 - i0.505. \tag{A.4}$$

These values are approximately equal to the values computed by Monkewitz (1988) (see table I, page 1004), the small differences being probably due to a better convergence here.

A single force streamfunction given by (2.6) can be, by appropriately choosing the parameters, fitted to the generic profile proposed by Monkewitz (1988) (Figure A.1), by following the same non-dimensionalisation as in this latter paper. We find that the best fit is obtained for $x = 5$ and $J = J^*/(2\pi l^* {U^*}^2) = -0.804$ (l^* being the reference length), when a constant velocity equal to 2 is added to the streamwise velocity.

We then performed the local stability analysis of this single force profile and found that the absolutely unstable mode corresponds to

$$\omega_0 = 0.956 + i0.031, \quad \alpha_0 = 0.8 - i0.505. \tag{A.5}$$

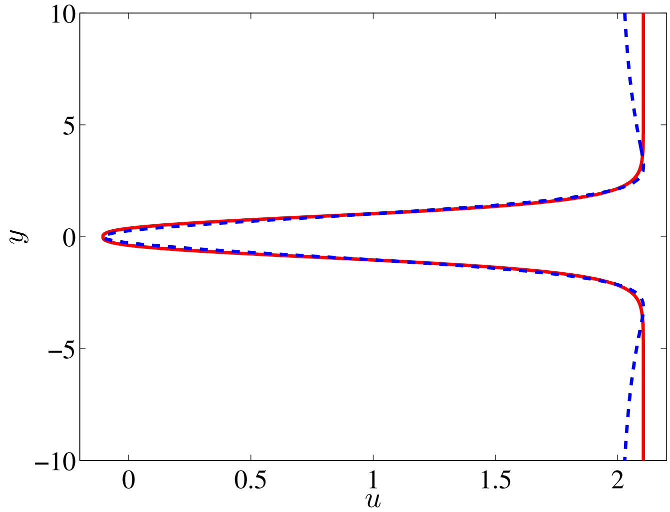

Figure A.1: Singlet force profile (dashed line) fitted to a generic bluff-body wake profile proposed by Monkewitz (1988) (solid line).

These values are quite close to what was found for the generic profile proposed by Monkewitz (1988), the amplification rate being slightly lower. Treating the Reynolds number as an independent parameter, we found that the transition from absolute to convective instability is approximately at $Re = 9.75$ with

$$\omega_0 = 0.945, \quad \alpha_0 = 0.8 - i0.505. \tag{A.6}$$

This value of Reynolds number for the transition from absolute to convective instability is similar to the result of Monkewitz (1988) (see Figure A.2).

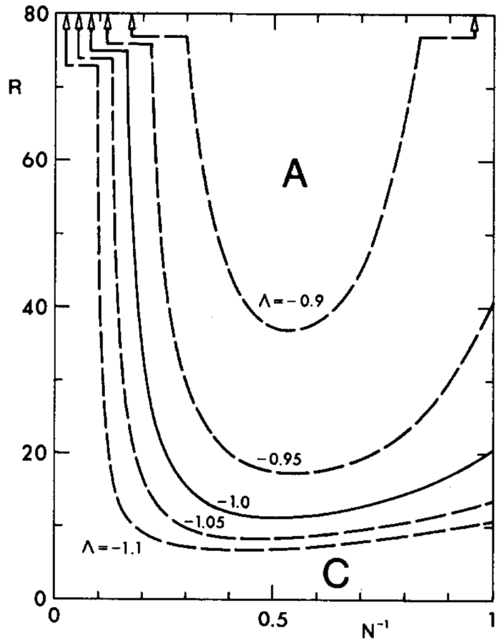

Figure A.2: Stability region of the Monkewitz profile in parameter space Re-N^{-1} for different values of Λ (Monkewitz (1988), figure 2, page 1001).

Appendix B

Details of numerical procedures

B.1 Discretisation in the streamwise direction

The first derivative is approximated by eight-order finite difference and the formula is given by

$$\left[\frac{df}{dx}\right]_k = \frac{1}{\Delta x}(\frac{1}{280}f_{k-4} - \frac{4}{105}f_{k-3} + \frac{1}{5}f_{k-2} - \frac{4}{5}f_{k-1} + \frac{4}{5}f_{k+1} - \frac{1}{5}f_{k+2} + \frac{4}{105}f_{k+4} - \frac{1}{280}f_{k+4}) \quad \text{(B.1)}$$

while the second derivative is approximated by fourth-order finite difference which is given by

$$\left[\frac{d^2f}{dx^2}\right]_k = \frac{1}{\Delta x^2}(-\frac{1}{12}f_{k-2} + \frac{4}{3}f_{k-1} - \frac{5}{2}f_k + \frac{4}{3}f_{k+1} - \frac{1}{12}f_{k+2}. \quad \text{(B.2)}$$

B.2 Time integration

An implicit second-order backward Euler method is used to integrate the Navier-Stokes system in time.The Laplacian term is taken implicitly whereas the nonlinear and convective terms are evaluated explicitly using a second-order Adams-Bashforth scheme is used. The discretised formulation of the linearised Navier-Stokes system is given by

$$(\Delta - 3\tau)\mathbf{u}^{(n+1)} = Re\,\nabla p^{(n+1)} + \mathbf{f}^{(n,n-1)} \quad \text{(B.3)}$$

$$\nabla \cdot \mathbf{u}^{(n+1)} = 0 \quad \text{(B.4)}$$

where $\mathbf{f}^{(n,n-1)}$ is

$$\mathbf{f}^{(n,n-1)} = -4\tau\mathbf{u}^{(n)} + \tau\mathbf{u}^{(n-1)} + Re\left[(\mathbf{U}\cdot\nabla)\,\mathbf{u} + (\mathbf{u}\cdot\nabla)\,\mathbf{U}\right]^{(n,n-1)}. \quad \text{(B.5)}$$

In the above equations $\tau = Re/(2\Delta t)$ while the superscript $(n, n-1)$ denotes the explicit Adams-Bashforth time differencing where $[\cdot]^{(n,n-1)} = 2[\cdot]^{(n)} - [\cdot]^{(n-1)}$. At both inlet and outlet, an advective boundary condition

$$\frac{\partial \mathbf{u}}{\partial t} + U_{ad}\frac{\partial \mathbf{u}}{\partial X} = 0 \tag{B.6}$$

is used in order to allow the perturbation to escape the domain, thus mimicking an open domain with U_{ad} being a chosen convective velocity. A zero Dirichlet boundary conditions are imposed at infinity in the Y-coordinate.

The expression for the pressure perturbation can be obtained by applying divergence to the momentum equations and by using incompressibility equation to eliminate $\nabla \cdot \mathbf{u}$. The result is a Poisson's equation for the pressure. To enforce the divergence-free condition, the fractional-step method is used, that is by computing an intermediate pressure and velocity field. For the intermediate pressure computation a Neumann boundary condition is used, the pressure gradient being obtained by projection of the momentum equation (at the previous time-step) normal to the boundary.

The intermediate velocity field is then computed as follows

$$(\Delta - 3\tau)\mathbf{u}^* = Re\ \nabla p^{(n+1)} + \mathbf{f}^{(n,n-1)} \tag{B.7}$$

with a boundary conditions

$$\mathbf{u}^*_\Gamma = \mathbf{u}^{(n+1)}_\Gamma \tag{B.8}$$

where the subscript Γ denotes the boundary. The pressure correction $\phi = p^{(n+1)} - p^*$ with

$$\nabla\phi = -\frac{3}{2\Delta t}(\mathbf{u}^{(n+1)} - \mathbf{u}^*) \tag{B.9}$$

where $\nabla \cdot \mathbf{u}^{(n+1)} = 0$. Taking the divergence of (B.9) along with the Neumann boundary condition for pressure correction, the following equation

$$\Delta\phi = \frac{3}{2\Delta t}(\nabla \cdot \mathbf{u}^*) \tag{B.10}$$

is solved. Finally, the new divergence-free velocity field and the new pressure can be computed by

$$\mathbf{u}^{(n+1)} = \mathbf{u}^* - \frac{2\Delta t}{3}\nabla\phi \tag{B.11}$$

$$p^{(n+1)} = p^* + \phi. \tag{B.12}$$

Bibliography

Y. D. Afanasyev. Wakes behind towed and self-propelled bodies: Asymptotic theory. *Phys. Fluids*, 16:3235–3238, 2004.

Y. D. Afanasyev and V. N. Korabel. Wakes and vortex streets generated by translating force and force doublet: laboratory experiments. *J. Fluid Mech.*, 553:119–141, April 2006.

S. Alben, C. Witt, T. V. Baker, E. Anderson, and G. V. Lauder. Dynamics of freely swimming flexible foils. *Phys. Fluids*, 24:051901, 2012.

E.J. Anderson, W.R. McGillis, and M.A. Grosenbaugh. The boundary layer of swimming fish. *J. Exp. Biol.*, 204(1):81–102, 2001.

A. Azuma. *The biokinetics of flying and swimming.* Springer-Verlag, 1992.

S. Bagheri, E. Åkervik, L. Brandt, and D. S. Henningson. Matrix-free methods for the stability and control of boundary layers. *AIAA J.*, 47(5): 1057–1068, 2009.

R. Bale, A. A. Shirgaonkar, I. D. Neveln, A. P. S. Bhalla, M. A. MacIver, and N. A. Patankar. Separability of drag and thrust in undulatory animals and machines. *Scientific Reports*, 4:7329, December 2014.

D. S. Barrett, M. S. Triantafyllou, D. K. P. Yue, M. A. Grosenbaugh, and M. J. Wolfgang. Drag reduction in fish-like locomotion. *J. Fluid Mech.*, 392:183–212, 1999.

C. M. Bender and S. A. Orszag. *Advanced Mathematical Methods for Scientists and Engineers I: Asymptotic Methods and Perturbation Theory.* Springer Science & Business Media, March 2013.

Q. Bone. Muscular and Energetic Aspects of Fish Swimming in *Swimming and Flying in Nature: Volume 2*, pages 493–528. Springer US, Boston, MA, 1975.

Q. Bone and R. Moore. *Biology of Fishes.* Taylor & Francis, New York, 3rd edition, 2008.

I. Borazjani and F. Sotiropoulos. Numerical investigation of the hydrodynamics of anguilliform swimming in the transitional and inertial flow regimes. *J. Exp. Biol.*, 212(4):576–592, 2009.

J. R. Brett. The energy required for swimming by young sockeye salmon with a comparison of the drag force on a dead fish. *Trans. Roy. Soc. Can.*, 27:1637–1652, 1963.

F. Candelier, F. Boyer, and A. Leroyer. Three-dimensional extension of lighthill's large-amplitude elongated-body theory of fish locomotion. *J. Fluid Mech.*, 674:196–226, 2011.

B. J. Cantwell. Viscous starting jets. *J. Fluid Mech.*, 173:159–189, 1986.

J. M. Chomaz. Global instabilities in spatially developing flows: non-normality and nonlinearity. *Annu. Rev. Fluid Mech.*, 37(1):357–392, 2005.

J. M. Chomaz, P. Huerre, and L. G. Redekopp. A frequency selection criterion in spatially developing flows. *Stud. Appl. Math.*, 84(2):119–144, 1991.

A. Couairon and J. M. Chomaz. Global instability in fully nonlinear systems. *Phys. Rev. Lett.*, 77:4015–4018, Nov 1996.

T. Daniel, C. Jordan, and D. Grunbaum. Hydromechanics of swimming in *Advances in comparative and environmental physiology: Volume 11*, pages 17–49. Springer-Verlag, London, 1992.

P. A. Dewey, B. M. Boschitsch, K. W. Moored, H. A. Stone, and A. J. Smits. Scaling laws for the thrust production of flexible pitching panels. *J. Fluid Mech.*, 732:29–46, 2013.

E. G. Drucker and G. V. Lauder. A hydrodynamic analysis of fish swimming speed: wake structure and locomotor force in slow and fast labriform swimmers. *J. Exp. Biol.*, 203:2379–2393, 2000.

E.G. Drucker and G.V. Lauder. Locomotor forces on a swimming fish: three-dimensional vortex wake dynamics quantified using digital particle image velocimetry. *J. Exp. Biol.*, 202(18):2393–2412, 1999.

A. B. Dubois and C. S. Ogilvy. Forces on the tail surface of swimming fish: Thrust, drag and acceleration in bluefish (pomatomus saltatrix). *J. Exp. Biol.*, 77(1):225–241, 1978.

U. Ehrenstein, M. Marquillie, and C. Eloy. Skin friction on a flapping plate in uniform flow. *Philos. T. Roy. Soc. A*, 372(2020), 2014.

C. Eloy. Optimal Strouhal number for swimming animals. *J. Fluids Struct.*, 30:205–218, 2012.

F. E. Fish. The myth and reality of gray's paradox: implication of dolphin drag reduction for technology. *Bioinspir. Biomim.*, 1(2):R17, 2006.

F. E. Fish, P. Legac, T. M. Williams, and T. Wei. Measurement of hydrodynamic force generation by swimming dolphins using bubble dpiv. *J. Exp. Biol.*, 217(2):252–260, 2014.

B. E. Flammang, G. V. Lauder, D. R. Troolin, and T. E. Strand. Volumetric imaging of fish locomotion. *Biol. Letters*, 7(5):695–698, 2011.

B. Fornberg. Steady viscous flow past a circular cylinder up to reynolds number 600. *J. Comput. Phys.*, 61(2):297 – 320, 1985.

P. Freymouth. Propulsive vortical signature of plunching and pitching airfoils. *AIAA J.*, 26:821–883, 1988.

R. Godoy-Diana, J.-L. Aider, and J. E. Wesfreid. Transitions in the wake of a flapping foil. *Phys. Rev. E*, 77:016308, 2008.

J. Gustafsson and B. Protas. On oseen flows for large reynolds numbers. *Theor. Comput. Fluid Dyn.*, 27(5):665–680, 2012.

D. A. Hammond and L. G. Redekopp. Global dynamics of symmetric and asymmetric wakes. *J. Fluid Mech.*, 331:231–260, January 1997.

G. Helfman, B. B. Collette, D. E. Facey, and Brian W. Bowen. *The Diversity of Fishes: Biology, Evolution, and Ecology.* Wiley-Blackwell, Chichester, UK; Hoboken, NJ, 2nd edition, May 2009.

P. Huerre and P. A. Monkewitz. Local and global instability in spatially developing flows. *Ann. Rev. Fluid Mech.*, 22:473–537, 1990.

P. Huerre and M. Rossi. Hydrodynamic instabilities in open flows in *Hydrodynamics and Nonlinear Instabilities*, pages 81–294. Cambridge University Press, Cambridge, 1998.

M. M. Koochesfahani. Vortical patterns in the wake of an oscillating airfoil. *AIAA J.*, 27:1200–1205, 9 1989.

K. Kupfer, A. Bers, and A. K. Ram. The cusp map in the complex frequency plane for absolute instabilities. *Phys. Fluids*, 30(10):3075–3082, 1987.

G. V. Lauder. Swimming hydrodynamics: ten questions and the technical approaches needed to resolve them. *Exp. Fluids*, 51(1):23–35, 2011.

G. V. Lauder and E. G. Drucker. Forces, fishes, and fuids: hydrodynamic mechanisms of aquatic locomotion. *Physiology*, 17:235–240, 2002.

G. V. Lauder and E. D. Tytell. Hydrodynamics of undulatory propulsion. *Fish Physiol.*, 23:425–468, 2005.

B. Lautrup. *Physics of Continuous Matter, Second Edition: Exotic and Everyday Phenomena in the Macroscopic World.* CRC Press, March 2011.

S. Le Dizès, P. Huerre, J. M. Chomaz, and P. A. Monkewitz. Linear global modes in spatially developing media. *Phil. Trans. R. Soc. London A*, 354 (1705):169–212, 1996.

G. C. Lewin and H. Haj-Hariri. Modelling thrust generation of a two-dimensional heaving airfoil in a viscous flow. *J. Fluid Mech.*, 492:339–362, 2003.

M. J. Lighthill. Note on the swimming of slender fish. *Journal of Fluid Mechanics*, 9:305–317, 10 1960.

M. J. Lighthill. Hydromechanics of aquatic animal propulsion. *Annual Review of Fluid Mechanics*, 1(1):413–446, 1969.

M. J. Lighthill. Aquatic animal propulsion of high hydromechanical efficiency. *J. Fluid Mech.*, 44(2):265–301, 1970.

M. J. Lighthill. Large-amplitude elongated-body theory of fish locomotion. *Proc. R. Soc. Lond. B*, 179(1055):125–138, 1971.

S. Lighthill. *Mathematical Biofluiddynamics.* Society for Industrial and Applied Mathematics, 1975.

M. Marquillie and U. Ehrenstein. Numerical simulation of separating boundary-layer flow. *Computers & Fluids*, 31(4-7):683 – 693, 2002.

M. Marquillie and U. Ehrenstein. On the onset of nonlinear oscillations in a separating boundary-layer flow. *J. Fluid Mech.*, 490:169–188, 2003.

M. J. McHenry and G. V. Lauder. The mechanical scaling of coasting in zebrafish (danio rerio). *J. Exp. Biol.*, 208(12):2289–2301, 2005.

M. J. McHenry, E. Azizi, and J. A. Strother. The hydrodynamics of locomotion at intermediate reynolds numbers: undulatory swimming in ascidian larvae (botrylloides sp.). *J. Exp. Biol.*, 206:327–343, 2003.

P. Meunier and G. R. Spedding. Stratified propelled wakes. *J. Fluid Mech.*, 552:229–256, 2006.

P. A. Monkewitz. The absolute and convective nature of instability in two-dimensional wakes at low reynolds numbers. *Physics of Fluids*, 31(5): 999–1006, 1988.

P. A. Monkewitz, P. Huerre, and J. M. Chomaz. Global linear stability analysis of weakly non-parallel shear flows. *J. Fluid Mech.*, 251:1–20, 1993.

K. W. Moored, P. A. Dewey, A. J. Smits, and H. Haj-Hariri. Hydrodynamic wake resonance as an underlying principle of efficient unsteady propulsion. *J. Fluid Mech.*, 708:329–348, 10 2012.

K. W. Moored, P. A. Dewey, B. M. Boschitsch, A. J. Smits, and H. Haj-Hariri. Linear instability mechanisms leading to optimally efficient locomotion with flexible propulsors. *Phys. Fluids*, 26:041905, 2014.

Faith A. Morrison. *An Introduction to Fluid Mechanics*. Cambridge University Press, April 2013. ISBN 978-1-107-00353-8.

U. K. Müller, B. L. E. Van Den Heuvel, E. J. Stamhuis, and J. J. Videler. Fish foot prints: morphology and energetics of the wake behind a continuously swimming mullet (Chelon labrosus Risso). *J. Exp. Biol.*, 200(22):2893–2906, 1997.

J. C. Nauen and G. V. Lauder. Hydrodynamics of caudal fin locomotion by chub mackerel, scomber japonicus (scombridae). *J. Exp. Biol.*, 205: 1709–1724, 2002.

F. Paraz, L. Schouveiler, and C. Eloy. Thrust generation by a heaving flexible foil: Resonance, nonlinearities, and optimality. *Phys. Fluids*, 28:011903, 2016.

R. Peyret. *Spectral Methods for Incompressible Viscous Flow.* Springer, March 2002.

B. Pier and P. Huerre. Nonlinear self-sustained structures and fronts in spatially developing wake flows. *J. Fluid Mech.*, 435:145–174, 2001.

D. B. Quinn, G. V. Lauder, and A. J. Smits. Scaling the propulsive performance of heaving flexible panels. *J. Fluid Mech.*, 738:250–267, 2014.

H. Schlichting and K. Gersten. *Boundary-Layer Theory*. Springer Science & Business Media, 2003.

A. H. Schooley and R. W. Stewart. Experiments with a self-propelled body submerged in a fluid with a vertical density gradient. *J. Fluid Mech.*, 15 (1):83–96, 1963.

L. Schouveiler, F. S. Hover, and M. S. Triantafyllou. Performance of flapping foil propulsion. *J. Fluids Struct.*, 20:949–959, 2005.

M. Sfakiotakis, D. M. Lane, and J. B. C. Davies. Review of fish swimming modes for aquatic locomotion. *IEEE J. Oceanic Eng.*, 24(2):237–252, 1999.

S. A. Smirnov and S. I. Voropayev. On the asymptotic theory of momentum/zero-momentum wakes. *Phys. Lett. A*, 307(2–3):148 – 153, 2003.

C. Sozou. Development of the flow field of a point force in an infinite fluid. *J. Fluid Mech.*, 91(3):541–546, 1979.

G. Taylor. Analysis of the swimming of microscopic organisms. *P. Roy. Soc. A - Math. Phy.*, 209(1099):447–461, 1951.

G. K. Taylor, R. L. Nudds, and A. L. R. Thomas. Flying and swimming animals cruise at a Strouhal number tuned for high power efficiency. *Nature*, 425:707–711, 2003.

G. S. Triantafyllou, M. S. Triantafyllou, and M. A. Grosenbaugh. Optimal thrust development in oscillating foils with application to fish propulsion. *J. Fluid Struct.*, 7:205–224, 1993.

E. D. Tytell and G. V. Lauder. The hydrodynamics of eel swimming. i. wake structure. *J. Exp. Biol.*, 207:1825–1841, 2004.

J. L. van Leeuwen, C. J. Voesenek, and U. K. Müller. How body torque and strouhal number change with swimming speed and developmental stage in larval zebrafish. *J. R. Soc. Interface*, 12(110):20150479, 2015.

J. J. Videler. *Fish swimming*, volume 10 of *Fish and fisheries Series*. Chapman & Hall, London, 1993.

S. Vogel. *Life in Moving Fluids: The Physical Biology of Flow.* Princeton University Press, 1994.

S. I. Voropayev and S. A. Smirnov. Vortex streets generated by a moving momentum source in a stratified fluid. *Phys. Fluids*, 15(3):618–624, 2003.

S. I. Voropayev, H. J. S. Fernando, S. A. Smirnov, and R. Morrison. On surface signatures generated by submerged momentum sources. *Phys. Fluids*, 19(7), 2007.

P. W. Webb. The swimming energetics of trout: I. thrust and power output at cruising speeds. *Journal of Experimental Biology*, 55(2):489–520, 1971.

P. W. Webb. Form and function in fish swimming. *Sci. Am.*, 251:72–82, 1984.

D. Weihs. Energetic significance of changes in swimming modes during growth of larval anchovy, engraulis mordax. *Fish. Bull*, 77:597–604, 1980.

T. Y. Wu. Hydromechanics of swimming propulsion. part 3. swimming and optimum movements of slender fish with side fins. *J. Fluid Mech.*, 46(3): 545–568, 1971.